Direction Measurement Capabilities of the LEDA Cosmic Ray Detector

SANDRA LYN BULTENA

Department of Physics

McGill University, Montreal, Québec

21/3/88

A thesis submitted to the Faculty of Graduate Studies and Research in partial fulfillment of the requirements for the degree of Master of Science in Physics.

Direction Measurement Capabilities of the LEDA Cosmic Ray Detector

To my family

ABSTRACT

The LEDA extensive air shower array is a device used for searches of point sources of cosmic rays. We survey the history of such searches and describe the design and construction of the LEDA detector with special emphasis on the timing and directional resolution characteristics. We find through a combination of Monte Carlo and data analysis that the angular resolution is between 0.65° and 1.25°, sufficient for point source searches. Very preliminary results on star-tracking are presented, indicating good acceptance of our experiment for the γ-ray source Cygnus X-3.

RESUME

La matrice LEDA pour mesurer les gerbes atmosphériques étendues est un appareil utilisé pour chercher des sources ponctuelles de rayons cosmiques. Nous donnons un apery de l'histoire de telles rècherches et décrivons la construction du détecteur LEDA avec l'emphase sur la résolution temporelle et directionnelle. A travers des programmes Monte Carlo et l'analyse de données expérimentales, nous trouvons une résolution angulaire entre 0.65° et 1.25°, ce qui est suffisant pour chercher des sources ponctuelles. Des résultats très préliminaires sur les positions des étoiles sont présentés, indiquant une bonne acceptation de notre expérience pour la source de rayons γ Cygnus X-3.

ACKNOWLEDGEMENTS

I'd like to thank my supervisor Dr. David Hanna for his incredible support and tolerance throughout this experiment. Our thought provoking debates taught me much about the world of experimental physics.

The official collaboration of the LEDA experiment is David (my supervisor), Kavita Murthy (another MSc. student), and myself. I cannot express in words how much we three have helped each other solve the analytical and physical details of our experiment, This experiment was a 'true' collaboration in every sense of the word, and I would have been hopelessly lost if it were not for David and Kavita.

Our experiment would not have been possible without the valuable assistance of Paul Mercure, who not only wrote the data acquisition programs and helped us de-bug *our* programs, but also devoted some of his own personal time to help us with some of the dirty work (laying cables, etc.) required when building an experiment.

I would also like to thank Robert Nowac, firstly for his ability to make me laugh when things were going wrong, and secondly for the beautiful diagrams which he made for my thesis (many at the last moment). Along with Robert and Paul, I would like to thank all the people in the department who made my days more enjoyable by just 'being there'.

And finally, I would like to thank all of my family for their support; my husband Stephen, who gives me incredible emotional support in all my endeavors (and even did all the household chores while I wrote my thesis); my son Michael who, although he is really too young to understand, tolerated my absences as well as my 'grumpy days' with very little fuss; and my parents, for whom without their lifelong adage of "if you are willing to work hard enough, nothing is unattainable", I would have probably given up long ago.

TABLE OF CONTENTS

1.0 INTRODUCTION

Soon after the pulsar Cygnus X-3 was discovered to be a source of very high energy neutral particles (generally believed to be γ-rays), physicists and astro-physicists intensified their research efforts in obtaining more data on the cosmic ray phenomenon. Sometimes the results of these observations brought more questions than were answered. Are the high energy particles coming from Cygnus X-3 γ-rays, or some unknown particle? Why is the flux of Cygnus X-3 variable? What causes the production of these high energy particles?

Before theorists can even begin to answer these questions, more information is needed about the locations of other γ-ray sources, the energy spectrum of these γ-rays, and the intensity variations of γ-rays over the period of the pulsar. At McGill University in Montreal, we have built an extensive air shower array LEDA (Large Experiment to Detect Air Showers) whose purpose is to add more information in the hope that it will help to provide solutions to these questions. LEDA consists of 19 $1\,m^2$ identical liquid scintillator detectors with an effective viewing area of $23{,}000\,m^2$. Each detector measures the particle density of the shower front, and the relative arrival times. The particle density is used to estimate the energy, and the relative arrival times are used to estimate the direction of the original cosmic ray. The directional analysis (usually referred to as the *fast-timing technique*) cannot be accomplished unless the timing accuracy of each detector is known to within a few nano-seconds (ns). This thesis will specifically deal with all aspects of the experiment which are

relevant to the location of ultra high energy (UHE) cosmic ray sources.

There are many methods to measure these cosmic rays and calculate their energy and direction, and they will be briefly discussed in chapter two, along with the current observations of γ-ray sources. In chapter three, the detectors used in the LEDA experiment will be discussed in detail with special attention given to the timing resolution of the photo-multiplier tube, light collection, and the time-slewing effects of the electronic equipment. Chapter four will discuss the array as a whole, again with special emphasis on the timing characteristics of the array. The data analysis will be discussed in detail in chapter five, and finally, the preliminary results of our observations will be discussed in the concluding chapter of this thesis.

2.0 A REVIEW OF GAMMA-RAY ASTRONOMY

2.1 Air Showers

The cascade shower effect was originally discovered by B. Rossi in 1933 when he proved that the soft component of cosmic rays would multiply in number when they passed through lead shielding. In 1937 J.F. Carlson and J.R. Oppenheimer developed the theory for this process. As a highly energetic particle passes through any medium, it will interact with a nucleus to produce more particles, each of which is also highly energetic. For example, an electron or positron emits high energy photons when deflected by the nuclear coulomb field (the bremsstrahlung process). A photon, if it has an energy of $1.02 MeV$ or greater, will under certain circumstances split into an electron and positron (the pair-production process). Since the energy of the primary particle is equally shared with the electron-positron pair, the energies of the individual particles decrease rather slowly in comparison with the increase in the number of particles.[1]

An air shower is simply a cascade shower produced in the atmosphere, which is 27 radiation lengths long, instead of an absorbing material. If the primary particle is energetic enough ($\sim 10^{14} eV$ or higher), the subsequent particles retain enough energy to penetrate the atmosphere and reach sea level. By this time, the number of particles is very large, and because the low density permits the secondary particles to spread far apart over the longitudinal range of $20 km$, the lateral spread of the particles may extend as far as several hundred meters. The term 'extensive air shower'

(EAS for short) is used to describe this event. The flux of cosmic rays with energy $\geq 10^{18}\, eV/particle$ through a $1\, m^2$ detector outside the atmosphere is 1 particle per $3000\, yrs$, but in the process of creating an air shower, the atmosphere magnifies the signal and distributes the secondary particles over an area of the order of one square kilometer. The result of this magnification is that the detector need only sample a small portion of the air shower, which given the large shower size, results in an enormous effective collection area. One could then detect the resulting air showers approximately once every few weeks.[2] An example of the beginning of an EAS is shown in figure 2.1.

Composition

The extensive air shower consists of three components: 1) the hadronic component, traditionally called the N-component (all particles which participate in the strong nuclear interaction); 2) electromagnetic or soft component (electrons, positrons, photons); and 3) the hard or muon component.

The N-component is created when the primary charged nucleus interacts with an air molecule. It creates high energy secondary nucleons, anti-nucleons, mesons and hyperons, with the most abundant being the π-mesons. The number of nuclear active particles increases with depth until it reaches a maximum, which occurs when the increase in particles is exactly compensated for by the dissipation of the less energetic particles. After this maximum, the number of particles in the N-component decreases with attenuation length L_n which depends weakly on the atmospheric depth.

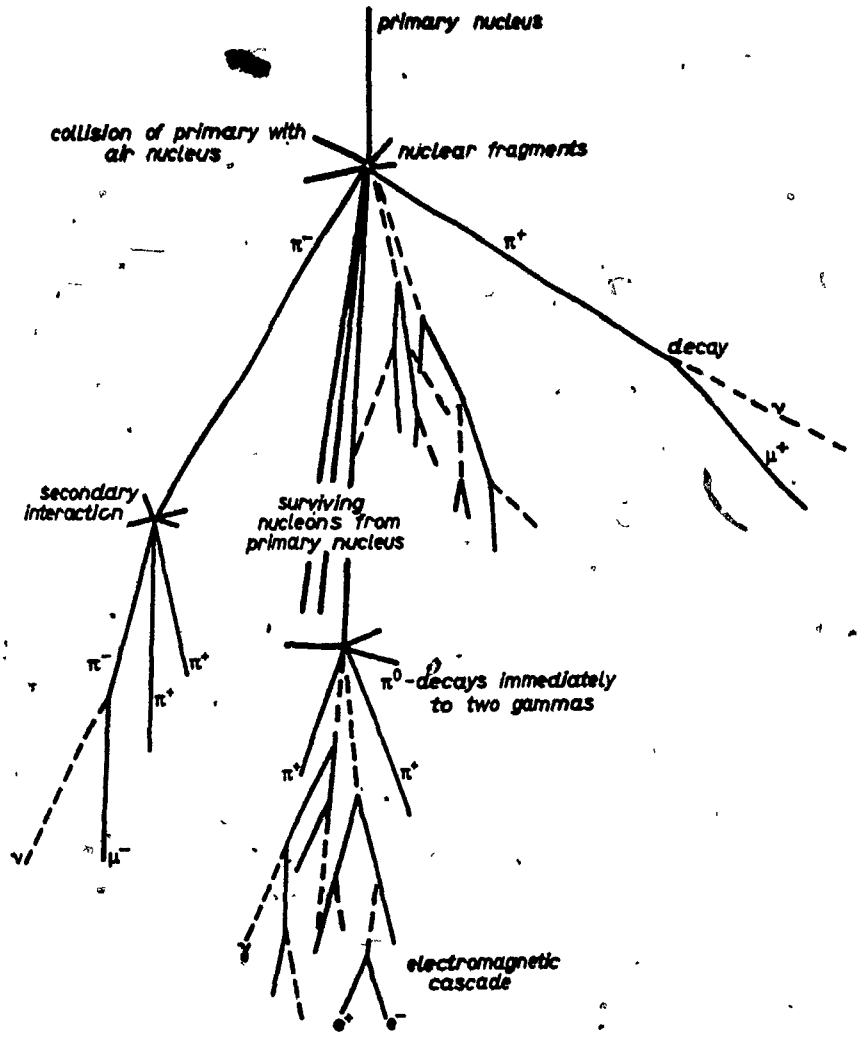

FIG 2.1: The start of a hadronic air shower and its resulting components.

The decay of the K-meson and the $\pi^{\pm}$ gives rise to the muon component which is thereafter non-multiplying. The number of μ's increase as the N-cascade develops since the muons may be lost only by decay and ionization losses, both of which are of little importance for muons of moderately high energies. The lifetime of the muon is $\sim 2.2 \times 10^{-6}\, s$, but relativistic time dilation increases this by orders of magnitude, allowing muons to survive to ground level.

The electromagnetic cascade is started when the secondary π^0, which comprises $20 \sim 30\%$ of the N-cascade, decays into two γ's, which occurs $> 98\%$ of the time. This decay has a lifetime of $10^{-16}\, s$ so chances of the π^0 interacting before decaying are remote. The γ-rays produce electron-positron pairs which will in turn produce γ-rays from the bremsstrahlung process. The electromagnetic shower is not 'pure' in the sense that it can also produce muons. If the γ-ray has an energy $\geq 2 \times 10^9 eV$ it can produce π-mesons which will then produce muons. However, this process has a very small cross section, and the total number of muons produced in the electromagnetic cascade is 0.1% of the number of electrons, which is $10 \rightarrow 100$ times smaller than the observed number of muons in a proton initiated shower.

The final products of the air shower will consist of the three components (N, electromagnetic, and muon) as well as neutrinos, which are created along with the muons in the development of the N-cascade. These particles will cover a nearly circular area about an axis which lies along the trajectory of the primary cosmic ray, and the number of particles that belong to the respective components in the EAS are denoted by

N_n, N_μ, N_e. N_e is about 95% of the total, $N_\mu \sim 4\%$ and the N-component is $\sim 1\%$. Indeed, physicists were long misled by the overwhelming abundance of electrons to interpret the showers as purely electromagnetic cascades.[3] Most of the N-component of the air shower which does penetrate to sea level is centered around the core of the shower. The relative density of the muon component N_μ/N_e however, increases as one moves away from the core.

In 1941, Schein et al.[4] measured the differences of the cosmic ray flux in the east – west direction and concluded that most of the primary cosmic rays are protons. The rest of the primary cosmic rays are nucleons, with the heaviest being iron. The gross features of the relative abundance of these nuclei are similar to those of galactic elements. There are some cosmic rays which are photons, but they comprise less than 1% of the total flux.[3]

Lateral Distribution

As described earlier, the secondary cosmic ray particles will form a thin disk-like shape centered around the core of the shower. In an electromagnetic air shower, the Coulomb scattering suffered by the electron as it passes by air molecules is the most significant cause of the displacement of these electrons from the shower axis. The most common function which describes this lateral distribution is the function calculated by J. Nishimura, K. Kamata, and K. Greisen, commonly referred to as the NKG function.

$$NKG(r, N_e, s) = \frac{.433 N_e s^2}{r_m^2}(1.9 - s)\left(\frac{r}{r_m} + 1\right)^{s-4.5}\left(\frac{r}{r_m}\right)^{s-2} \qquad 2.1$$

where

r = distance from the core

N_e = total number of electrons in the shower at the detector level

s = shower age

r_m = Molière radius of air $= 21X_0/E_c$ where X_0 is the radiation length and E_c is the critical energy of the electron. ($r_m \sim 79m$ at sea level)

The Molière radius r_m is a characteristic unit of length which is inversely proportional to the density of the medium. The shower age, s, describes the state of the longitudinal development of an electromagnetic cascade as well as the lateral spread of the cascade particles. If $s < 1$ the number of particles in the shower is increasing; at $s = 1$, the number of particles has reached a maximum, and for $s > 1$, the number of particles is decreasing. This is illustrated in figure 2.2. The s-parameter can also be described in reference to the energy spectrum. In a shower initiated by a single photon or electron, the power-law spectrum of photons or electrons would be[5]

$$n_e(E)\,dE \sim E^{-(s+1)}\,dE \qquad 2.2$$

where:

$n_e(E)$ = number of electrons

E = energy (eV)

s = age

The energy E of the primary particle affects the rate of the shower growth (see figure 2.3)[2] and hence, the age at a given depth in the atmosphere is a function of this

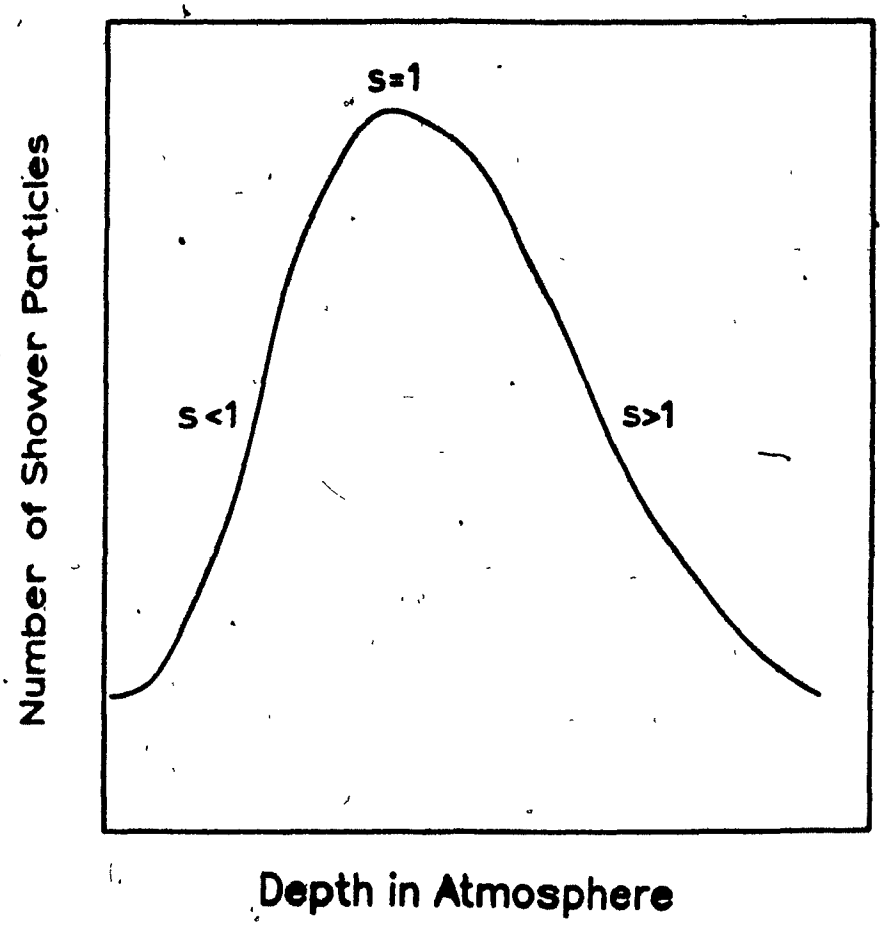

FIG 2.2: The physical meaning of the "shower age" s.

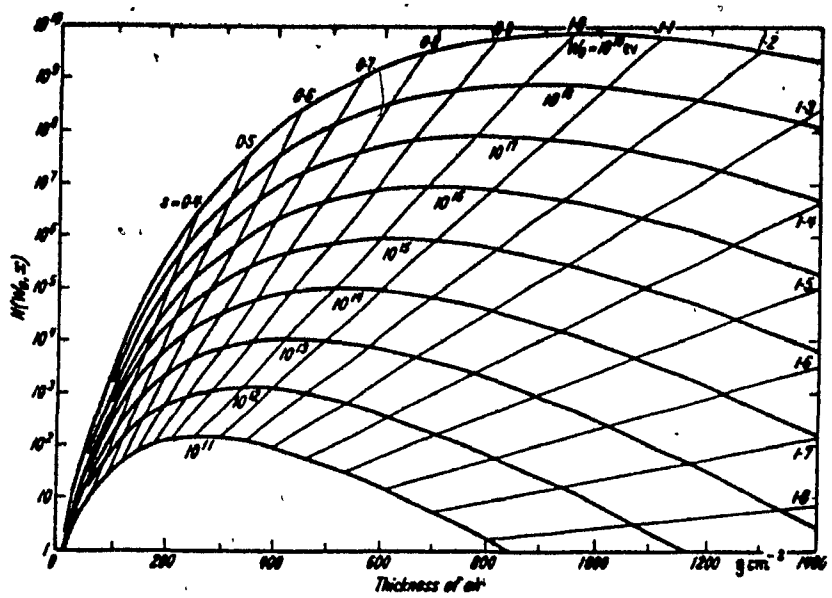

FIG 2.3: The total number of electrons, as a function of the thickness (g cm^{-2}) of air crossed, produced by photons of various energies, W_e, in eV. The parameter s is the age of the shower at different stages of its development.

energy. The results of the experiments studying cosmic ray showers are contrary to predictions for electromagnetic cascades begun by a single photon or electron at the top of the atmosphere, or by a collection of π^0 mesons originating in a single nuclear collision at the origin of the shower.[5] Hence a shower can be identified as having a charged nucleus as the primary cosmic ray if the age parameter differs greatly from the one expected for it from the theory.[5]

Up until this time, we have only considered the electromagnetic models for the lateral distribution of particles. However, if one discounts the mesons and their secondary particles at very large radii, the NKG function (and its approximations), agree closely with the pure electronic cascade model. The energy of the incident primary is

then calculated using the rough estimate of:

$$E \approx 10^{10} N \; eV \qquad 2.3$$

where

N = the number of electrons at sea level.

Time Distribution

An electromagnetic shower consists of many electrons which have a broad range of energies, scattered throughout the shower front. This gives rise to relative time delays between the photons and electrons. If these delays were due to the difference in velocities, they would be very small since all the particles in the shower travel with velocities close to the speed of light, and the total distance that they cross is only a few kilometers. It is the differences of path length caused by scattering of the electron off of air molecules which introduces measurable delays for the electrons. One of the earlier EAS experiments[6] measured these time differences and found them to be of the order of a few nanoseconds. This corresponds to the shower front having a physical thickness of $1 \sim 2\,m$.

When measuring an EAS, another time factor must also be taken into consideration. Usually the shower front is described as a thin disk, but in fact it has a spherical shape. P. Bassi et al.[7] used three particle counters arranged on a single plane to estimate the average radius of curvature (R). They concluded that the expectation value for the radius of the shower front is $2600\,m$ with a lower limit of $1300\,m$. Therefore, if one measures the EAS with an array of counters on a single plane, the off-axis

particles will be delayed by a factor

$$ct \approx \frac{d^2}{2R} \qquad 2.4$$

where:

R = the radius of curvature for the shower front

d = distance of the particles from the core of the shower

The shower front can be approximated to a thin, disk-like plane only if the method of detection is arranged such that the off axis delay time is of the same order as the electron-photon delay time due to the shower thickness, as described in the previous paragraph, ie: $d^2/2R \sim 1\,m$ or $d \sim 73\,m$.

2.2 Observational Methods

The extensive air shower is a complex phenomenon whose properties cannot all be studied in detail by one single experimental design. Therefore more than one method of observation has been developed to measure the particular aspects of cosmic rays that the physicist wished to study. Some of the methods of observations are:

(1) observation of the Čerenkov light produced in the atmosphere by energetic electrons can be used to study: the longitudinal structure of the EAS and the incident directions of primary cosmic rays in the energy range of $10^{12} \rightarrow 10^{15} eV$;

(2) extensive air shower arrays, which can determine: the energy spectrum from $10^{15} \rightarrow 10^{19} eV$; the lateral spread of the particles by method of core selection; and the incident direction of the primary cosmic rays using fast timing techniques which can be used in studies of the isotropic or anisotropic nature of the flux;

Atmospheric Čerenkov Detectors

As the air shower progresses through the atmosphere, the energetic electrons ($E \geq 21\,MeV$) emit Čerenkov light with an angular deviation less than 1^0. Large mirrors are used to focus this light onto an array of photomultiplier tubes. One of the advantages of this technique is that it provides a means of investigating the longitudinal structure of the EAS. The intensity of Čerenkov light is proportional to the total energy dissipated in the atmosphere. Another advantage to this method of observation is a good angular resolution($\sim 1°$), suitable to the study of the anisotropy of primary cosmic rays. However, the largest disadvantage of atmospheric Čerenkov light detection is the inability to take data at any time other than clear moonless nights.

Detectors are designed with parabolic mirrors with either one photo-multiplier tube (PMT) or an array of PMTs placed at the focal point of the mirror. The mirror gives great sensitivity, due to both the large area of light collection and to the narrow angular pointing. The mirrors that use only one PMT measure the particle density indirectly by measuring the Čerenkov light flux. This flux is related to the number of particles in the shower by the following formula:[8]

$$Q \sim N^{0.8\pm0.05} \qquad 2.5$$

where

Q = flux of incident Čerenkov light

N = the number of particles

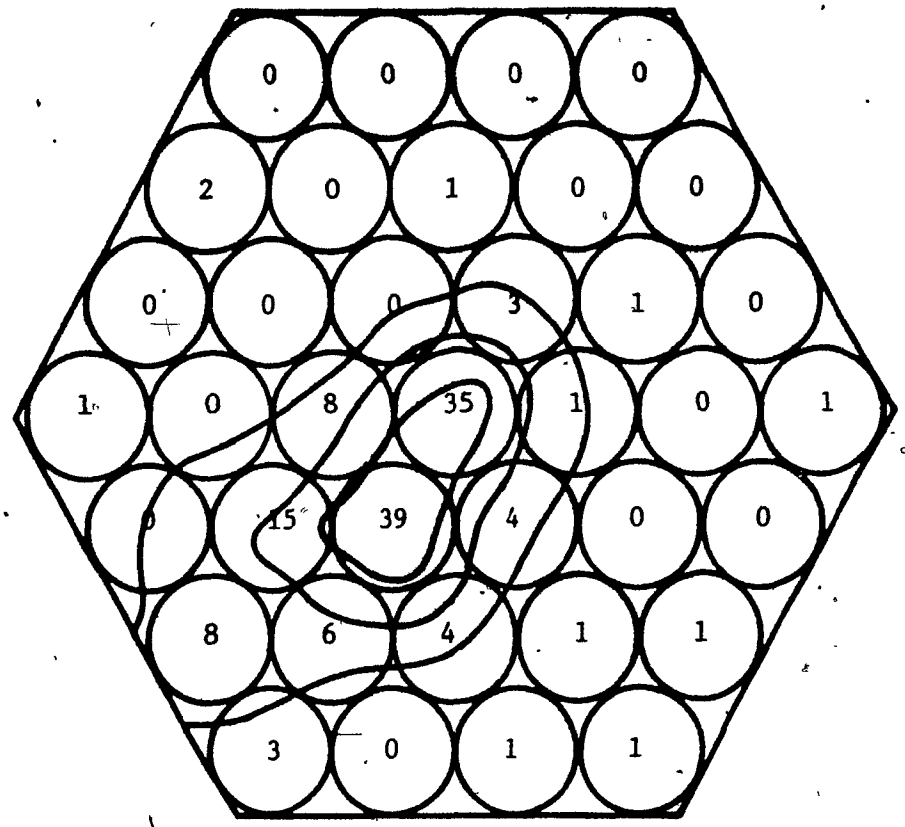

FIG 2.4: CERENKOV-LIGHT MAP of an air shower was made with the 10-meter reflector at the Whipple Observatory. The circles represent the phototubes. The numbers are proportional to the intensity of the light recorded by each phototube; the lines are intensity contours. From such a map the axis of the air shower and hence the arrival direction of the cosmic ray can be calculated. In this case the axis of the shower is parallel to the axis of the detector and displaced from the detector toward the lower left. The map records only a part of the edge of the conical shower, which may be hundreds of meters in diameter.

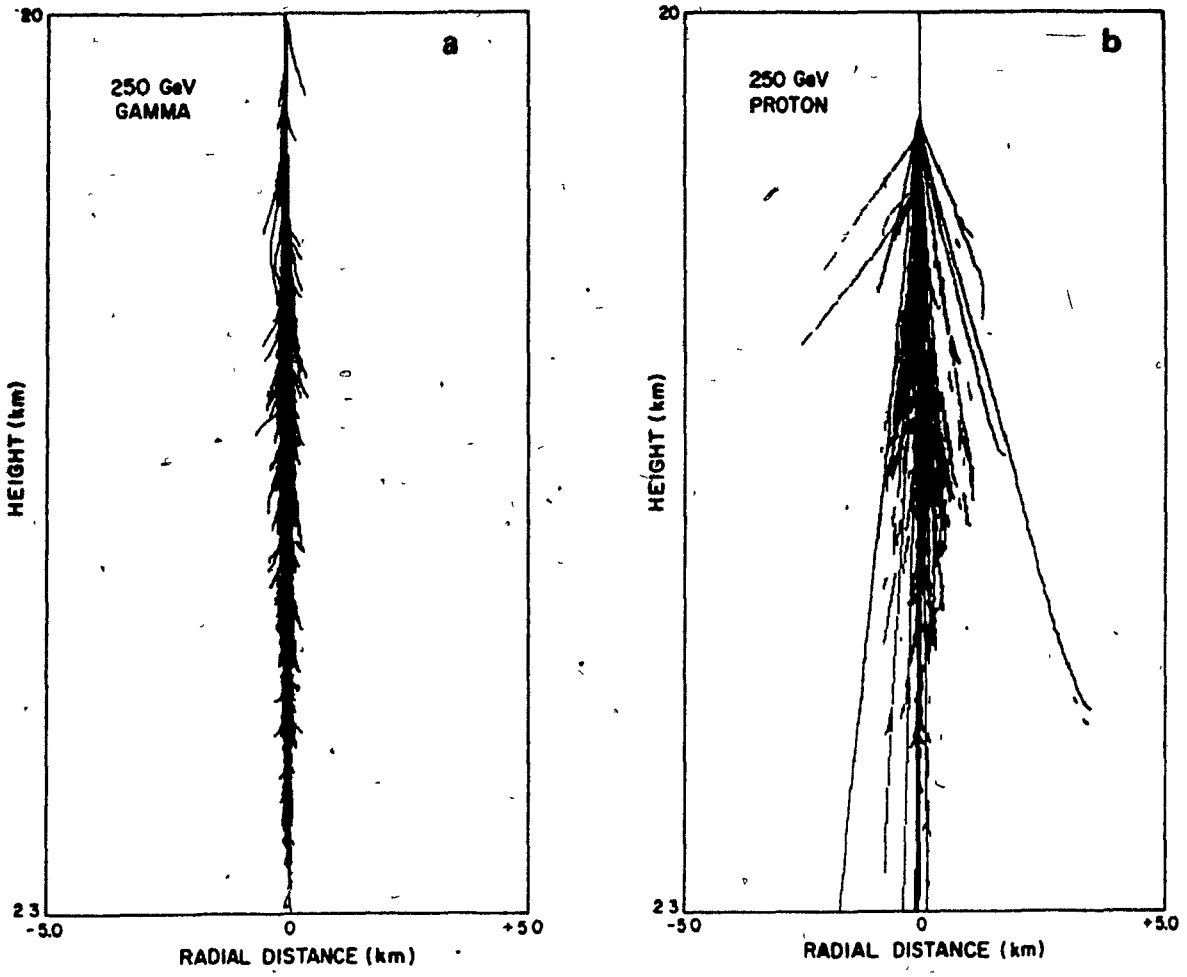

FIG. 2.5: Monte Carlo simulation of the development of air showers from (a) $250\,GeV$ gamma; (b) $250\,GeV$ proton. Each line represents a relativistic particle in this side view of two vertically incident showers.

The mirrors which have many PMT's at the focal point are used to reconstruct the image formed on the mirror by the Čerenkov light rings. Since the shower development is observed over a large range, and since each electron over the critical energy will produce Čerenkov radiation, the image produced on the mirror will not be a single ring, but instead it will consist of a circle or elliptic form of light. An example of this is shown in figure 2.4. It shows data obtained at the Fred Lawrence Whipple Observatory.[9] By Monte Carlo methods it was shown[10] that the directional differences of electrons in an hadronic shower is much larger than in the purely electronic shower. Hence, it can be seen from figure 2.5 that the circle of Čerenkov light will be narrower if the air shower is initiated by a γ-ray. Thus these detectors can be used to differentiate between the showers initiated by a γ-ray or a charged particle.

One method of observation, used by the Crimean group[11] , requires two or more mirrors pointed towards some pre-fixed location in the sky. The advantage of these detectors is that they can study EAS which have an energy $\geq 10^{12}\ eV$ because Čerenkov light is emitted before the shower particles have been absorbed in the atmosphere, and since the Čerenkov light is in the visible range, it suffers very little attenuation. The disadvantage of this method is that the detector is only sensitive to a small portion of the sky during any particular time, which would make it difficult to find any new anisotropic properties of the γ-ray fluxes.

The Fly's Eye experiment in Utah uses 67 mirrors. Each of these mirrors points to a different region in space covering approximately 6 steradians of viewing angle.

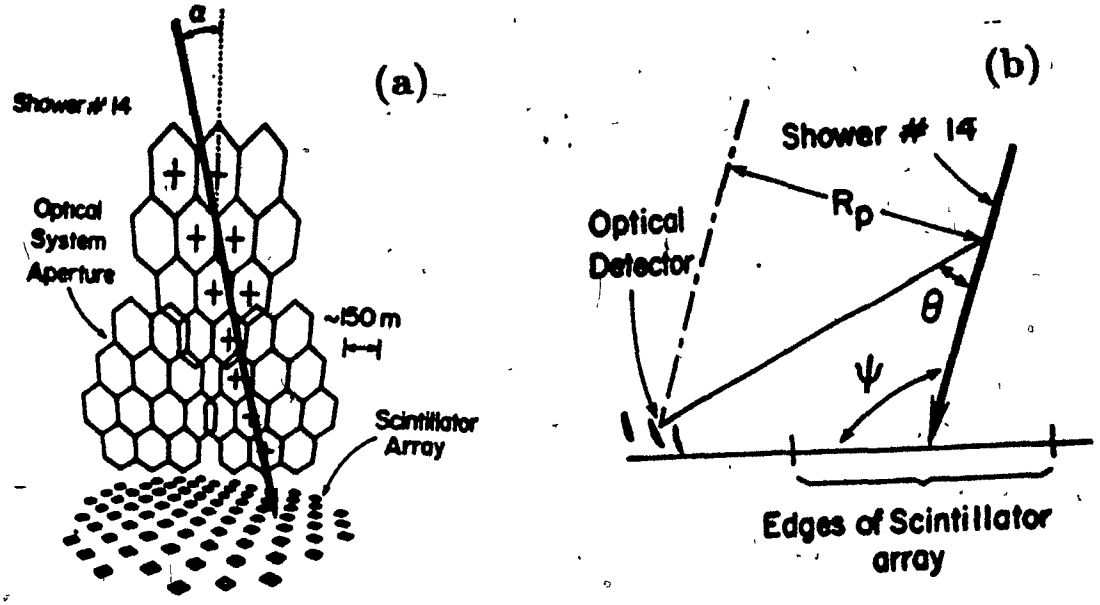

FIG 2.6: FLY'S EYE DETECTOR a) Projection of the optical detector's aperture onto a vertical plane above the center of a scintillator array (CASA). A reconstructed shower trajectory is indicated by the heavy line. Crosses denote phototube aperture in which a signal was detected. b) View of the plane defined by a shower and the optical detector.

This enables them to observe showers at very large distances. As the shower progresses, various detectors will record the light generated by two separate processes; the Čerenkov radiation of shower going directly into the Fly's Eye; and by the scintillation light caused by the de-excitation of the nitrogen molecules in the atmosphere. This detector has many advantages, the most obvious being that almost all of the sky can be observed simultaneously. The second advantage is that the longitudinal development of a shower can be observed when the shower is located anywhere between 0.3 and 50 km from the detector. This method is illustrated in figure 2.6. However, the disadvantages is that the spectrum is limited to[12] $10^{16} \leq E \leq 10^{21}$ when mea-

suring the nitrogen fluorescence and $10^{12} - 10^{14}\,eV$ for the Čerenkov radiation; and the source of the primary cosmic ray cannot be measured with the same degree of accuracy as the previous described methods.

Extensive Air Shower Arrays

The most easily measured quantity of an EAS is the lateral distribution. Since the total number of particles cannot be measured directly, it is necessary to measure the number of particles falling on a limited number of detectors. These detectors usually consist of a combination of: scintillators, for counting particles as well as fast-timing; geiger counters; thick Čerenkov counters, to absorb the electronic component and thus measure the energy density; shielded detectors to measure the muon content; and/or flash detectors used to study the hadronic portion of the EAS.

To determine the shape of the energy spectrum it is necessary to first calculate the total number of particles which arrived at the detector level, which would indicate (by equation 2.3) the energy of the incident primary. The relative accuracy of these measurements is dependent upon the spacing and the physical arrangement of the detectors used to study the EAS. This is because the density spectrum falls off very rapidly as one goes away from the core of the shower, and if the density of particles is too low near the detectors, the statistical fluctuations start to influence the calculation of the shower core, and hence, the measurement of the energy becomes suspect. For example, if a shower has $2 \cdot 10^5$ ($E \sim 2 \cdot 10^{15}\,eV$) particles, the theory predicts that the particle density will be 25 particles/m^2 at a radius of $10\,m$ from the core, but the

density will fall to less than 1 particle/m^2 in less than 50 m.[3] To measure this size of shower accurately, the particle counters must be placed close together, or the event will not be seen.

The core of the shower is usually calculated by fitting the data to an approximation of the NKG function given by:

$$\rho(N,r) = N\frac{1}{2\pi r_o}\frac{e^{-\frac{r}{r_o}}}{r_o\,(r+1)} \qquad 2.6$$

where

r_o = is an approximation of the Molière radius $(70-75m)$

r = radial distance from the center of the shower

N = total number of particles

The age of the shower is approximated to be 1.25 in this formula. A figure comparing the NKG function (equation 2.1) and equation 2.6 is shown in figure 2.7. This function, when fitted to the experimental data, will not only locate the core of the shower, but also estimate the number of particles in the shower. The methodology used in fitting this function is given in detail by Murthy.[13]

If the experiment is used to infer the properties of high-energy interactions by studying the air shower, it is necessary to investigate the structure of the EAS core (remember that the N-cascade is concentrated near the core), and this requires setting the detectors close together near the center of the array.

The muon detectors that are often used in extensive air shower arrays serve multiple purposes. Currently, the most popular use for muon detectors is called the

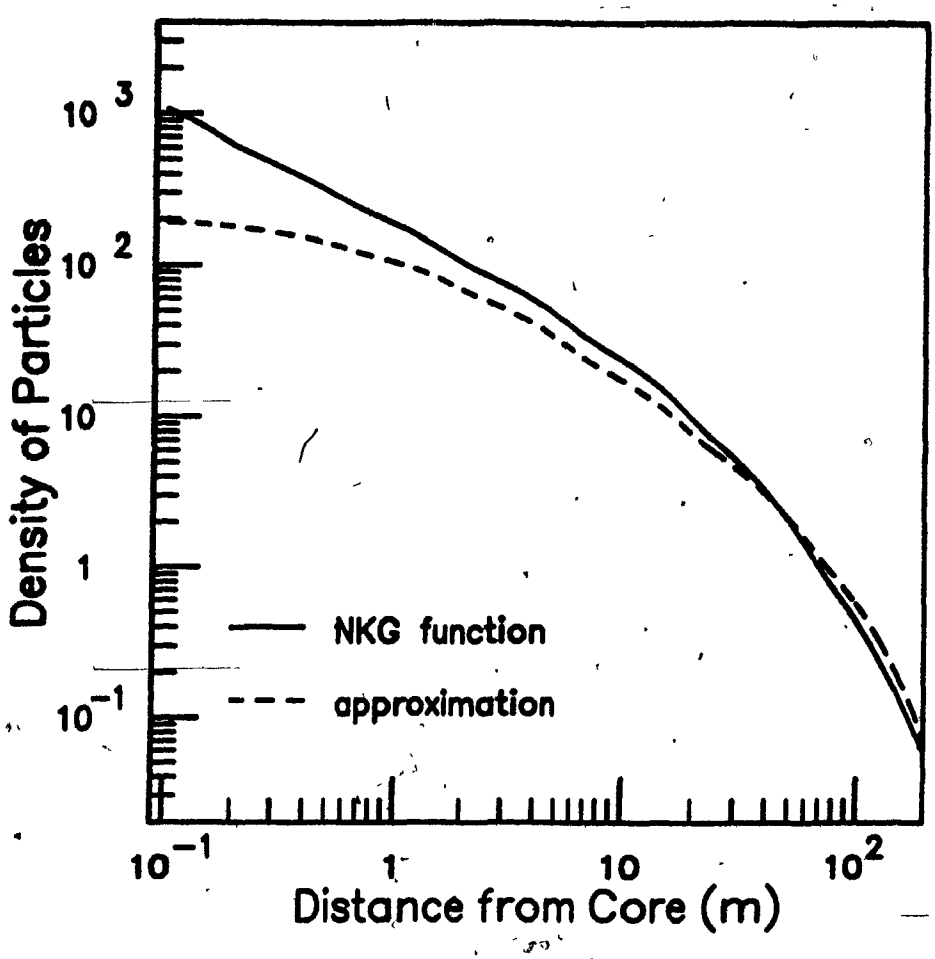

FIG 2.7: A plot showing the NKG function (equation 2.1) with the approximation of the NKG function (equation 2.6) with $s = 1.25$ and $r_m = 75\,m$.

'muon veto'. By counting the number of muons in the air shower, it is possible to determine whether a charged particle or a γ-ray initiated the shower because, as mentioned before, although the electromagnetic cascade is not 'pure', the number of muons produced in an electromagnetic shower $\gamma \rightarrow \pi \rightarrow \mu$ is less than 1/10 the number produced in an hadronic shower. If the number of muons is large; $(N_\mu/N \approx 10^{-1})$, the air shower is most probably the result of a hadronic shower, whereas if the shower is muon poor; $(N_\mu/N)_\gamma \leq 10^{-2}$, then the shower can be said to be purely electromagnetic in origin.

The results of the above methods can be improved if the arrival direction of the shower is known. The density measurements obtained from the particle counters can be corrected for the increased energy deposited in the detector due to an increased path length. Also, if the arrival direction of the shower is known, the effect of the depth of the atmosphere which the shower has passed through can be studied without building two separate arrays at different elevations. Because γ-rays are not deflected from their path by the galactic magnetic fields, the direction of the shower can also be used to find γ-ray sources.

The method used for determining the direction of the incoming primary particle is called the fast-timing technique. It is described in detail by A.C. Smith et al.[14] In essence, the relative time delays of each counter can be used to fit an equation representing the shower front distribution. If the detector array is small enough ($\sim 100m$ in diameter) the shower front is considered to be planar, and the data is fit

to the expression

$$\beta c t_i = x_i \cdot \sin\theta\cos\phi + y_i \cdot \sin\theta\sin\phi + a \qquad 2.7$$

where

t_i = time measurement from counter i

x_i , y_i = coordinates of counter i

β = velocity of the measurable shower front

θ = angle of the normal vector to the zenith

ϕ = angle of projection of the normal vector in the x-y plane

a = height of shower front at x=0, y=0 when the trigger was formed.

However, for larger arrays, it may be necessary to include the shower curvature correction $d^2/2R$ in this calculation.

2.3 γ-ray Astronomy

Cosmic rays have been studied fervently since they were first discovered in the late thirties. Many of the properties of cosmic rays, such as the composition of the primary particles, energy spectrum, lateral distributions of electrons, hadrons, and muons, and the longitudinal development, all have been studied in detail. However, although not a new field, γ-ray astronomy is becoming a 'hot' topic of research. Unlike charged particles, γ-rays cannot be deflected from their course because of the galactic magnetic fields, which enables us to pinpoint their location of creation. To do this, the scientist must search for anisotropies in the γ-ray flux. The difficulty of this task lies in the fact that of all the cosmic-ray particles, γ-rays comprise less than 1%.

Observation of Cosmic γ-rays

Since the famous radio outburst of Cygnus X-3 in 1972,[15] much time has been spent studying this system under all energy ranges; X-ray, radio, ultra-violet, etc. All of the energy ranges (except for radio) show a $4.8\,hr$ periodicity with '0-phase' corresponding to the X-ray minimum. This $4.8\,hr$ periodicity of fluxes is the fingerprint used to distinguish Cyg X-3 from other possible sources. γ-rays were first detected from Cyg X-3 in the $100\,MeV$ region by Galper et al.[16] in a balloon experiment in 1976 and in a similar experiment by Lamb et al.[17] in 1977 on the SAS-2 satellite. Both experiments used magnetic core spark chambers to measure the γ-ray fluxes. Gasper et al. obtained a flux of

$$2 \times 10^{-4}\, photons\, cm^{-2}\, s^{-1} \quad \text{for} \quad E_\gamma > 40\,MeV.$$

Lamb et al. obtained a 4.5σ excess of γ-rays over the background with fluxes of

$$\sim 10 \times 10^{-6}\, photons\, cm^{-2}\, s^{-1} \quad \text{for} \quad E_\gamma > 35\,MeV$$

and

$$\sim 4 \times 10^{-6}\, photons\, cm^{-2}\, s^{-1} \text{ averaged over the entire } 4.8\,hr \text{ period.}$$

The phase plot shown in figure 2.8 from Lamb et al. ($E_\gamma > 35\,MeV$) shows one peak, which is not sharply defined. This distribution closely resembles the amplitudes displayed in the X-ray region. Paradoxically, the COS B satellite experiment in 1977[19] found no excess γ-rays from Cyg X-3. This may be caused by the real time-variations of the flux.

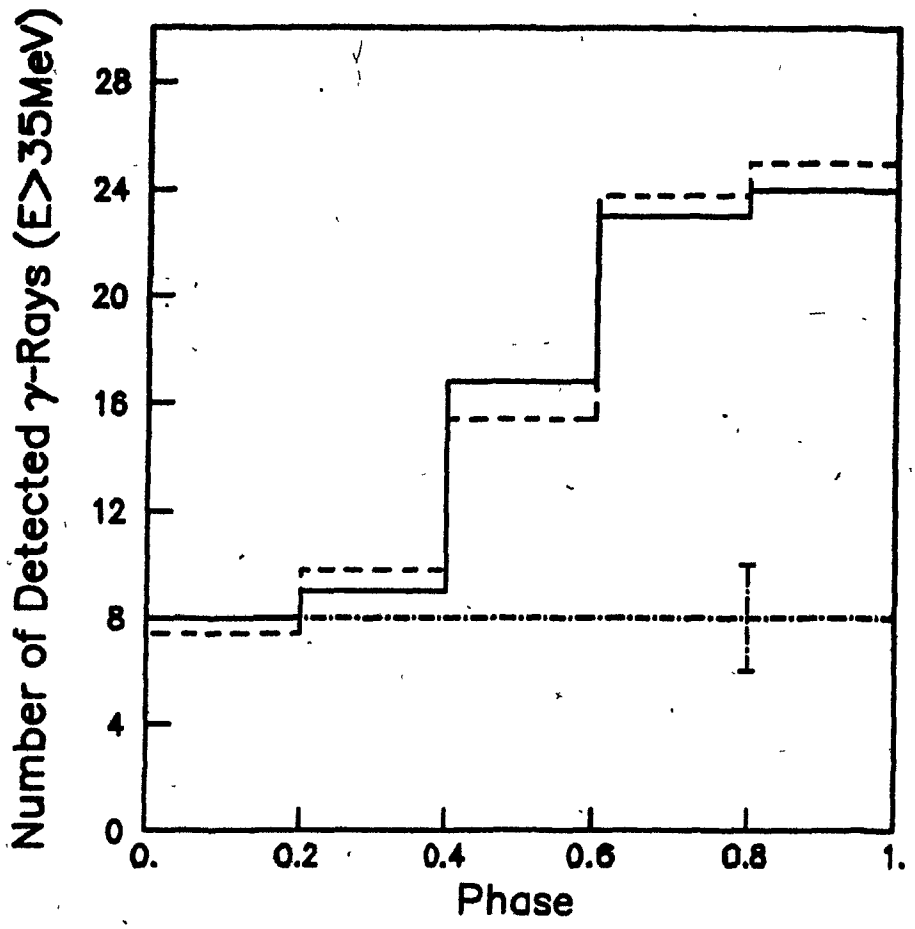

FIG 2.8: The solid line shows the distribution of arrival times of all detected γ-rays ($E > 35\,MeV$) from the region of Cyg X-3 in fractions of the ($0^d1996814 \pm 0^d0000005$) period.[17] The zero of time corresponds to the X-ray minimum defined by Parsignault et al.[18] The dashed lines show the number of γ-rays normalized to the average SAS-2 exposure to Cyg X-3. The dot-dashed line shows the estimated contribution from diffuse celestial and galactic radiation, together with its uncertainty.

After this initial study of low energy γ-rays ($E_\gamma \sim 10^8\ eV$) Cyg X-3 became an object of extreme interest. Many cosmic-ray physicists went back to analyze their data that had been collected over the years to determine if they had any evidence that Cyg X-3 was a high-energy γ-ray source.

In 1979, the Crimean group[11] published a paper in which they had analyzed six years of data taken from 1972 to 1977. They had used two $2.5\,m$ parabolic mirrors and fast photomultipliers to observe the atmospheric Čerenkov light from air showers with $E > 10^{12}\,eV$. The Crimean group found that the γ-ray fluxes did not show as nearly a sinusoidal flux as in the X-ray region, but they claimed to see two peaks at X-ray phases $0.157 - 0.212$ and $0.768 - 0.823$ (see figure 2.9). The first pulse had a statistical significance of 5.4σ, with the second having a 2.7σ significance. The pulses are separated by 0.4 of the period, occurring just before and just after the X-ray minimum. The flux recorded for the 1^{st} and 2^{nd} pulses were recorded by the Crimean group to be

$$2.8 \times 10^{-10}\ photons\,cm^{-2}\,s^{-1} \text{ and } 9.0 \times 10^{-11}\ photons\,cm^{-2}\,s^{-1}.$$

At the Mount Hopkins Observatory in southern Arizona, Helmken et al[20] studied γ-ray fluxes from several X-ray binary stars in the Cygnus system during the winter of 1976-1977. They used a $10\,m$ reflector which was multiplexed to give 10 independent $1°$ beams. No excess γ-rays from Cyg X-3 were found and that placed the upper flux limit at

$$6.5 \times 10^{-11}\ photons\,cm^{-2}\,s^{-1} \quad \text{for} \quad E_\gamma > 10^{11}\,eV.$$

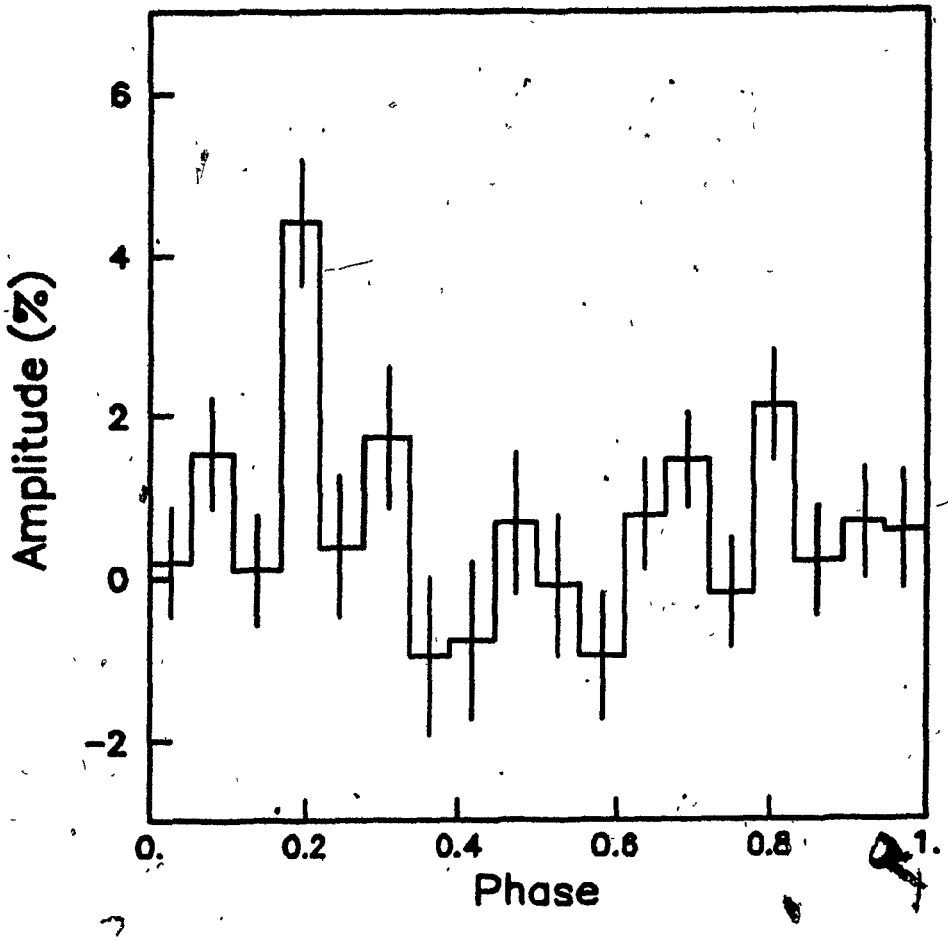

FIG 2.9: The phase histogram for gamma-ray with energy $E > 2 \times 10^{12}\, eV$ from the Crimean Group.[11]

In the early 1980's, the results of the Crimean group were confirmed by the Mt. Hopkins Observatory[21] in April, May and June 1980, and by the Jet Propulsion Lab at Edwards Air Force Base in California[22] during 29 Aug – 6 Sept. Both experiments used two mirrors with the Mt. Hopkins group using $2.5\,m$ diameter mirrors and $5\,cm$ photomultipliers, giving them a 2.0° field of view, and the JPL group having a total field of view of 2.0° and 2.8° for each mirror. Both experiments measured the background rate by looking on either side of Cyg X-3 as it passed through the field of view of the mirrors. Danaher et al.[21] observed a 3.5σ peak between 0.7 – 0.8 phase. The flux that they obtained was

$$\sim 2.5 \times 10^{-10}\, photons\, cm^{-2}\, s^{-1} \qquad \text{for} \quad E \geq 10^{12}\, eV.$$

Lamb et al.[22] found a 4.2σ excess in the phase between 0.5 and 0.7. They gave a flux averaged over the entire cycle as

$$\sim 8 \times 10^{-11}\, photons\, cm^{-2}\, s^{-1} \qquad \text{for} \quad E \geq 10^{12}\, eV.$$

The results of both these experiments are shown in figure 2.10.

Ultra-high energy (UHE) γ-rays ($E_\gamma \geq 10^{14}\, eV$) can be detected by extensive air shower arrays. The first evidence that Cyg X-3 was a UHE γ-ray source came from the EAS array at Kiel[23] in 1983. The EAS experiment (located at sea level) consisted of $28 - 1\,m^2$ area scintillation counters located at distances up to $100\,m$. The detectors could provide information on the shower core, shower size N_e, and the age parameter s. They used the fast-timing technique to determine the direction of the shower front.

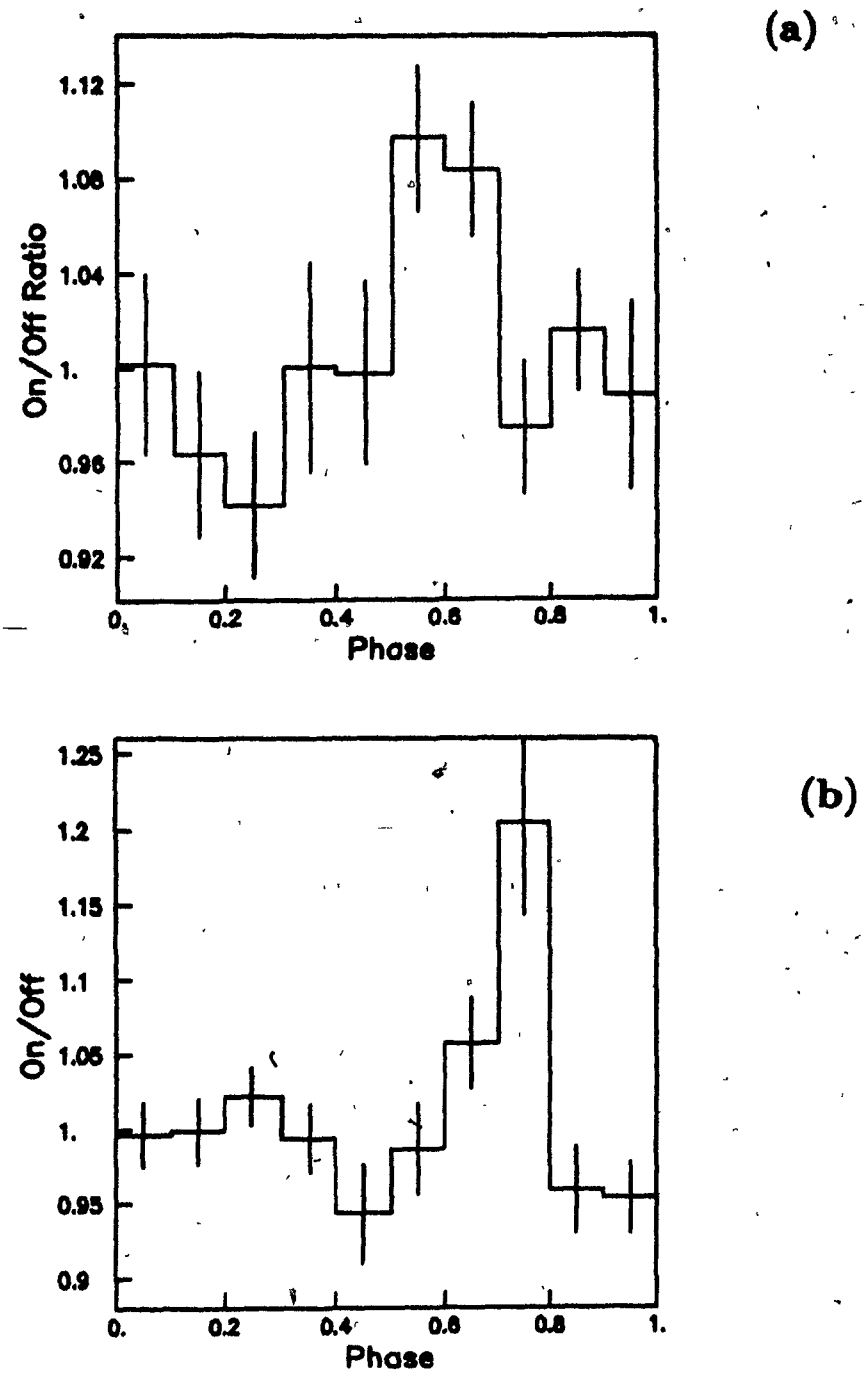

FIG 2.10: Phase histogram of γ-ray emission from Cyg X-3. a) Mt. Hopkins, b) JPL.

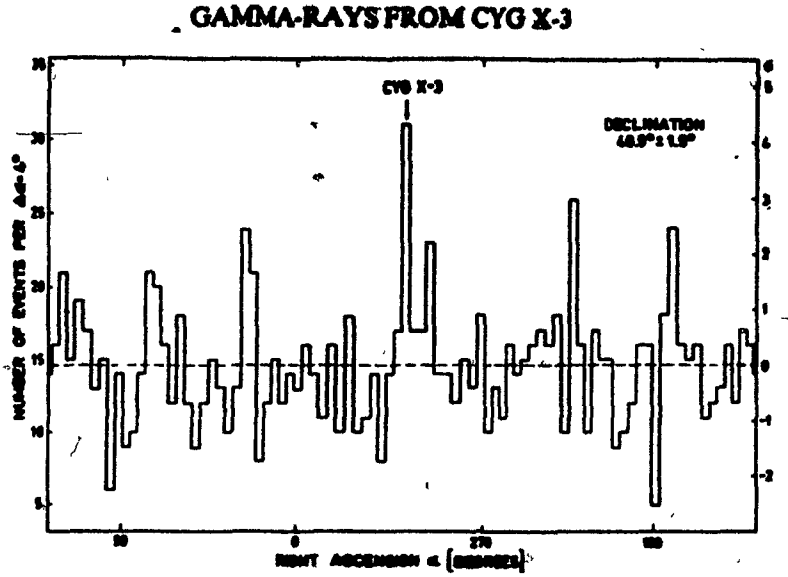

FIG 2.11: Number of extensive air showers detected by the Kiel group of size $n_e \geq 10^5$ particles and age parameter $s \geq 1.1$ in the declination band $40.9^0 \pm 1.5^0$ as a function of right ascension. The dashed line represents the average number of showers per bin over the total band.

The data was taken over a 4 year span from March 1976 to January 1980, however the effective viewing time of Cyg X-3 was only 3,838 hours. As discussed earlier, a nucleonic shower can be identified if the measured value of the age parameter differs greatly from the one expected for it from electro-magnetic cascade theory. So, to decrease their background events by a factor of 2, they considered only the showers with an age $s \geq 1.1$ to be γ-rays initiated showers. The results of their analysis is a 4.4σ excess above the average off source background shown in figure 2.11. When this excess was folded into the $4.8\,hr$ period, the peak occurred at the .4 phase. The flux averaged over the entire phase was given as

$$(7.4 \pm 3.2) \times 10^{-14}\ photons\ cm^{-2}\ s^{-1} \qquad \text{for} \quad E_o \geq 2 \times 10^{15}\ eV$$

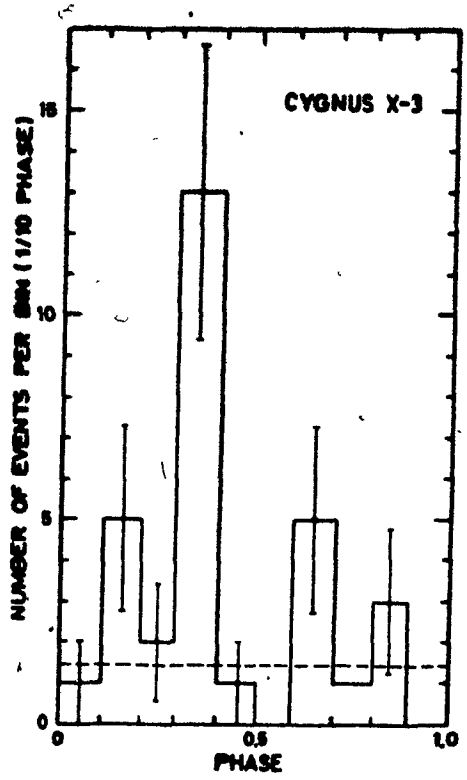

FIG 2.12: Phase histogram of the arrival times of extensive air showers of size $N_s \geq 10^5$ particles and age parameter $s \geq 1.1$ from the direction $\delta = 40.9^0 \pm 1.5^0$ and $\alpha = 307.8^0 \pm 2.0^0$. The phase parameters used are those given by Parsignault et al.[18] Error bars represent $\pm 1\sigma$ statistical errors. The dashed line corresponds to the average off-source rate of 1.44 ± 0.04 showers per bin.

and

$$(1.1 \pm 0.6) \times 10^{-14}\ photons\ cm^{-2}\ s^{-1} \qquad \text{for} \quad E_o \geq 10^{16}\ eV.$$

Their results are shown in figure 2.12. It should be noted that the Kiel group did **not** observe a low fraction of muons in their UHE photon sample.

The Kiel results were subsequently confirmed at Haverah Park[24] in the U.K.and Akeno[25] in Japan in 1983 and 1986 respectively. At Haverah Park, four water Čerenkov counters were used with 3 of the detectors placed on the circumference of a $50m$ circle and the 4^{th} detector located at the center. The array is sensitive

to the range of $10^{15} - 10^{16}\,eV$. Because of the large size of the Čerenkov counter ($13.5\,m^2 \times 1.2\,m$) and slow phototubes, the expected angular resolution was $\sim 3°$. The background was measured by looking on either side of Cyg X-3. The excess flux from Cyg X-3 averaged over the $4.8\,hr$ phase is given as 1.7σ. They attribute this low significance to their low angular resolution. However, when the γ-rays from Cyg X-3 were folded into the $4.8\,hr$ period, a sharp peak occurred at $0.225 - 0.25$ phase. The intensity was given as

$$\sim 1.5 \times 10^{-14}\ photons\,cm^{-2}\,s^{-1} \qquad \text{for} \quad 10^{15}\,eV \leq E_\gamma \leq 10^{16}\,eV.$$

At Akeno, the EAS array consists of 153 $1\,m^2$ scintillation counters and nine muon detectors with an overall area of $9 \times 25\,m^2$. The data was recorded from early 1981 to September 1984. They obtained an angular resolution of 3° for the arrival direction of the shower. The ratio of the percentage of muons to electrons ($R = N_\mu/N_e$) was used to select data in favor of γ-rays against the charged particle initiated showers. If $R \geq 0.001$ the shower data was rejected. The integral flux obtained was

$$1.1 \times 10^{-14}\ photons\,cm^{-2}\,s^{-1} \qquad \text{for} \quad E_0 \geq 10^{15}\,eV$$

and

$$8.8 \times 10^{-14}\ photons\,cm^{-2}\,s^{-1} \qquad \text{for} \quad E_0 \geq 6 \times 10^{14}\,eV.$$

Other observations of Cyg X-3 shows the sporadic nature of the γ-ray fluxes. On 17 June 1985, the Fly's Eye atmospheric Čerenkov detector[26] found a 3.1σ effect on γ-rays $\geq 10^{13}\,eV$. In 1985 the Baksan air shower array[27] observed a 40% increase in

the number of detected air showers from Cyg X-3. This excess occurred following a large radio flare on 9 October 1985. A summary of the observations of Cygnus X-3[24] showing the detected phases (relative to the x-ray minimum) and the time-averaged integral γ-ray flux above $10^{11} eV$ is shown in figure 2.13.

Cyg X-3 is not the only emitter of UHE γ-rays. The Buckland Park Air Shower Array in Australia,[28] measured an excess of γ-ray showers coming from Vela X-1[29] in the southern hemisphere. They used 5 fast-timing counters to obtain an angular resolution of 2°, and cut all the showers which had an age less then 1.3. When the data was folded into the $8^d.96411$ period, they obtained a 4 sigma spike at 63°.

The Fly's Eye detector[30] found evidence for $5 \times 10^{14} eV$ γ-rays from the X-ray binary Hercules X-1. They used 67 mirrors to study the atmospheric Čerenkov light from the incoming electrons. Their angular resolution was 3.5°, therefore they centered their viewing range to a 7° circle centered around Hercules X-1. They obtained a 1.8σ excess of γ-rays from Hercules X-1. When the data was folded into the 1.24 period of the X-ray spectrum, it was found that only the data taken early in the night of 11 july 1983 had any significant results. These results are shown in figure 2.14. The flux calculated for this period is given as

$$\sim 3 \times 10^{-12} \, photons \, cm^{-2} \, s^{-1} \qquad \text{for} E_\gamma \geq 5 \times 10^{14} \, eV.$$

Currently there are more EAS experiments being proposed and/or built to specifically study high energy γ-rays sources. Our experiment at McGill university is an air shower array (LEDA) which is composed of 19 $1\,m^2$ liquid scintillator detectors

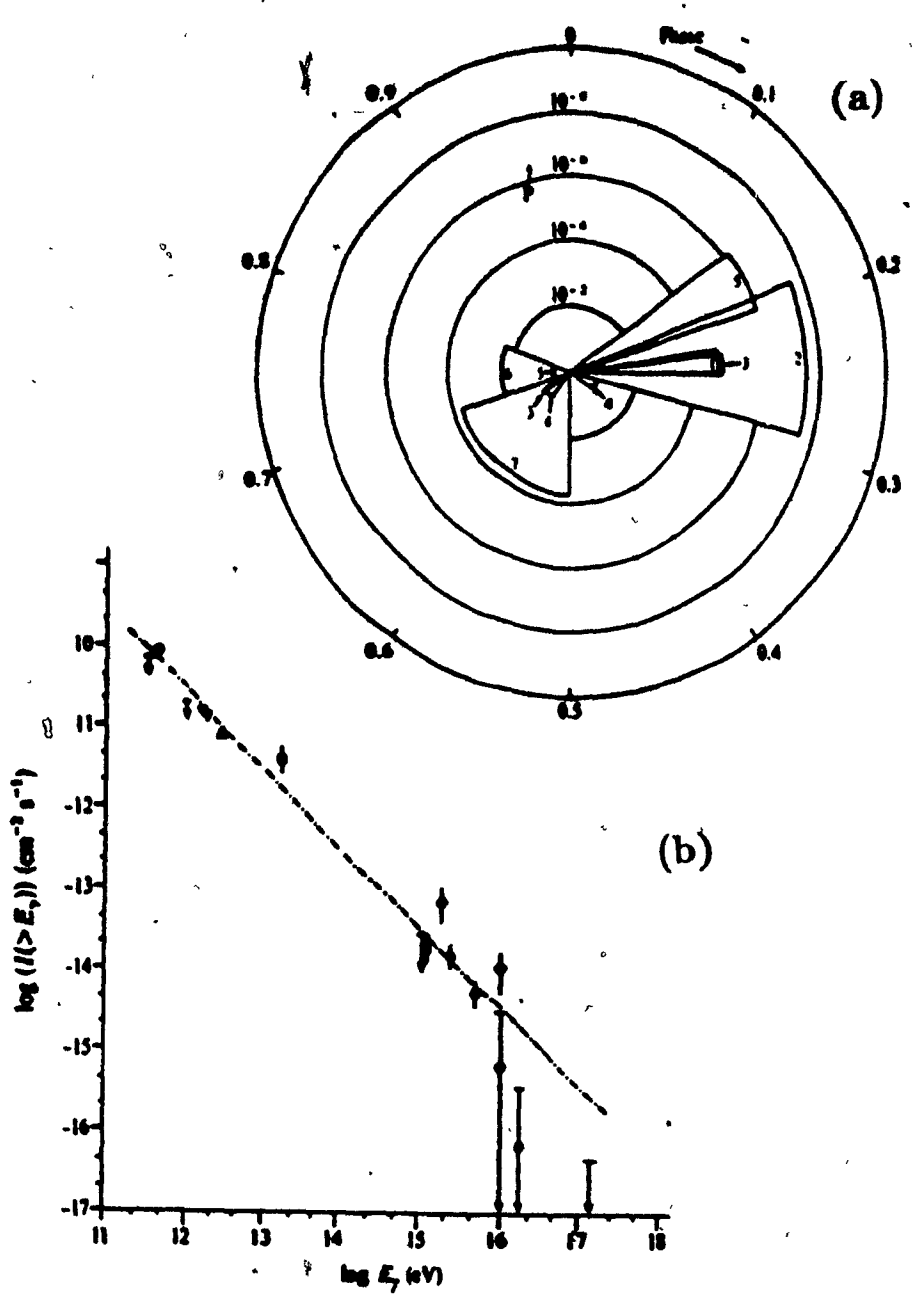

FIG 2.13: a) A summary of the phases (relative to X-ray minimum) for pulsed emission above 500 GeV from Cygnus X-3.[24] The numbered sectors, 1-7, are taken from refs 24, 22, 22, 48, 49, 20, 21 respectively. The probability of each measurement occurring by chance has been estimated from the cited references (where not explicitly stated) and is plotted radially. b) The time averaged-integral γ-ray flux above 10^{11} eV from Cygnus X-3. Source of measurements: $\circ$, ref 21; $\bigtriangledown$, ref 49; $\bigtriangledown$, ref 20; $\bigtriangleup$, ref 50; $\sqcup$, ref 48; $\diamond$, ref 22; $\bullet$, ref 24. The dotted line is an estimate of the spectral slope between 5×10^{11} and 5×10^{15} eV.

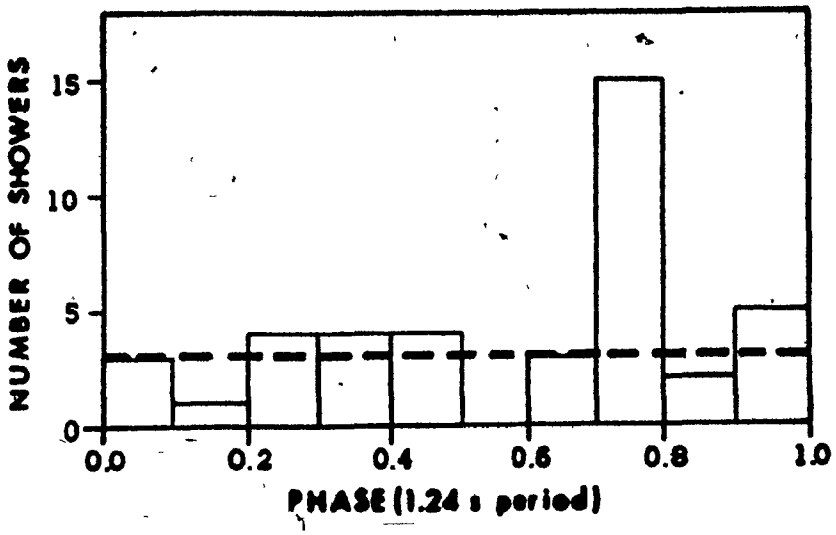

FIG 2.14: Phase dependence of the shower arrival times for the first half of the data received on 1983 July 11 at the Fly's Eye Detector. The dashed line is the expected number of events in each bin.

arranged in a uniform hexagonal array with a radius of 86 m. The direction of the shower front will be found using the fast-timing technique, and γ-ray showers will be determined by the age parameter, in a method similar to the Kiel experiment.[23]

An air shower array consisting of 64 detectors in a $100\,m \times 100\,m$ square at Notre Dame[31] GRAND^{TM} (Gamma Ray Astrophysics at Notre Dame) is being built with four layers of multi-wire proportional chambers (MWPC) in each detector. There will be a steel shield over the 4^{th} MWPC which will be used to differentiate between electrons and muons. The direction of the shower will be determined by the direction of the incoming particles measured by the MWPC. The γ-ray showers can be determined by making cuts on the ratio of N_μ/N_e.

An ambitious project to build an air shower array (CASA) (Chicago Air Shower Array) at Fly's Eye in the Utah desert has been proposed by Jim Cronin in Chicago.[32] They propose to build 1064 $1.5\,m^2$ scintillator detectors placed on a square grid with a $10\,m$ spacing between each detector. Shower directions will be determined by fast-timing techniques. This will operate in conjunction with a muon detector array built by the University of Michigan.[32] These muon detectors will be used to help determine the γ-ray initiated showers by the ratio N_μ/N_e.

Models

With all the data obtained in the last 10 years on the γ-ray ray fluxes from Cyg X-3, theoreticians have been pressed into finding models which would describe the production of the UHE γ-rays. An obvious constraint on the models for the origin of the UHE radiation is that it must reproduce the light curve, which is the intensity of γ-rays as a function of the time within the period of the pulsar. The observations to this date do not justify an assumption of a steady direct γ-ray source because the shape of the UHE light curve cannot be reproduced by merely eclipsing this source, which would give a relatively flat light curve with a single flat eclipse. Some mechanism is needed to accelerate charged particles, which would then produce UHE γ-rays. The period of UHE, X-ray, and UV light from Cyg X-3 are all equivalent, which implies that the modulation is produced by orbital motion. What accelerates these particles must be inferred by the UHE γ-ray spectrums.

W. Vestrand and D. Eichler proposed that Cyg X-3 is a young pulsar in a close

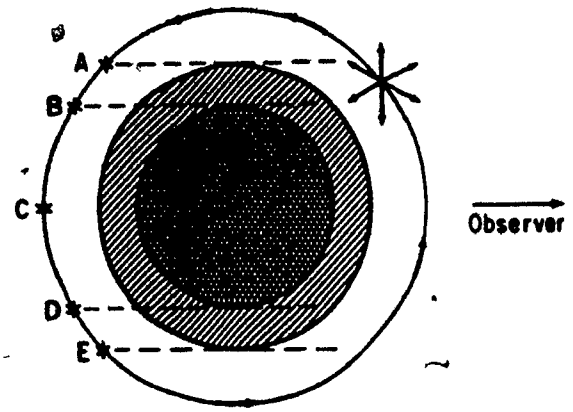

FIG 2.15: Schematic representation of how the UHE light curve can be generated based on the model proposed by Vestrand et al. The cross-hatched region denotes the main body of the companion, and the circumscribing shaded region denotes its atmosphere. The outer circle represents the pulsar orbit, and the dashed lines represent particle trajectories that produce γ-rays detectable at Earth. Pulses are produced when the pulsar is between A and B and between D and E. X-ray minimum occurs at position C.

binary system. They argue that the radiating particles are ionic, and that they are accelerated isotropically by the rotational energy of the pulsar.[33] The companion star then acts as a target material for the particles accelerated near the pulsar, and generates π^0 or bremsstrahlung γ-rays by the proton-proton collision with gas in the atmosphere.[34] Figure 2.15 demonstrates how two sharp pulses of γ-rays will be observed on earth. The pulse width is directly proportional to the gas width of the companion star. This model unfortunately cannot account for $E_\gamma \geq 10^{16}\,eV$.

An alternate model was proposed by G. Chanmugan and K. Brecher[35] in which

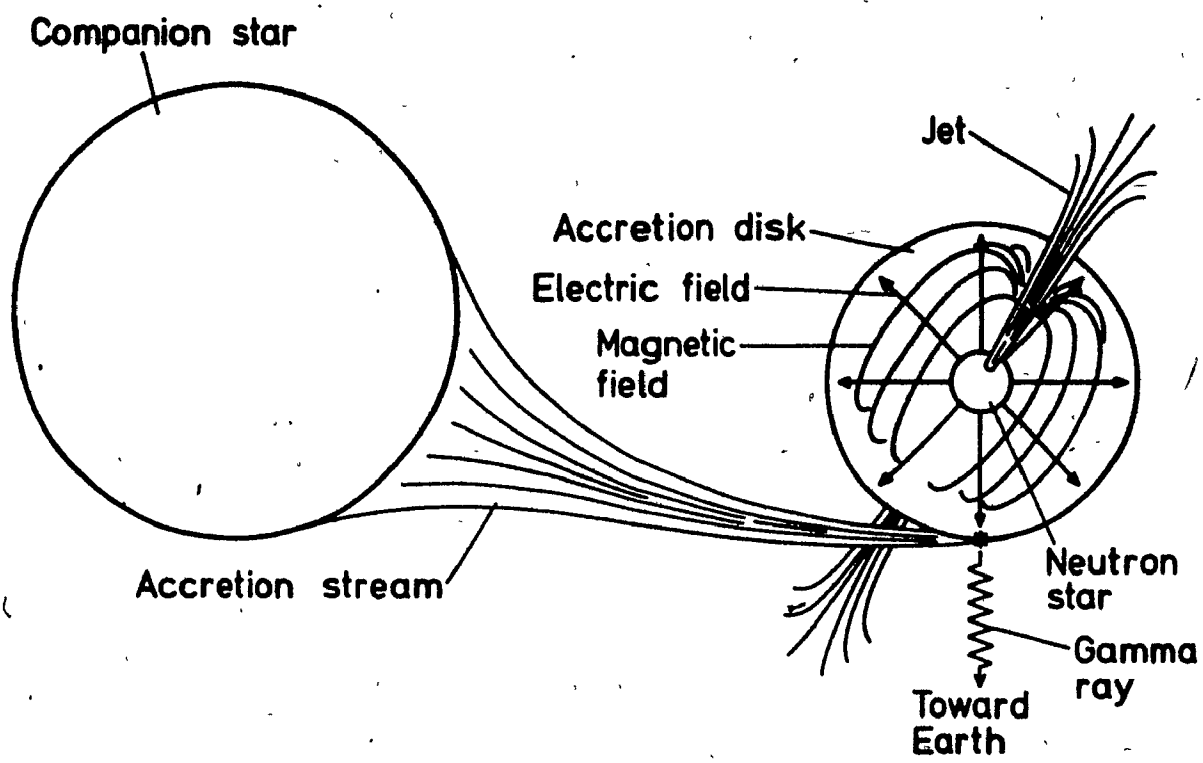

FIG 2.16: Schematic diagram for the production of UHE γ-rays based on the model proposed by Chanmugan et al. The gasses from the companion star form an acretion disk around the neutron star. The large magnetic fields of the neutron star will accelerate particles within the accretion disk. The γ-rays will then be formed in the same manner as was proposed by Vestrand et al.

the energy source is an accretion disk *surrounding* the neutron star. The accreting matter forms a differentially rotating accretion disk around the degenerate star, the ambient magnetic field becomes amplified, and if the accretion disk is highly conducting, an observer in a non-rotating inertial frame will see an electric field which is a function of the distance 'r' from the neutron star. A tacit assumption of this model is that the magnetic field will remain anchored in the disk and create the large scale structure. Because the electric field is a function of the distance r, high potential differences will form in the accretion disk, even though it has a lower magnetic field intensity than the pulsar. These high voltages will produce accelerated charged particles in a jet in the $\pm z$ directions (see figure 2.16) To obtain the $4.8\,hr$ modulation effect, Chanmugan et al. also proposed that the neutron star has a highly-inclined magnetic axis. The γ-rays are then formed in the same manner as was described in W. Vestrand's's model.

Again, another theory involving the accretion disk as the accelerating medium was proposed by D. Kazana and D.C. Ellison.[36] Their theory suggests that charged particles are accelerated in the accretion disk by first order Fermi shocks created when plasma accretes onto the compact object. The shocks form because accretion velocities are much higher than the thermal velocities of the accreting matter. Neutrons are formed in the accelerating area by $p + p \rightarrow n + X$. The production of the neutrons is crucial because it allows the transport of energy away from the acceleration site without invoking special magnetic field configurations. The neutrons can then, by

interaction with the stellar companion, produce the narrow (in-phase) UHE γ-ray pulse by making π^0's which decay to highly collimated γ-rays.

The above models were derived to represent the steady production of γ-rays. However, it was seen that γ-ray bursts can occur. Milgrom and Pines[37] suggested that instability in the 'pulsar surrounded by an acretion disk' system may initiate the radio outburst; and such an instability may also be able to produce UHE particles that fill the inner regions of the system. They would then interact with the ambient photon field and produce phase independent UHE γ-ray emission.

The theoreticians' models must satisfy the results found by experimentalist, in particular, the energy spectrum and light curve of the UHE γ-rays. However, this information is sketchy at present and there needs to be more 'hard' physical evidence which could then either confirm some theories, or disprove them.

3.0 COSMIC RAY COUNTER

3.1 Description of the Detector

When we designed the detector for our EAS experiment, we wished to satisfy the following conditions:

(1) The detector should be inexpensive and easy to construct, so that the number of detectors that could be built within a fixed budget would be larger than that for more expensive detectors.

(2) The detector has to be able withstand large temperature changes due to the harsh Canadian weather conditions ($-40\,^\circ$ winter $\rightarrow 30\,^\circ$ summer).

(3) Since the energy of the primary cosmic ray can only be determined indirectly by measuring the lateral spread of the particles at ground level, it is necessary to have a good pulse-height resolution to insure an accurate measure of the density of particles.

(4) Because there are time differences within the shower front due to multiple coulomb scattering of the electrons in the atmosphere, have sufficient detector area to ensure a high probability of intercepting the earliest particles.

(5) The detectors should be built in such a way that they can easily be accessed or repaired should a malfunction occur.

Our final design[38] is shown in figure 3.1. Our detector is a simple design comprised of: a plywood base mounted on four $10 \times 10\,cm$ posts sunk into the ground ($\geq 1\,m$ to prevent frost heaving effects), an acrylic vacuum-formed tray with an ef-

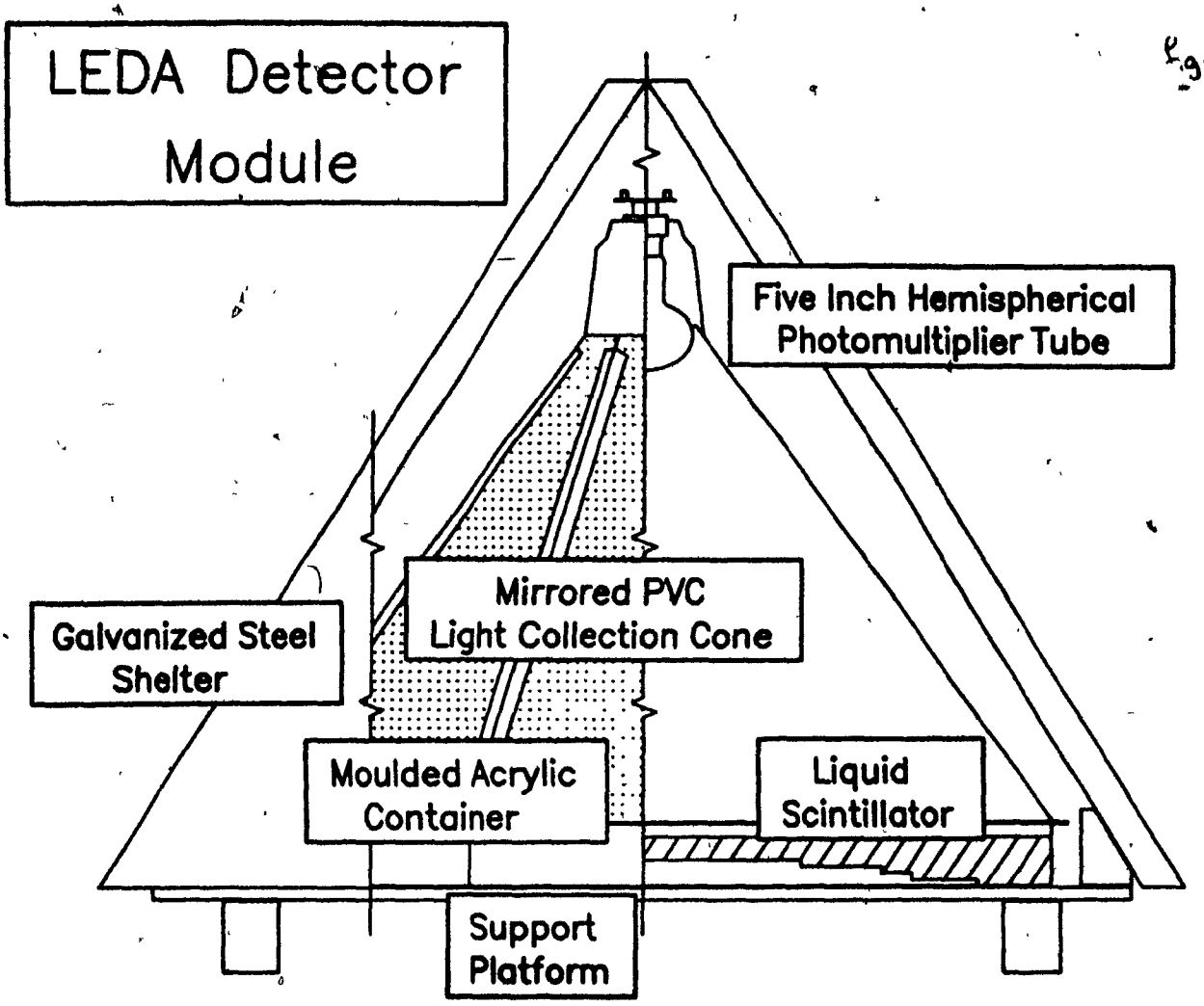

FIG 3.1: A cut away diagram of the LEDA detector.

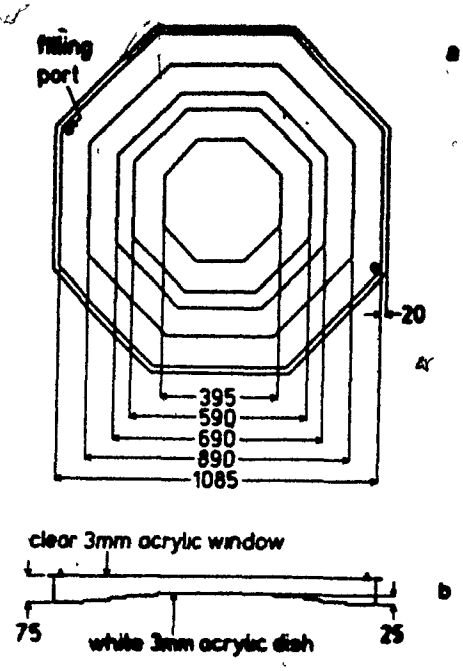

FIG 3.2: (a) Plan view of the acrylic dish used to contain the liquid scintillator for the counter. The distances shown are in mm and in total area is approximately $1\,m^2$. (b) A cut through the centre of the scintillator dish, illustrating the structured bottom. The steps are approximately $6\,mm$ each and are used to smooth out the response of the counter to particles traversing it at different distances from the centre.

fective area of $1\,m^2$ in which there is placed 45 litres of liquid scintillator, a light collection cone, made of polyvinylchloride (PVC) with aluminized mylar glued to the inside to improve the reflectivity, a Hamamatsu R2218 photomultiplier tube (PMT) located at the apex of the light collection cone, black plastic sheeting to make the detector light-tight, and finally a galvanized steel pyramid to protect the detector from snow and rain.

To improve the pulse-height resolution, the scintillator tray is constructed such that the thickness of the liquid scintillator is not uniform throughout the detector (see figure 3.2). Thus, the varying amounts of light output from the scintillator is

exactly compensated for by the light collection efficiency of the cone. Supporting blocks are placed underneath the central portion of the tray to inhibit any sagging that may occur due to the weight of the liquid scintillator. The octagonal shape of the tray was chosen because it was easy to construct by vacuum forming techniques, and because of its nearly circular shape, the positional dependence of light collection and timing can be considered purely radial to a first order approximation. The tray is partially translucent, so a sheet of aluminized mylar is placed underneath to reflect any photons that should happen to pass through.

We used liquid scintillator because, not only is it cheaper than *all* plastic scintillators, but it also has has a higher light output, which improves our timing resolution. The decay time ($\sim 2-3\,ns$), is faster than the *cheap* plastic scintillators (acrylic based), but slower than the expensive plastics (polyvinyltoluene). The liquid scintillator was designed specifically for our experiment to withstand cold temperatures.[38] Because the light output from liquid scintillator is reduced if it is exposed to oxygen, great care must be taken when using this product. The top of the scintillator tray is sealed with a clear acrylic top with two gas ports. Before the tray was filled with the scintillator, all the oxygen was purged by pumping dry nitrogen into one port while the other port was left open. To fill the tray, liquid scintillator is siphoned through a rubber tube into the opened gas port by pumping nitrogen into the barrel containing the scintillator. A $2-3\,cm$ gap of nitrogen remains between the top of the scintillator and the top of the tray which allows the scintillator to expand or contract, due to

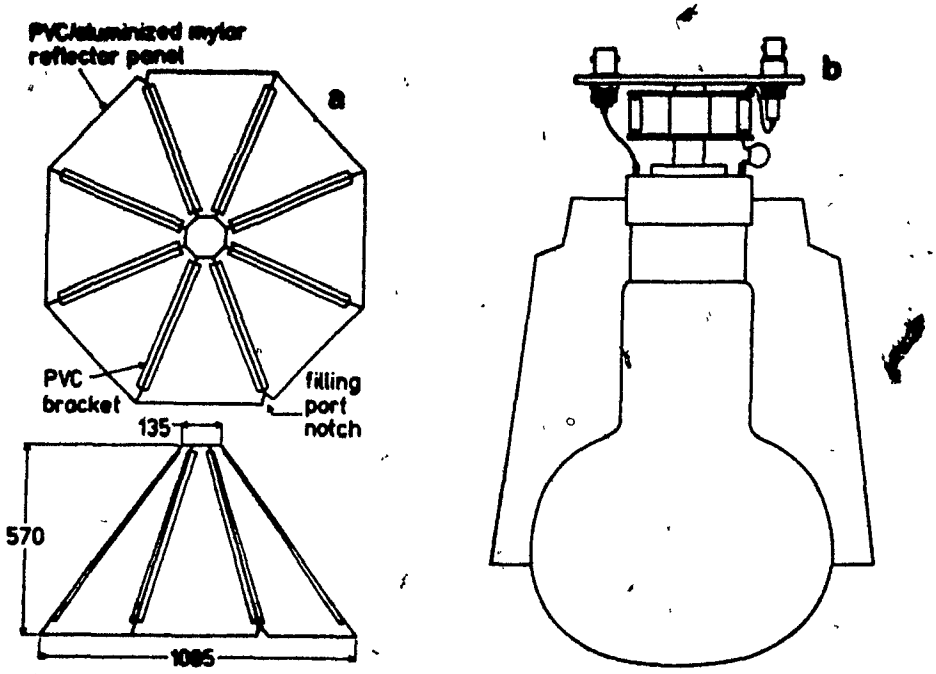

FIG 3.3: (a) Plan and side view of the light collection cone developed for this counter. The reflector panels are held together with pvc brackets to form a self-supporting structure which rests on the scintillator dish. (b) A cut through the centre of the phototube mount. The base is attached to an inverted PVC cup which rests on the light collection cone, suspending the phototube above the centre of the scintillator dish.

temperature changes, without damaging the tray itself.

The light cone is an octagonal pyramid with a base length of 1085 mm, a height of 570 mm, and a 135 mm opening at the top (see figure 3.3). It is made from eight equilateral triangles of PVC held together with brackets made from the same material. The inside of the light cone is covered with aluminized mylar to act as a reflector. Experiments have been done[39] which show that the aluminized mylar is as effective as mirrored acrylic or as the best commercially available high gloss white paint. The PMT is placed at the top of the pyramid using a plastic holder to keep it secure. It is 12 cm in diameter, it has venetian blind dynodes, 13 stages, and it has a hemispherical

Bialkali photo-cathode. The quoted rise time for a single photon is 6.5 ns.[40]

Once the detector is completed, it is covered by a thick black industrial plastic to exclude any stray outside light. The plastic is stapled onto the wooden support frame to hold it in position. Then a thin (14-gauge), galvanized steel pyramid, with its joints sealed with duct tape to weather-proof it, is placed over the entire arrangement and screwed onto the wooden base. The cables leading to the PMT are passed through a small hole in the bottom of the base. Figure 3.1 shows the assembled detector.

TABLE 3.1

Electronic Modules

abbreviation	description	model #
ADC	analog to digital converter	LeCroy 2249W
TDC	time to digital converter	LeCroy 2228A
DISCR	octal discriminator	LeCroy 623B
FI/FO	logic fan in / fan out	LeCroy 429A
GATE GEN	gate generator	LeCroy 222
HV	high voltage supply	LeCroy HV4032A

The electronics used are standard LeCroy ADC's, TDC's and discriminators. The modules and the model numbers are listed in table 3.1 The ADC and TDC modules are housed in a standard CAMAC crate and the data is read out via a Kinetic Systems LSI-11/2 computer (contained in the same crate) with the RT11FB operating system. Data is temporarily stored on floppy disk, and when the disk is full, the data is transferred over the phone lines to the VAX 785 (located in the Physics Department at McGill) for further analysis. Different electronic configurations were

used at varying stages of our experiment and they will be illustrated as required.

3.2 Timing Resolution

The timing resolution of our detector is based upon a combination of: the light output from the scintillator, the decay time of the scintillator, the geometry of the light cone, time slewing due to differences in pulse-heights, and the response of the PMT.

To calibrate our detector we needed some method of triggering the electronics, as well as some method to locate the position of the incoming cosmic ray so that the radial variance of the time could be measured separately from the other concerns. In order to determine the location of the incoming cosmic ray, we used two small ($7cm \times 9cm$) plastic scintillators and fast PMT's, one on top of the other. This was placed directly underneath the liquid scintillator tray to insure that we only detected the vertical cosmic rays. The pulse from the PMT was recorded only if a signal was also recorded from both plastic scintillators (A & B). A block diagram of the electronics is shown in figure 3.4. The ADC gate, and the TDC start pulse are generated by the ANDed outputs from the A & B discriminators. The discriminator threshold levels were set to $30\,mV$ to minimize the time-slewing effects, which will be discussed later, and the pulse width was adjusted to its maximum setting of $150\,ns$, so that the delayed PMT pulse would be properly integrated by the ADC. B is delayed by $3\,ns$ with respect to A so that it will always complete the coincidence, thus minimizing jitter in the start time. Thus, the recorded time from the PMT is the time it takes for the light to travel from the scintillating liquid to the PMT, plus or minus a fixed

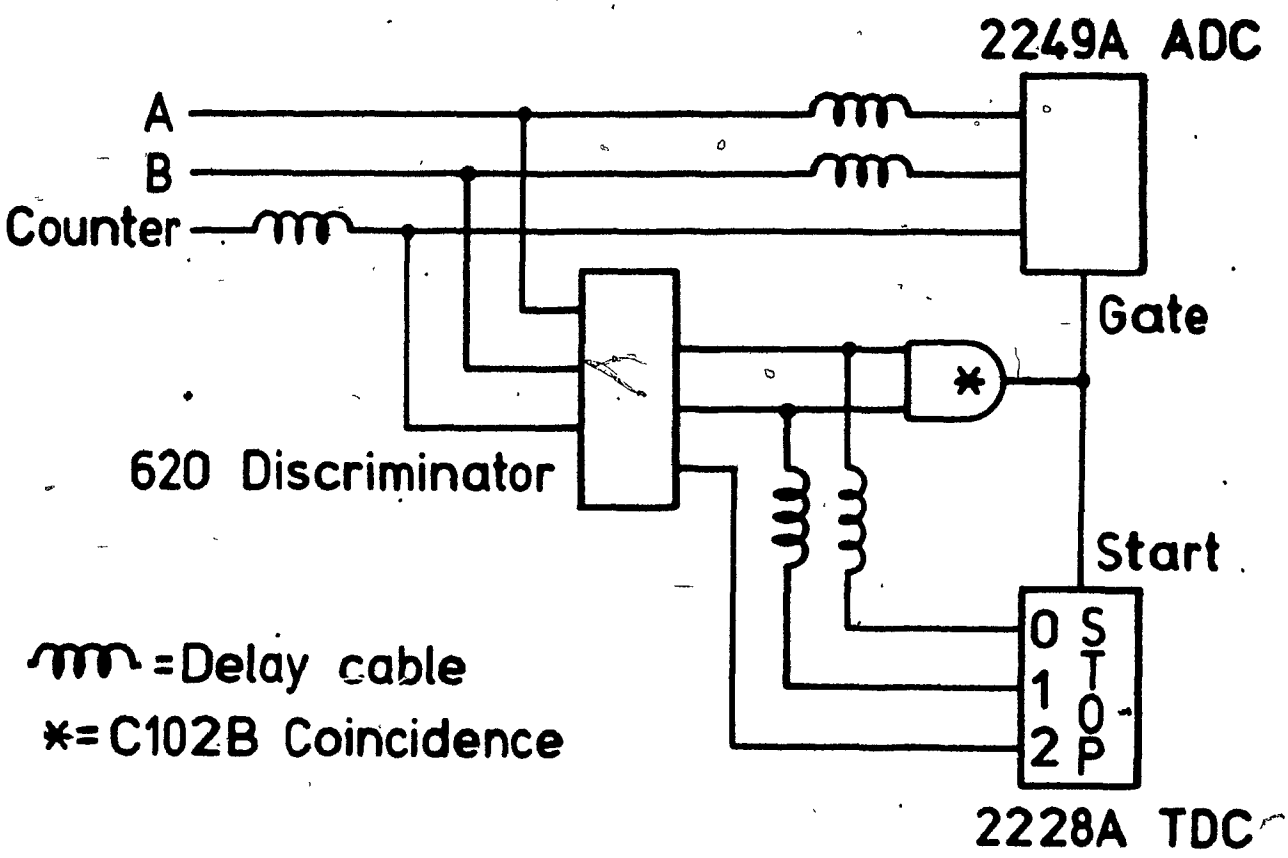

FIG 3.4: A block diagram of the electronics used in the time-slewing measurements. A and B are the signals coming from the trigger counter placed directly beneath the larger detector. C is the signal coming from the PMT. The start of the TDC and the gate for the ADC are generated by the logical function $A \cdot A$

time interval, depending on the delay cables used.

Time Slewing

The effective time is a function of the pulse-height, (time slewing) since the stop pulse is generated only *after* the pulse has passed the discriminator threshold. This is demonstrated in figure 3.5. Larger pulses have steeper slopes (usually referred to as a faster slewing times) which will cause the stop pulse to be generated Δt before a similar, although smaller pulse would, even though the pulses are generated at the same instant in time. The effect of this relationship between the pulse-height and time had to be found so that it could be corrected for in the off-line analysis. Theoretically the relationship is of the form:

$$time \propto pulseheight^{-n}$$

To determine the approximation for n, we recorded the pulse-height and time for each cosmic-ray that passed through the detector. These were then plotted (see figure 3.6) on two scatter plots with *time* as a function of ph and $1/\sqrt{ph}$ respectively. From these plots it can be seen that $n = \frac{1}{2}$ is a good approximation. Thus the equation used to find the time-slewing effect is given by:

$$t = a/\sqrt{ph} + b \qquad 3.1$$

To find the constants a and b, the time versus pulse-height information was analyzed in the following manner. After a scatter plot was created of t vs $1/\sqrt{ph}$, it was reduced to ten data points, each with a mean and standard deviation. This was

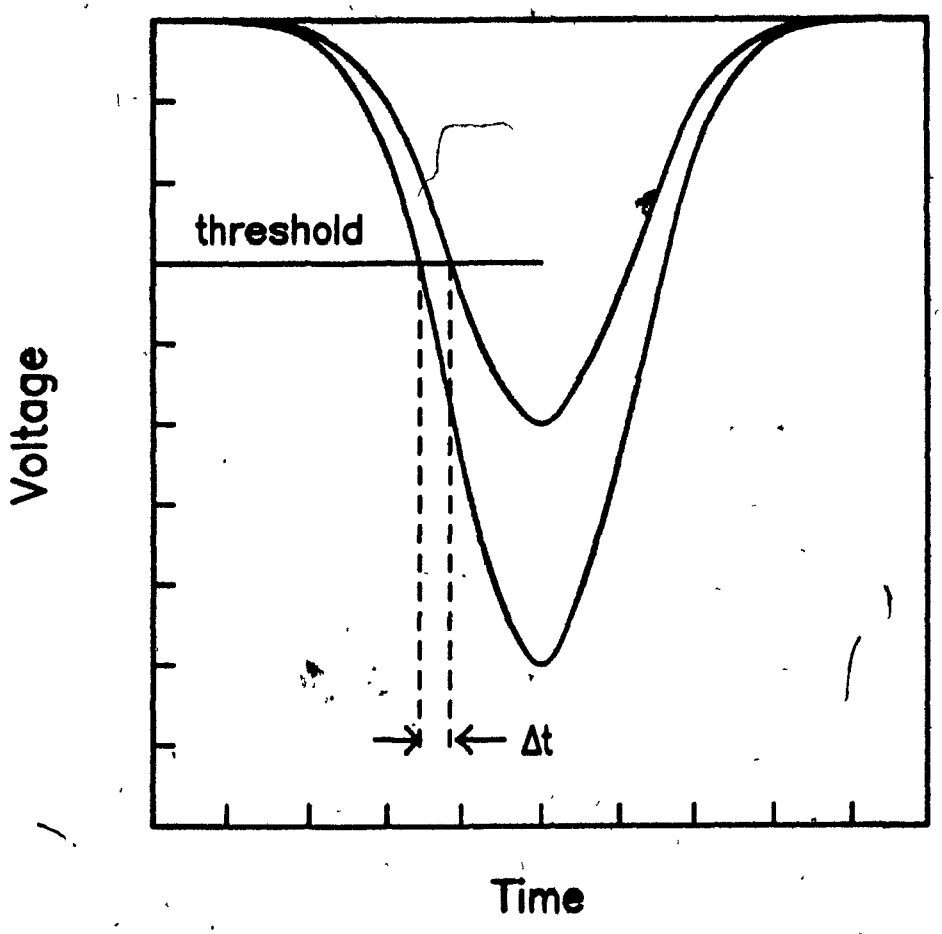

FIG 3.5: A demonstration of the time-slewing effect for two arbitrary pulses.

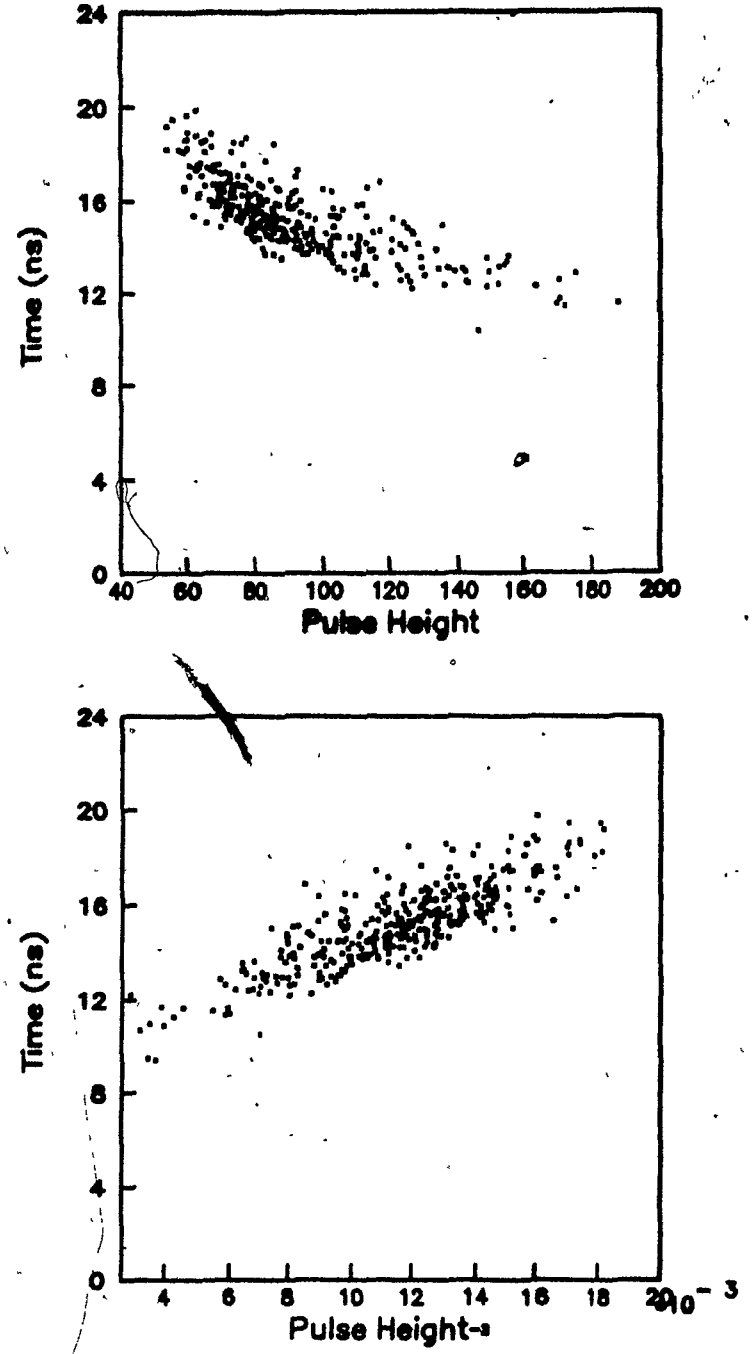

FIG 3.6: (a) The results of the recorded time (in ns) of the PMT as a function of the pulse-height (given in ADC channels). The shape of this plot is an effect of the time-slewing. (b) The same data as in part a, but plotted as time vs $1/\sqrt{ph}$.

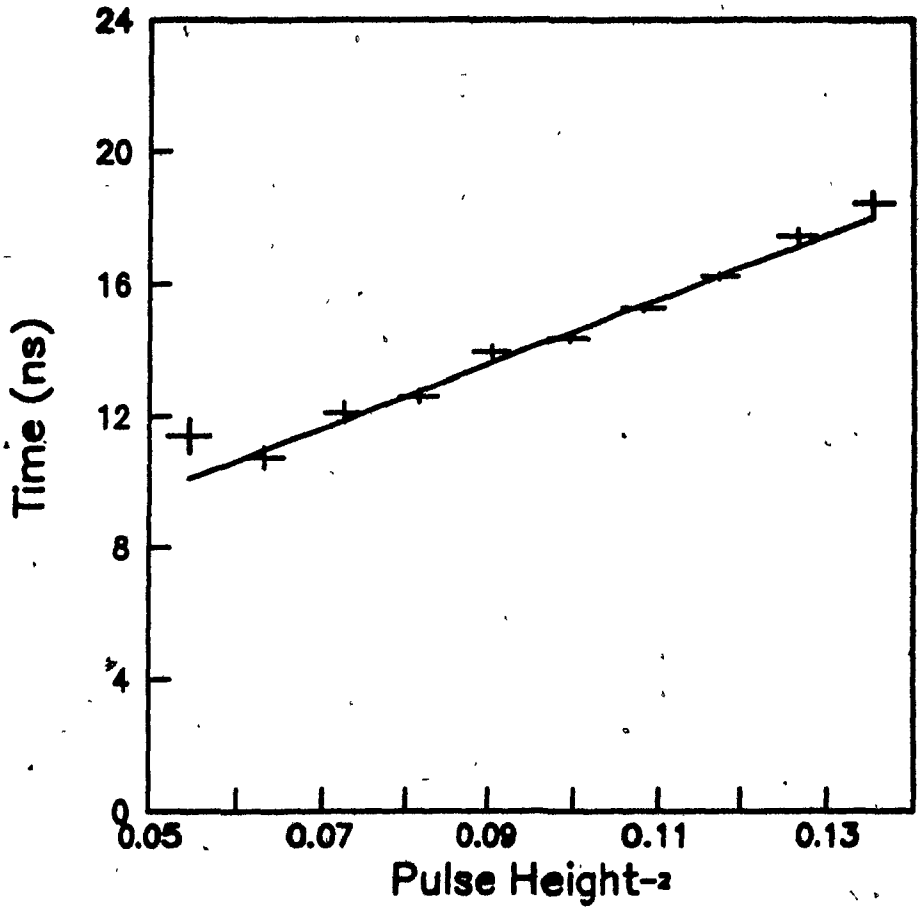

FIG 3.7: The results of the 'slicing' the previous plot into 10 distinct data points and fitting a straight line to obtain an expression for time-slewing corrections.

achieved by *slicing* the scatter plot into ten equal portions, each slice being parallel to the time axis. Thus for a given range of pulse-heights, where the range is a function of the width of the slice, a histogram of the time distribution was formed. The mean and standard deviations of the time were then calculated directly from each of the ten histograms formed. These data points (illustrated in figure 3.7), were then fit, using the least squares method, to equation form 3.1 to find the proportionality constant and intercept.

With the high voltage on the PMT set to $1425\,V$, a and b were calculated to be $(97.5 \pm 1.5)\,ns/\sqrt{ph}$ and $(11.5 \pm 0.1)\,ns$ respectively. However, when the high voltage was increased by $75\,V$, the value of a was changed to $(110.0 \pm 1.7)\,ns/\sqrt{ph}$, an increase of 12.9%. The value of b did not change within the limits of uncertainty. The change in the slope (a) may be due to the fact that the voltage increase subsequently increased the pulse-height spectrum. Equation 3.1 is only an approximation, and it may not hold over an extended range of pulse-heights. Without changing the electronic configuration, the slope was also calculated for three different PMT's. It was found that each photomultiplier gave a different response, and hence it was concluded that each detector must be tested individually before it is used in our array.

Timing Dependence on Radial Position

Because of the geometry of the light collection cone, the photons that originate at the edge of the tray have a longer and different path lengths than the photons that originate at the center of the tray. Therefore, the measurement of the 'absolute time'

is not constant as one passes from one side of the tray to the other.

To determine the radial dependence of the time, the trigger counter was placed in the centre of the detector (denoted by $0\,cm$), and then from 5 to $50\,cm$ at $5\,cm$ intervals. For each position of the trigger counter, the slope and the intercept of equation 3.1 was calculated in the same manner as described in the previous section. By comparing each line from the various positions it was found that the slope of the line varied by a maximum of 4.5%, and the intercepts varied by up to 25%.

The variations in the slopes with respect to the radial position were not statistically significant so it was decided that the slope should be constrained to be the same for all positions in the detector. To do this, the the following function was minimized.

$$\chi^2 = \sum_{j=1}^{11} \sum_{i=1}^{10} \frac{\left(t_{ij} - a/\sqrt{ph_{ij}} - b_j\right)^2}{\sigma_{ij}^2} \qquad 3.2$$

where:

i labels different data points at a given radial position

j labels different radial positions

t_{ij} is the mean time of the ij^{th} data point

$1/\sqrt{ph_{ij}}$ is the corresponding pulse-height average

$\sigma_{ij} = RMS/\sqrt{N}$ of the associated timing data

The result of the above fitting technique is shown in figure 3.8. The χ^2 was 1.1 per degree of freedom. The results of this analysis shows that there is a maximum of $1.2\,ns$ time difference between the light collection in the center of the tray and at the edge of the tray ($50\,cm$).

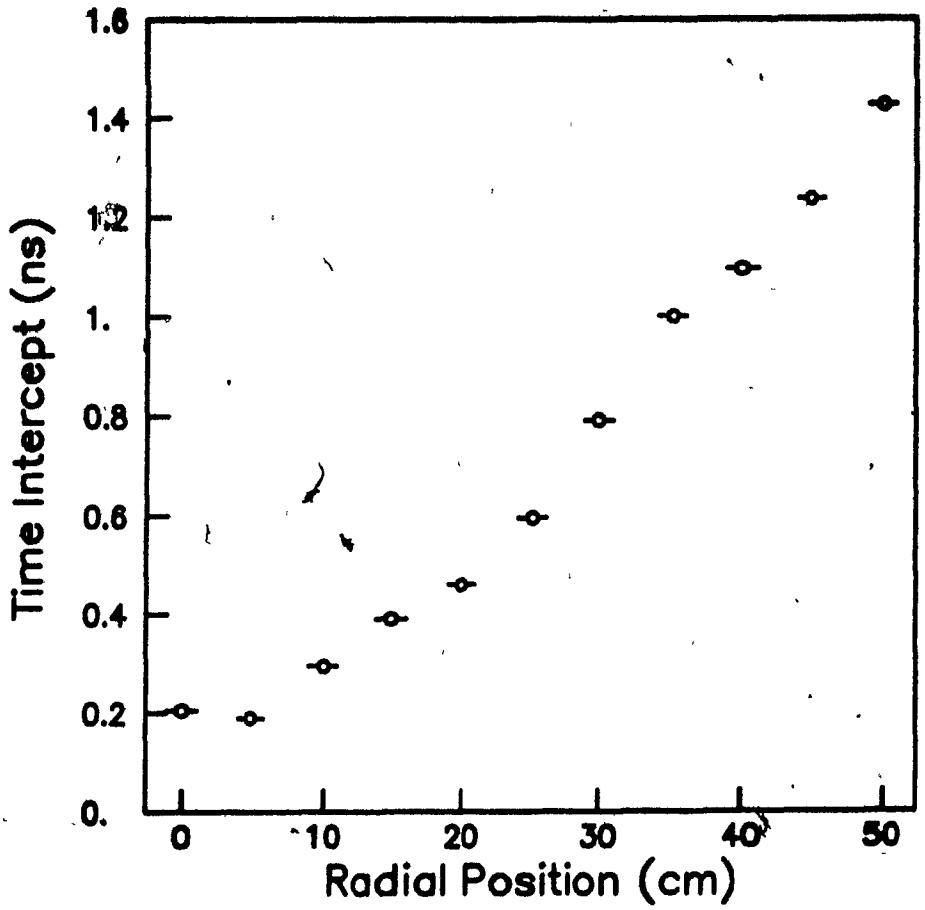

FIG 3.8: This figure shows the relative times at which a signal is recorded by the TDC as a function of the radial position, where 0 corresponds to the centre of the detector.

If one considers only the direct light (i.e. no reflections) the path length from the center of the tray to the PMT is $56.5\,cm$, and from the edge of the tray to the PMT is $78.8\,cm$. This gives the time differences of two photons travelling at the speed of light as $0.75\,ns$. Since the $1.2\,ns$ measured time difference (Δt) is a function of the path taken by the photons, and direct photons have a $\Delta t = 0.75\,ns$, it indicates that the amount of direct light is not sufficient to get the PMT above the discriminator threshold.

Monte Carlo Simulation of the Light Cone

To understand the properties of our light collection cone, a Monte Carlo program was written to simulate the photon trajectories as they pass from the scintillator to the PMT. A detailed description of the program is given in Appendix A. The pulse shaped sent by the PMT was modeled simply by generating a Gaussian shaped pulse (rise time = $6.5\,ns$) for every photon that struck the PMT, and then adding this to the previous pulse. The photons were generated from specific points along the bottom of the tray and the resulting time histograms and pulse-shapes were recorded as a function of the radial position.

A histogram of the time spectrum for $0\,cm$ and $50\,cm$ is shown in figure 3.9. By comparing the two figures it can be seen that the number of photons arriving within $50\,ns$ is significantly larger for those originating at the center of the tray than for those originating at the edge. (The total number of photons arriving within the $150\,ns$ gate width was pre-fixed for all radial positions.) The most surprising feature

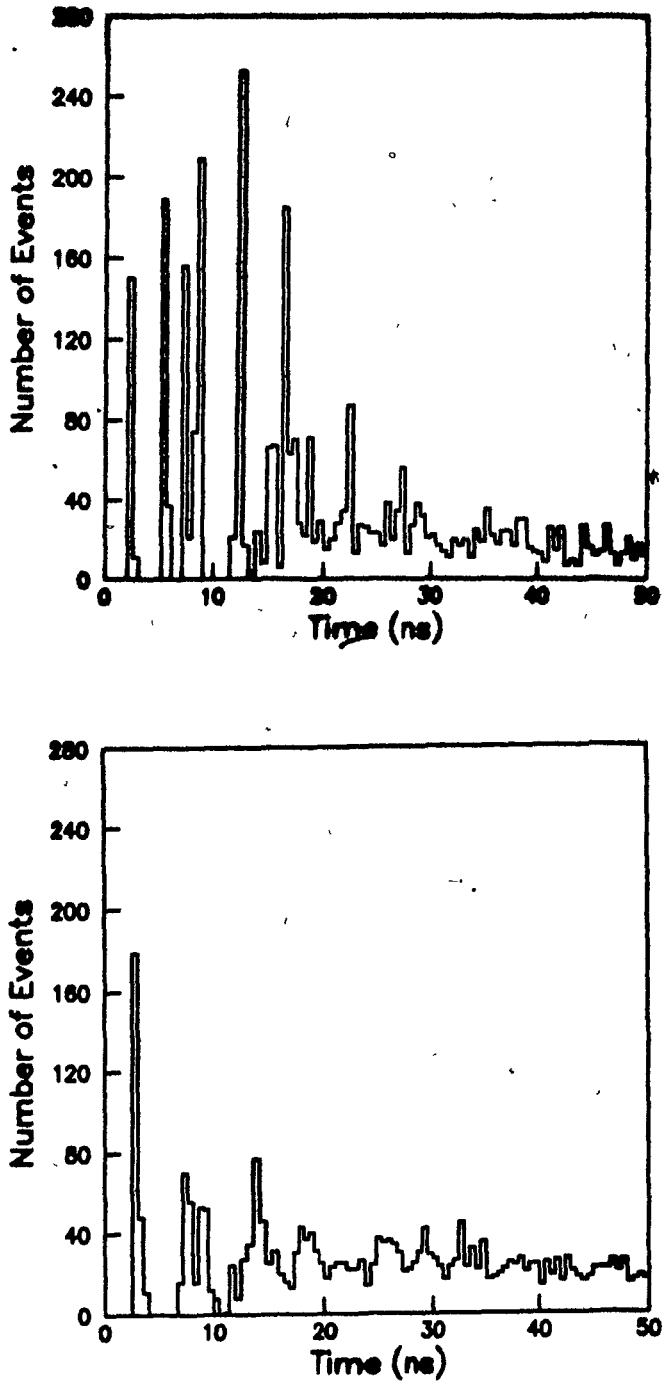

FIG 3.9: A histogram of the time it takes for a photon (with a random initial direction) to reach the PMT in the LEDA detector. This is a Monte Carlo simulation for (a) radial position = 0 , and (b) radial position = 50cm.

of the time spectrum is that the time for the fast photons is quantized. For the photons originating at the center of the tray, there appear to be preferred paths which involve one or two reflections, with a larger total solid angle than that which the direct photons have. For the photons which originate at the edge of the tray, most of the photons which strike the PMT in 10 ns are direct photons, or photons which hit the edge of the nearest light cone plane, and then go directly to the PMT. For both radial positions, the number of photons which arrive in the first stages of the pulse are almost equivalent. However, for the 0 cm pulse, photons continue to arrive, causing the pulse to peak sharply, and then quickly decline. For the 50 cm pulse, after the first burst of light, photons continue to arrive at an approximately steady rate. Hence the peak is not as sharply defined.

Although the program does not profess to accurately describe the pulse shape, the simplified results are shown in figure 3.10. The pulse-height is an integrated measure of the curves shown, and both are equivalent. It can be seen that although the pulse shape is different for the 0 cm and 50 cm, the initial rise of the pulses are very similar, and so we drew the conclusion that the time slewing effects are not radially dependent.

The main purpose of this program was to determine whether or not it would predict a 1.2 ns difference of timing as one passes from the center of the detector towards the edge. The program generates 10 events for each radial position. The average time for the pulse to pass four pre-defined thresholds (shown in figure 3.10) is calculated for

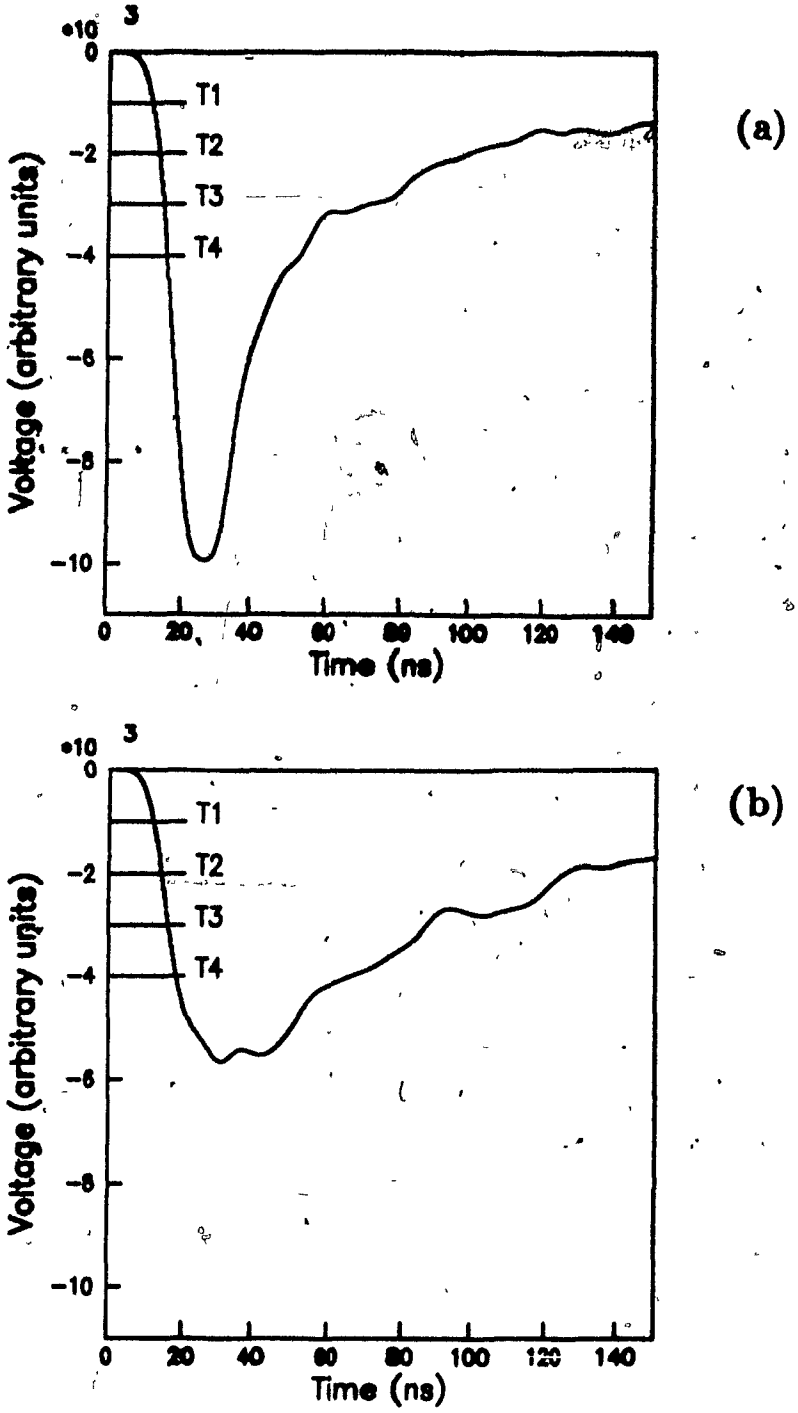

FIG 3.10: Monte Carlo generated pulse-shapes for a radial position of (a) 0cm, and (b) 50cm in the LEDA detector. T1–T4 are arbitrary discriminator thresholds, used to illustrate why there is a timing difference as a function of radial position.

each of the 11 radial positions. The results are summarized in figure 3.11. The figure illustrates that the radial timing dependence is a function of the threshold level of the discriminator, where the lower threshold gives a better resolution. Since our program does not accurately describe the pulse shape in terms of voltages and currents created by single photons, we cannot accurately predict what threshold level will give what timing resolution. However, since the threshold levels on the discriminator are set at their lowest possible levels ($30\,mV$), we have achieved the best radially dependent timing resolution possible.

Timing Dependance on the PMT

To calculate the timing resolution due only to the PMT it is necessary to first negate the effects of the radial and the pulse-height dependence. When the data is taken with the trigger counter placed directly underneath the scintillator tray, the position of the incoming cosmic ray is known to within a $10\,cm^2$ area, hence for this data there is no radial timing dependence. To correct for the pulse-height dependence, a histogram of the pulse-height correct time (t') is plotted instead of t, where t' is defined as:

$$t' = t - (a/\sqrt{ph} + b) \qquad 3.3$$

where

t' = pulse-height corrected time

t = time recorded by the TDC

a = slope of the t vs $\sqrt{ph}$ curve calculated in the previous analysis

b = time intercepts calculated in the previous analysis

ph = pulse-height recorded by the ADC

Figure 3.12 shows a histogram with the corrected time for the positions of $0\,cm$ and $50\,cm$. The results were fitted to a Gaussian with the respective means and σ's given as: $(0.72 \pm 0.04)\,ns$ and $(0.65 \pm 0.03)\,ns$. It can be seen that the random fluctuation of the times due to the PMT are not dependent on the radial position.

A response of a PMT to one photon is governed by the electron trajectories within the tube; photo-electrons created by the light pulse follow individual paths to the first dynode, depending on their point of origin. Secondary electrons also travel individual paths between the dynodes and anode depending on *their* point of origin and emission velocities, causing further time dispersions. Other factors affecting the time include:[41]

1) The number of dynodes. Fewer stages give better timing

2) The overall voltage. Higher field strengths improve timing. The time response varies approximately as $V^{-\frac{1}{2}}$

3) The photo-cathode diameter. Smaller diameters have better timing. The best timing is achieved when illuminating the central area only.

The voltage applied to each detector was chosen to maximize the efficiency of particle detecting,[13] hence we cannot adjust this to improve our timing resolutions. The number of dynodes used was also fixed to 13 to achieve the maximum amplification of the current.

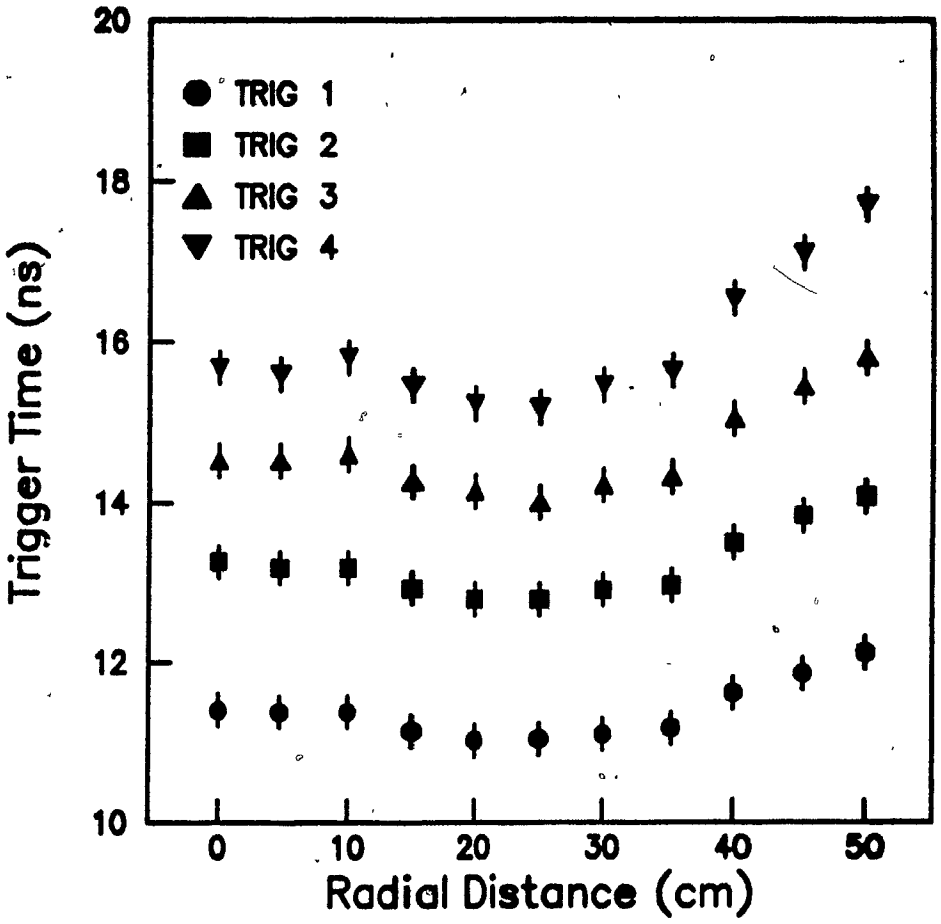

FIG 3.11: A summary of the triggering times as a function of radial position and trigger level. It can be seen that the lower the trigger level, the less time variation there is a function of position.

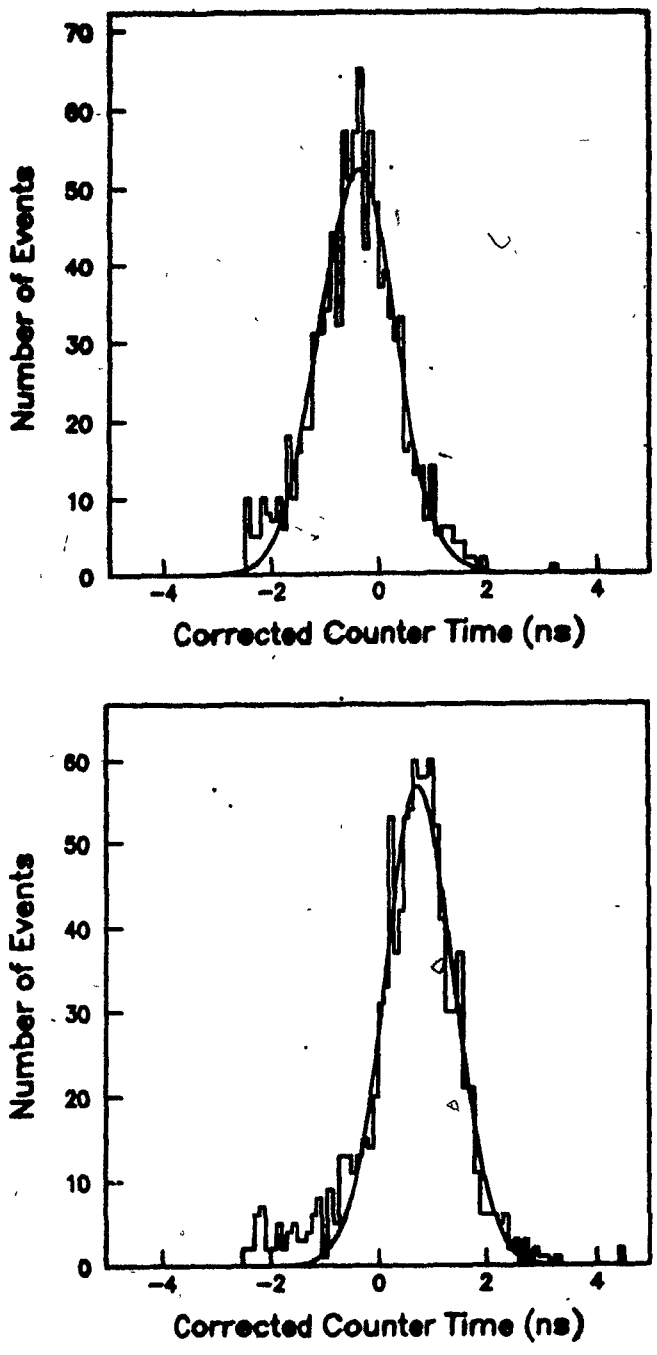

FIG 3.12: A histogram of the 'corrected' times given by equation 3.3 for a radial position of (a) .0 cm and (b) 50 cm.

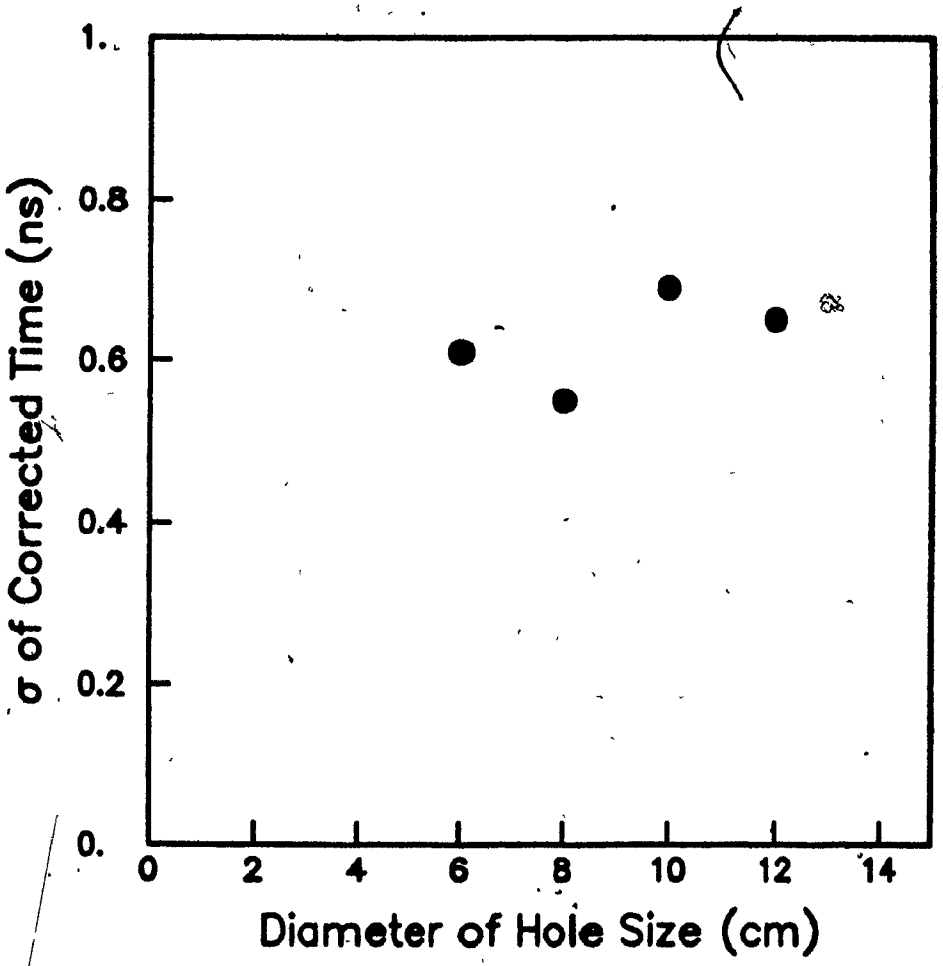

FIG 3.13: σ of the 'corrected' times of the counter as a function of the diameter of the PMT optically exposed to the scintillator.

Most hemispherical PMT's try to satisfy two conditions, a uniform collection efficiency and isochronous collection from the photocathode[42]. The latter should improve timing resolution compared with flat PMT's. To test whether timing depends on the part of the photocathode hit by a photon, we constructed four covers for the phototube made of a thick opaque plastic with each having a circular hole cut through the center. The hole sizes were 6, 8, 10, 12 cm respectively. As expected, the pulse-height was directly decreased as the hole size decreased since the pulse-height is a function of the number of detected photons. Because of this, for each hole size, the time vs pulse-height relationship had to be calculated so that the effect could be corrected for when studying only the PMT time resolutions. The histograms of the pulse-height corrected times were plotted, and the σ of the fitted Gaussians are shown as a function of hole size in figure 3.13. It can be seen that the various portions of the PMT have no noticeable effect on the timing resolutions. A similar result was quoted by Clark et al.[43]

Total Timing Resolution

The timing resolutions up until this point have been calculated only for single particles. Because the time versus pulse-height can be measured and corrected for off-line, it does not play a role in the total timing resolution. To fold in the timing resolution of the PMT and the radial dependence of the time, a Monte Carlo program was written which combines the Gaussian smearing ($\sigma = 0.7\,ns$) and the 1.2 ns change in timing as a function of the radius. We can then simulate a timing distribution

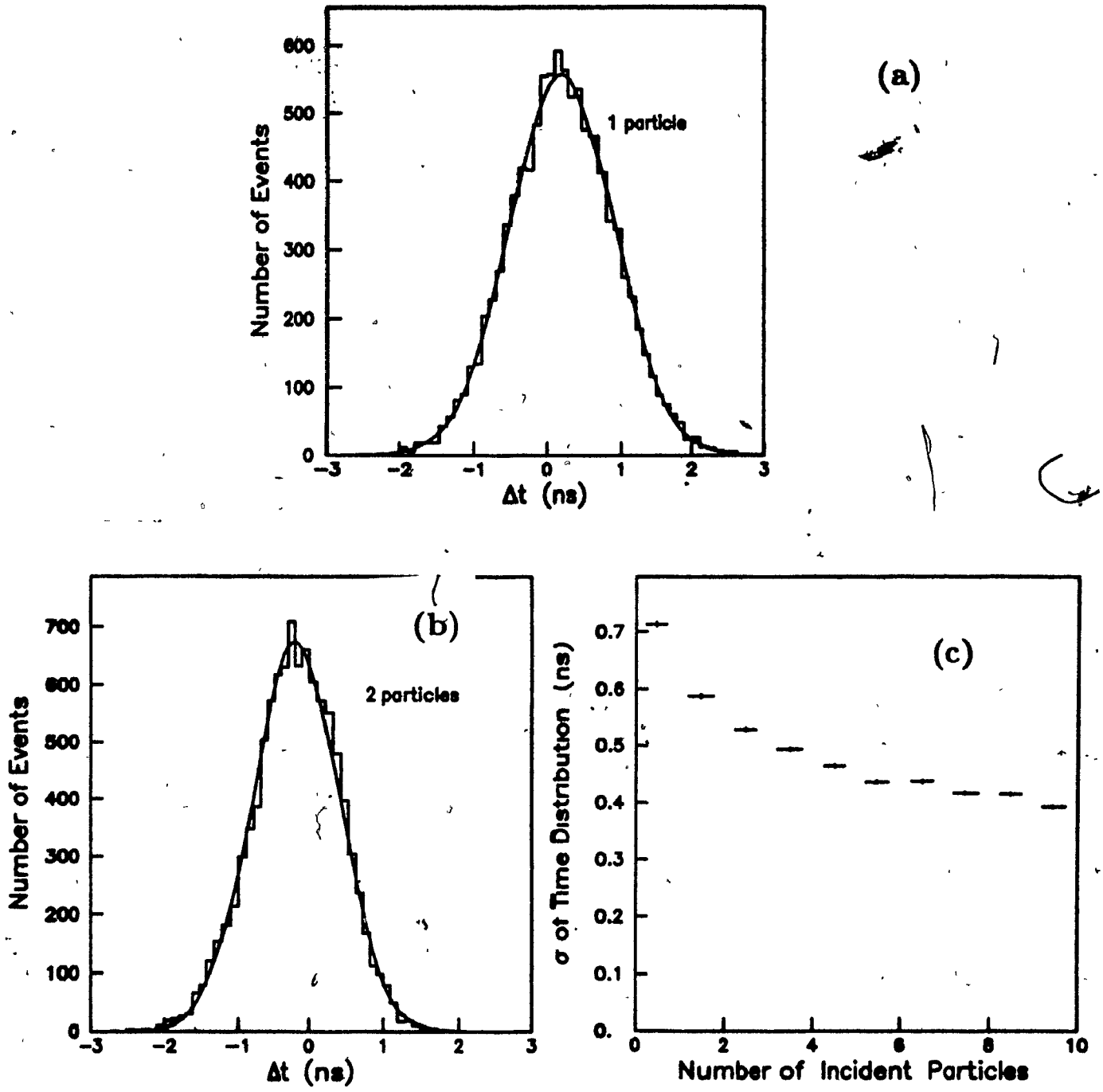

FIG 3.14: (a) Simulation of timing response of the counter of single particles assuming a uniform flux of particles across the face of the counter and using the information from figs. 3.8 and 3.12. (b) As in (a) but simulating the response to the simultaneous traversal of two particles at arbitrary and uncorrelated points. (c) Simulated timing resolution as a function of particle multiplicity in the counter.

for the counter assuming a uniform flux of particles across its face. The curve for single particles appears in figure 3.14(a) while figure 3.14(b) shows the results for events where two particles, uncorrelated spatially, traverse the counter simultaneously. With more particles the timing resolution improves as can be seen by looking at figure 3.14(c) where the σ's of 3.14(a) and 3.14(b), along with those from similar distributions with more particles traversing, are plotted versus particle number. A limiting σ of $0.5\,ns$ seems obtainable.

4.0 LEDA ARRAY

4.1 Air Shower Array

LEDA (Large Experiment to Detect Air-showers) is located near St. Anne de Bellevue on the island of Montreal. It was constructed in a corn field belonging to the Macdonald College farm. Our original plan was to make an hexagonal array comprised of 19 detectors and a grid spacing of $50\,m$. However, when the land was surveyed we discovered that due to the limitations imposed by the size of the field, the maximum grid size possible was $43\,m$. After each detector spot was marked, four $1\,m$ deep holes were dug for the support posts. After these $10 \times 10\,cm$ posts were planted correctly, the tops were sawed off to a uniform height. This was done with great care to ensure that the wooden base was level, which in turn would ensure that the liquid scintillator would be uniformly distributed in the tray. To inhibit any warping of the wooden base due to damp weather conditions, it was firmly bolted to the support posts. The cables used for the detectors were passed through a small hole in the base. Thick industrial plastic was then used to seal the bottom to prevent any of the caustic liquid scintillator from leaking on the ground in case of any leakage from the counter bottom. Next, the empty scintillator tray was placed over a sheet of aluminized mylar and four support blocks. The blocks were used to keep the center of the tray from sagging due to the weight of the scintillator liquid. When the counters are filled with the liquid scintillator they weigh approximately $50\,kg$, so it was decided that the filling process should be done in the field once the trays were in place. This would prevent the seal

from breaking due to the liquid sloshing about. The light cones were then placed over the tray, the PMT placed on top of the light cone, and finally, the whole apparatus was covered with the dark plastic. The final shielding, (the steel pyramid) was placed over the detector and firmly screwed into the wooden base.

The final form of LEDA consists of of 19 detectors arranged in a hexagonal shape as shown in figure 4.1. The detectors are not coplanar, however the maximum difference between the highest and the lowest is less than $2\,m$. The hexagonal shape was chosen because it is the closest approximation to a circle that can be achieved with a regular lattice arrangement. A circle maximizes the area, minimizes the circumference and has no corners. The total area of the array is approximately $22,000\,m^2$. Each detector is used in the density and fast timing measurements. The inner seven counters (1-7) are connected to the electronics hut (which is located at the center of the array near detector 1) via 50 metre high-voltage (RG59) cables and 50 metre fast signal (RG58) cables. The outer twelve counters (8-19) are connected to the electronics hut via 100 metre cables. Given that the speed of the signal in the cables is 2/3 the speed of light, the signals of the outer counters will be delayed by $250\,ns$ with respect to the inner seven.

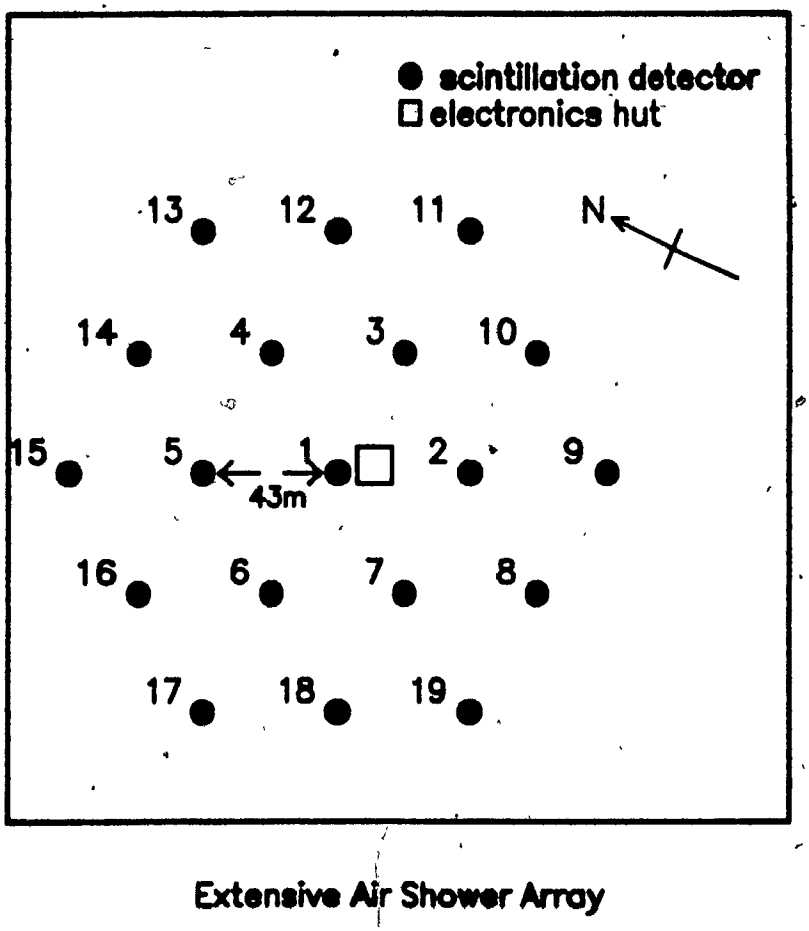

FIG 4.1: An illustration of the LEDA air shower array. The detector numbers are labelled, where the 'inner seven' counters are labelled from 1 through 7 and the 'outer twelve' counters are labelled from 8 through 19. The grid spacing is 43 m.

4.2 Electronics Configuration

The photomultipliers require high voltage which is powered by the LeCroy HV4032A 32-channel high voltage supply. The analog-to-digital converters (ADC) and the time-to-digital converters (TDC) are housed in a CAMAC crate. Also, within the CAMAC crate, the computer used to read the information from the ADC/TDC's is the LSI-11/2 computer using the RT11-FB operating system. The discriminators, gate generators and the fan-in/fan-out modules are housed in the NIM bin.

TABLE 4.1

Electronic Modules

abbreviation	description	model #
ADC	analog to digital converter	LeCroy 2249W
TDC	time to digital converter	LeCroy 2228A
DISCR	octal discriminator	LeCroy 623B
FI/FO	logic fan in / fan out	LeCroy 429A
GATE GEN	gate generator	LeCroy 222
HV	high voltage supply	LeCroy HV4032A

The electronics configuration of the experiment is shown in figure 4.2. As signals come in from the inner seven counters, they are split by 4/1 splitters. The larger signal is used for the fast timing to minimize time slewing effects described in chapter 2. The smaller signal is passed through $100\,ns$ of delay cables and then converted to digital form by the ADC. The larger signals from the inner seven counters are split equally, before entering separate discriminators, one with a threshold ($th_1 = -30\,mV$) set just above the noise level of the counter and one with a higher threshold ($th_2 = -200\,mV$).

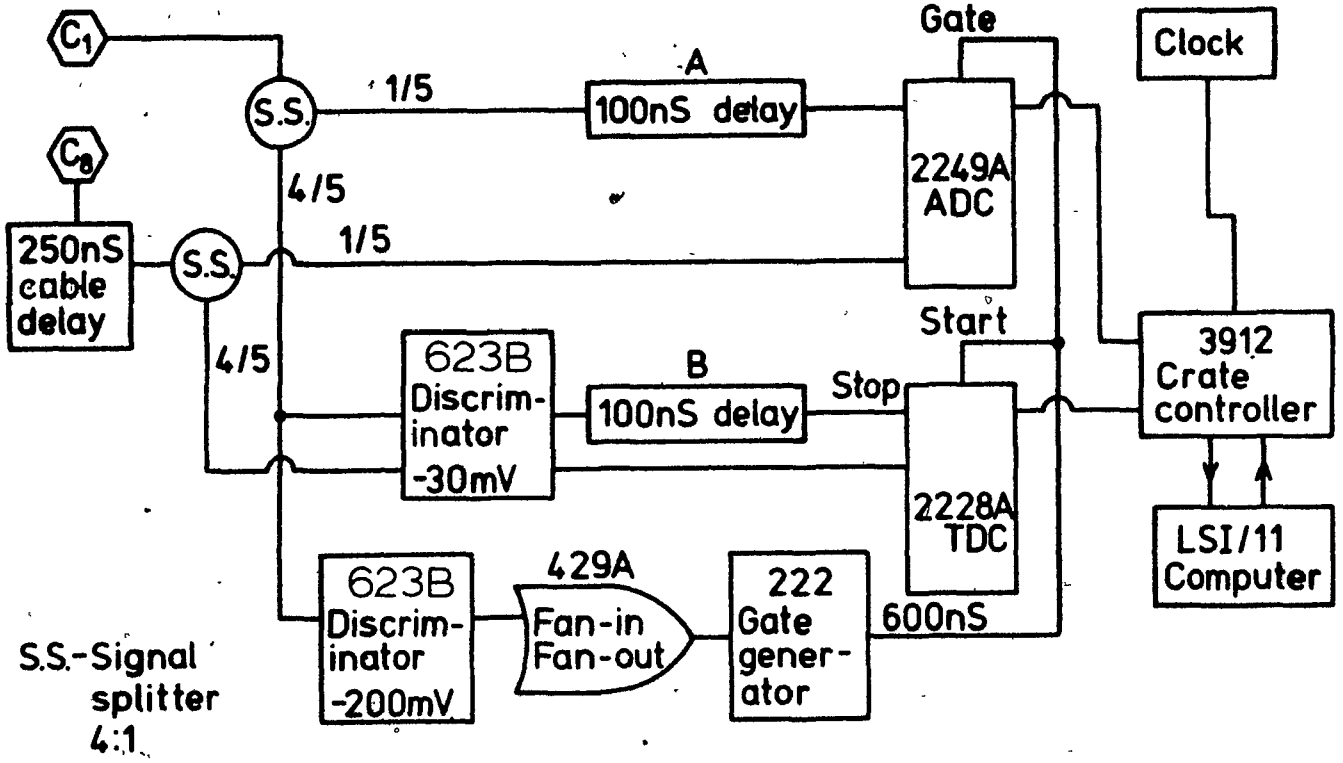

FIG 4.2: A block diagram of the electronic signal processing used in our experiment. The incoming pulses from all the detectors are split with 4/5 of the pulse going to the discriminators and 1/5 the pulse going to the ADC. The pulses from the inner seven counters (C1) are used for the start and stop of the TDC and ADC after passing through a high level (-200 mV) discriminator. The outer twelve counters (C8) have an additional delays due to the extra length their signal cables.

The first discriminator's signal is used to stop the TDC clock after being delayed by $100\,ns$. The second discriminator's signal is used for the triggering which will be explained in a later section. The signals coming from this second discriminator are combined into an OR gate, which sends a pulse to the NIM gate generator. The resultant pulse is used as the gate for the ADC, and as the start pulse for the TDC. Thus the experiment is triggered only if one of the inner seven detectors goes above the threshold of the second discriminator. The outer 12 counters are arranged similarly, but they are not used in the primary trigger, so they only use one low threshold discriminator to generate a pulse which stops the TDC. The method used in determining the amount of delays needed and the length of the gate width is described in the next section.

4.3 Delays and Gate-widths

Because of the various lengths of the signal cables, and transit times in the trigger logic, it was necessary to add delays to some of the incoming signals to ensure that all of the analog pulses are inside the generated gate, and that all of the timing stop pulses arrive after the start pulse. Also, the angle of the shower front causes the time in each detector to be offset by

$$vt = (x\cos\phi + y\sin\phi)\sin\theta \qquad 4.1$$

where

v is the velocity of the shower front, (usually taken as $30\,cm/ns$)

d is the distance separating the two respective counters

θ & ϕ are the zenith and azimuthal angles.

The amount of delay that is needed was calculated by using a Monte Carlo program, which was written to simulate our experiment. It was found that the inner seven counters had particles which 'hit' the detector up to $100\,ns$ *before* the trigger was sent (see figure 4.3a.) This occurs when the shower, coming at an angle θ, hits the first of the inner seven counters giving a signal which is above the threshold th_1 but below the triggering threshold of th_2. If the signal pulse is sent to the electronics hut without any additional delays, it will arrive before the trigger pulse, which will only be sent after the shower front strikes another one of the inner seven counters which has a signal above th_2. Suppose for example, in figure 4.4, that the particle density was such that $th_1 <$ signal $< th_2$ for counters 2, 3, & 7 and that counter 1 triggered the experiment because it was the first detector that had a signal larger than th_2. If $\theta = 30^0$ and $\phi = 0^0$, then the signal from counter 2 would arrive $(1/.30)43 \sin 30^o \cos 0^o \approx 72ns$ before the trigger. Therefore, unless the signals coming from the inner seven counters are delayed by $100\,ns$ with respect to the trigger signal, some information could be lost.

Because the outer 12 counters are connected to the electronics hut by $100\,m$ cables, as opposed to the $50\,m$ cables that the inner 7 counters use, they have an intrinsic delay of $250\,ns$ and hence, they do not need extra delay cables. Using the above example, the signal from counter 9 would arrive $250-(1/.30)86 \sin 30^o \approx 100\,ns$

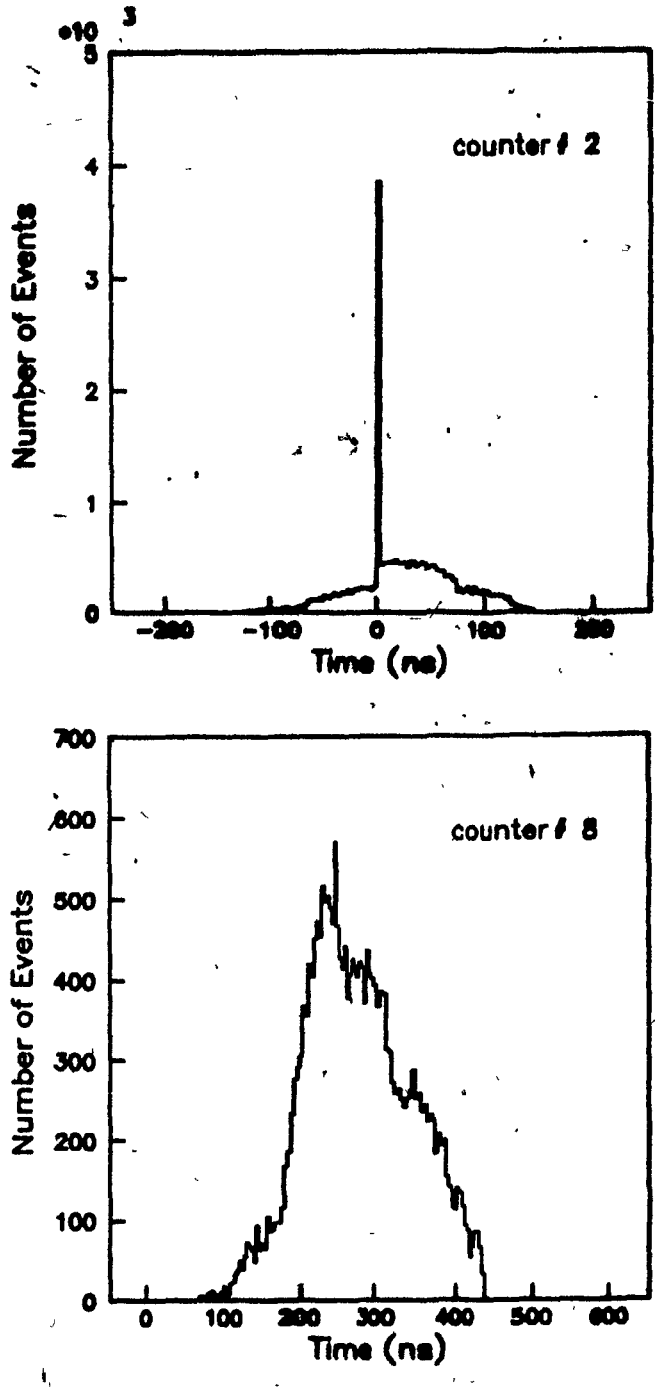

FIG 4.3: A Monte Carlo simulation of the arrival times of the shower front for counters 2 & 8. The sharp peak in (a) is a result of the pulse from counter 2 being used to start the clock.

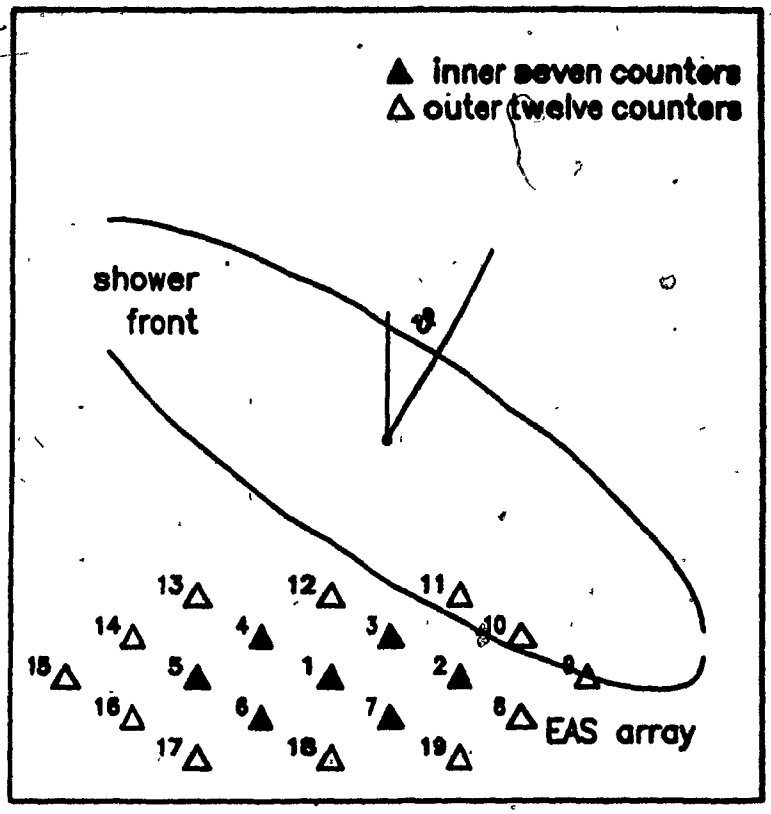

FIG 4.4: An illustration of the shower front approaching the air shower array with angle θ.

after the trigger.

The Monte Carlo also showed that due to extra flight time for the shower front as well as the extra $50\,m$ of signal cable used for the outer 12 counters, the signals arriving from these counters come as late as $500\,ns$ after t_0 (see figure 4.3b). Once the pulse is sent, the ADC requires a gate width of at least $150\,ns$ to obtain an accurate integration of the pulse. This then gives us a gate width with a minimum of $650\,ns$.

After the first few preliminary runs, the timing information was histogrammed for each detector. Because of the triggering methods, the inner 7 detectors and the outer 12 detectors have patterns which are unique to their own groups. The timing histograms for counter 2 and counter 8 are shown in figure 4.5. The sharp peak in the histogram for counter 2 corresponds to those events which were triggered by counter 2. The location of this peak is a measure of the delay cables used for the inner seven counters within the electronics hut. It can be seen from these plots that the delays and the gate width of $650\,ns$ are sufficient.

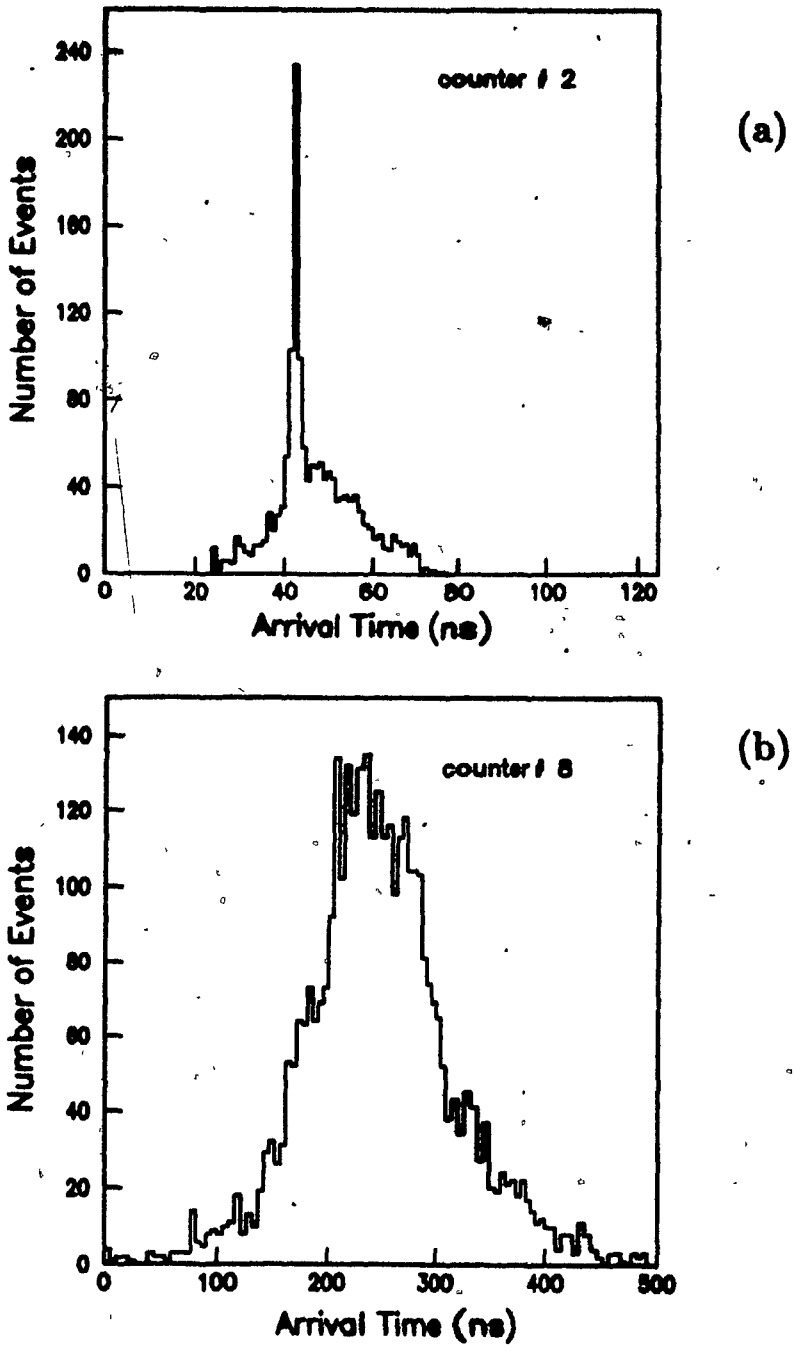

FIG 4.5: A histogram of the arrival times of the shower front for (a) counter 2, and (b) counter 8.

4.4 Trigger Conditions

The ADC gates and the TDC starts are generated only when one of the inner seven counters goes above the threshold limit determined by the second discriminator shown in figure 4.2. Triggering on one of the inner 7 counters increases the likelihood of the shower core being within the perimeter of the array. It is essentially impossible to fit the shape and size of the shower if only the edge of the shower is detected and it circumvents the more complicated timing and delay problems involved if the outer counters are involved in the trigger.

Depending on the number of counters required to constitute a 'real' shower, the computer will accept only a small portion of the measured events and write them to disk. Unless the trigger threshold is set high enough, this will incur a significant amount of computer 'dead time' due to the time required by the computer to reject those events which do not constitute a 'shower', plus the time necessary to reset the CAMAC modules. To minimize the amount of dead time, it was necessary to find a trigger rate which was compatible with the computer's capabilities to reject those events which did not satisfy the criterion of a shower. The trigger rate of the experiment is controlled directly by the threshold levels in the discriminator. Thus as the trigger rate was adjusted through the discriminator, the trigger rate, read by a scalar, was compared with the number of events which the computer had analysed. The result of this is shown in figure 4.6. The trigger rate was chosen to be approximately 10 events/second, which corresponds to a discriminator level of $500\,mV$. To

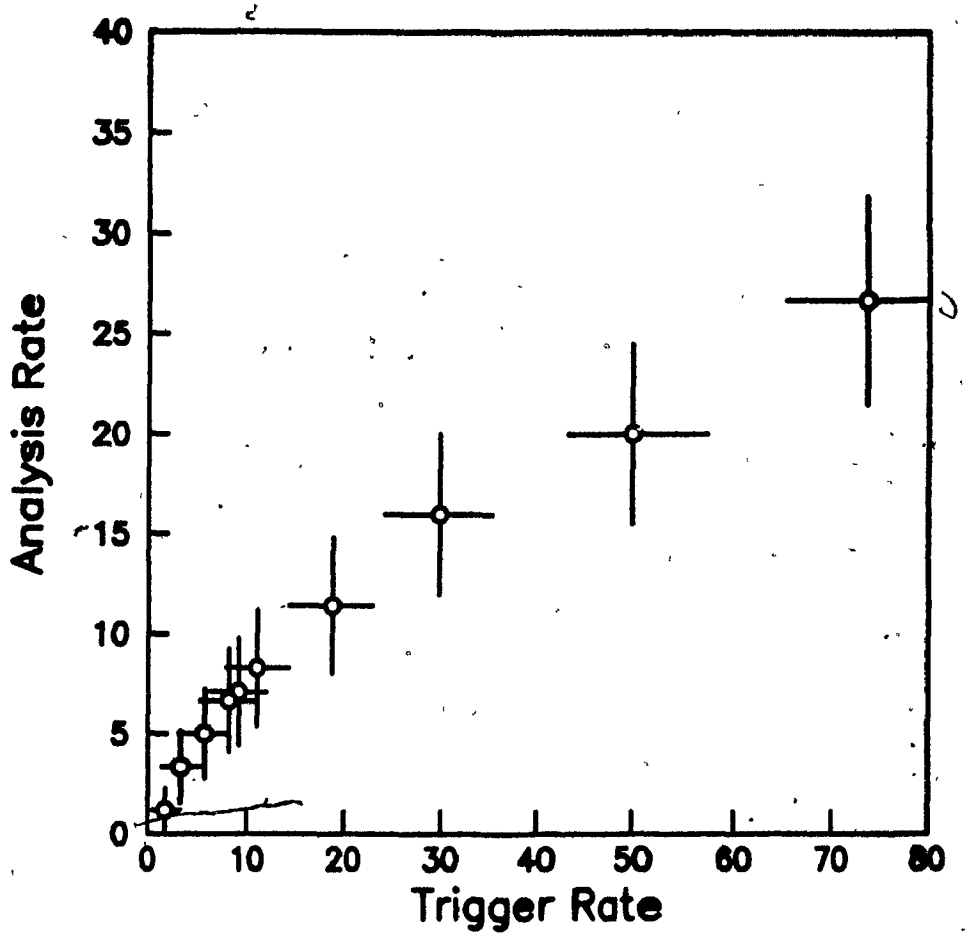

FIG 4.6: A plot of the computers ability to analyze incoming data versus the number of triggers given per second.

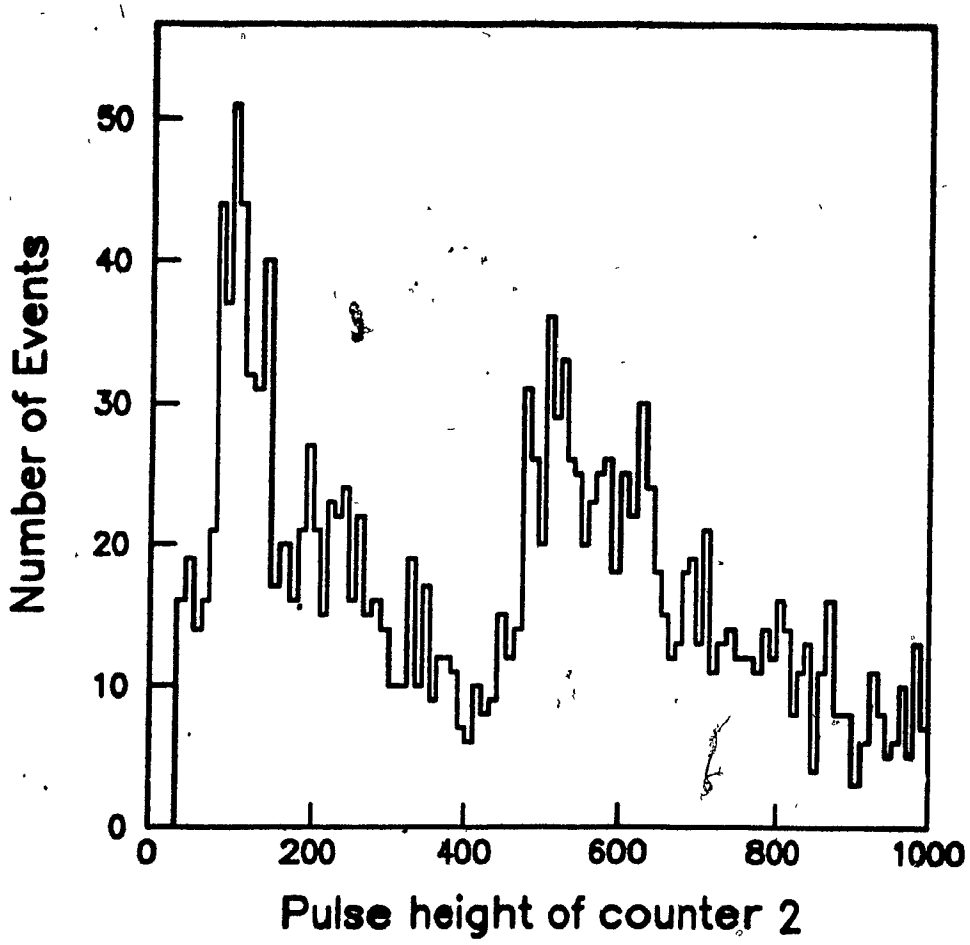

FIG 4.7: A histogram of the pulse-heights for counter 2 was plotted, using only those events which had times which fell within the peak, shown in figure 4.6.

illustrate what this means in terms of particle densities, a histogram (figure 4.7) of the pulse-heights of counter 2 was constructed by only plotting those pulse heights which had a corresponding time which fell within the peak shown in figure 4.5. It can be easily seen that the triggering level is approximately 550 adc channels, which corresponds roughly to 4 particles. Figure 4.8 is a logarithmic histogram of the time between each successive shower recorded on the disk. The linear nature of this plot suggests that the 'dead time' of the computer does not affect the rates at which we record the data.

4.5 Data Acquisition

Data Storage

If an event is accepted, the information is stored onto a floppy disk on the LSI-11/2 computer in the following manner. The first four bytes of data give the number of seconds past midnight of the current day. A code, consisting of 3 bytes, is then written. The $0 \rightarrow 18$ bits are used as a flag such that if counter x were hit, the $x - 1$ bit will be set to 1. Bits $19 \rightarrow 23$ is the number of counters hit, written in binary form. This code will then provide an automatic check, since the number of '1' bits between $0 \rightarrow 18$ should be equivalent to the binary number stored in the bits $19 \rightarrow 25$. For each counter hit, the ADC/TDC values read from the CAMAC crate is converted into another 3 byte 'word'. The first 12 bits of this word is the ADC value, and the second twelve bits is the TDC value. It should be noted that the CAMAC control only returns 12 bits for each ADC or TDC value. An example of the data storage

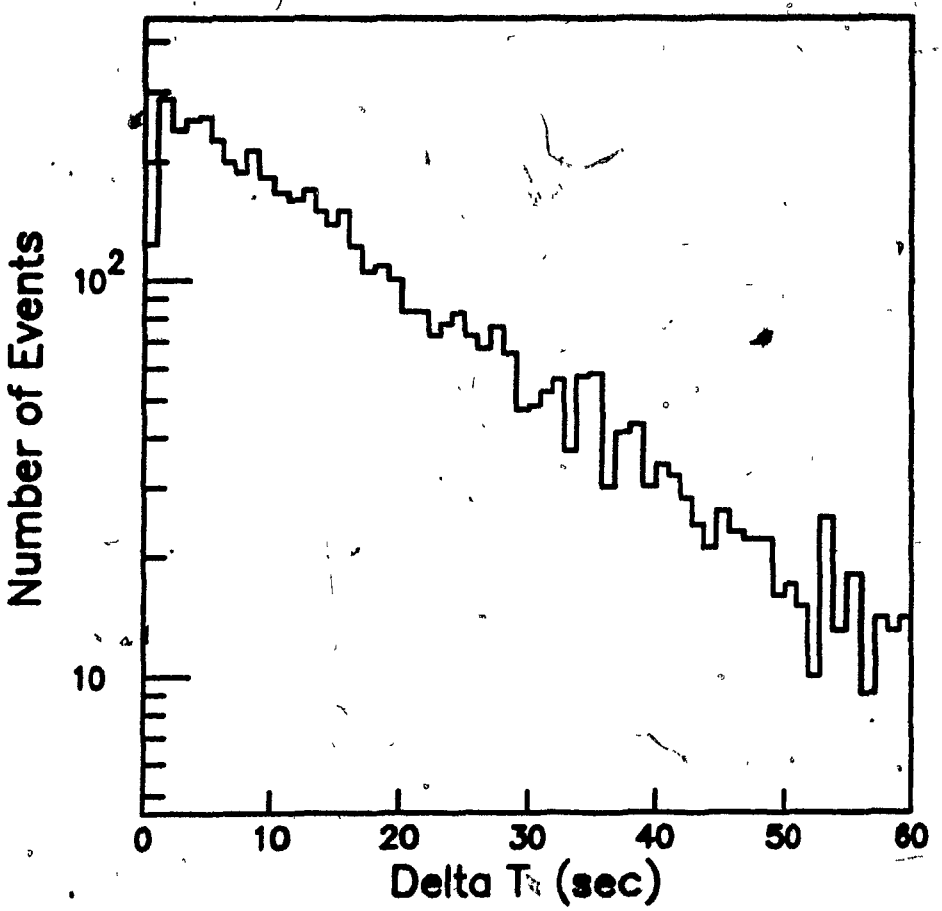

FIG 4.8: A logarithmic histogram of the time between successive recorded showers.

technique is shown in table 4.2. This technique was used to minimize the amount of disk space needed to store the shower data.

TABLE 4.2
Data Storage on the LSI

computer form				what it means
byte	← 4 →	← 3 →	← 2 →	← 1 →	
	0011 0011	0000 0000	0100 1000	0101 1001	The shower was recorded at 55603 seconds after midnight
byte	← 7 →	← 6 →	← 5 →		
	00100 001	0001 0000	0100 0010		4 counters were hit.
	# hit	which counters were hit			They were 2,7,13,17
byte	← 10 →	← 9 →	← 8 →		
	0010 0011	0001 0100	0000 1000		Counter 2 had an adc of 1032
	TDC		ADC		and a tdc value of 561.
byte	← 13 →	← 12 →	← 11 →		
	0001 1001	0100 0000	0111 0110		counter 7 had an adc of 118
	TDC		ADC		and a tdc of 404
byte	← 16 →	← 15 →	← 14 →		
	0101 0001	0001 0000	1100 1001		counter 13 had an adc of 201
	TDC		ADC		and and a tdc of 1297
byte	← 19 →	← 18 →	← 17 →		
	0100 0111	1110 0101	0100 1111		counter 17 had an adc of 1359
	TDC		ADC		and a tdc of 1151

Data Transfer

The disk is partitioned into 10 files which takes about 40 hours to fill with the normal trigger conditions (rate $\approx$ 5 showers/min). Before the disk is full however, we establish a telephone link between the McGill High Energy Physics group's VAX 785 and the LSI and begin reading filled files onto the VAX and writing them to its

disk. After each file on the LSI's floppy disk has been read, it is flagged, allowing it to be overwritten by the LSI when more space is needed. The transfer program runs in background mode and does not contribute to the dead time of the experiment. This program is typically run once a day and the transfer of data takes approximately one hour. Thus the LSI cycles continuously through the 10 files available to it, using the floppy disk as a temporary storage device. The transfer of data to the VAX is asynchronous but nevertheless requires operator intervention on a daily basis.

The information cannot be passed through the phone lines in byte form, so it must be converted into ASCII character form, which only has 6 bits as opposed to 8 bits.† To do this, each group of 3 bytes of the original data is converted into 4 characters in the following manner. The low 6 bits of every byte are rebuffered and converted into characters by adding a value of 20 *hex.* The last 2 bits of each byte are then grouped together in an extra byte to form the 4^{th} character. So, in the above example, the final form of the data file which is stored at McGill is shown in table 4.3.

Once a week, the pedestals for all the ADCs are recorded, as well as the histogram of the self-triggered pulse-heights for each detector. Since the self-triggered histogram is predominately single particle pulses, the mean is commonly referred to as the single particle line (SPL). This histograms is used to determine the noise level for that detector and to determine the SPL value needed for the energy calculations. These

† **ASCII character codes range in value from 32 → 126 (20 → 7E *hex*). Since the 8^{th} bit is not used and the 6^{th} bit is always 1, there are only 6 usable bits left.**

TABLE 4.3
Data Storage on the VAX

Original form of data (HEX)	Final form of data (HEX)
59 48 00 33 42 10	39 28 20 25 53 22 30 24
21 08 14 23 76 40	41 28 34 20 43 56 20 25
19 C9 10 51 4F E5	39 29 30 2C 31 2F 45 37
47	27 21

numbers are recorded, and the data taken within the next week is blocked together to form one 'run', with the date used as the run name.

Frequency

The number of showers recorded for every 2-day period since October 1987 is shown in figure 4.9. During the months of July, August, and September the files created on the LSI were sent through Datapac 3101^{TM}, which a Canada-wide switching network operated by Telecom Canada, to the VAX. This system was automated, but unfortunately it was unreliable, and tended to inhibit continuous data collection. There was no data collected in October because, at that time, the field needed to be harvested, which required us to disconnect our experiment.† During this time we developed the current data transfer program.

During the Christmas break we added additional cuts to the program. Instead of having one parameter describing the noise level of all the detectors, 19 parameters

† In the future we will bury the cables so that this will no longer be a problem.

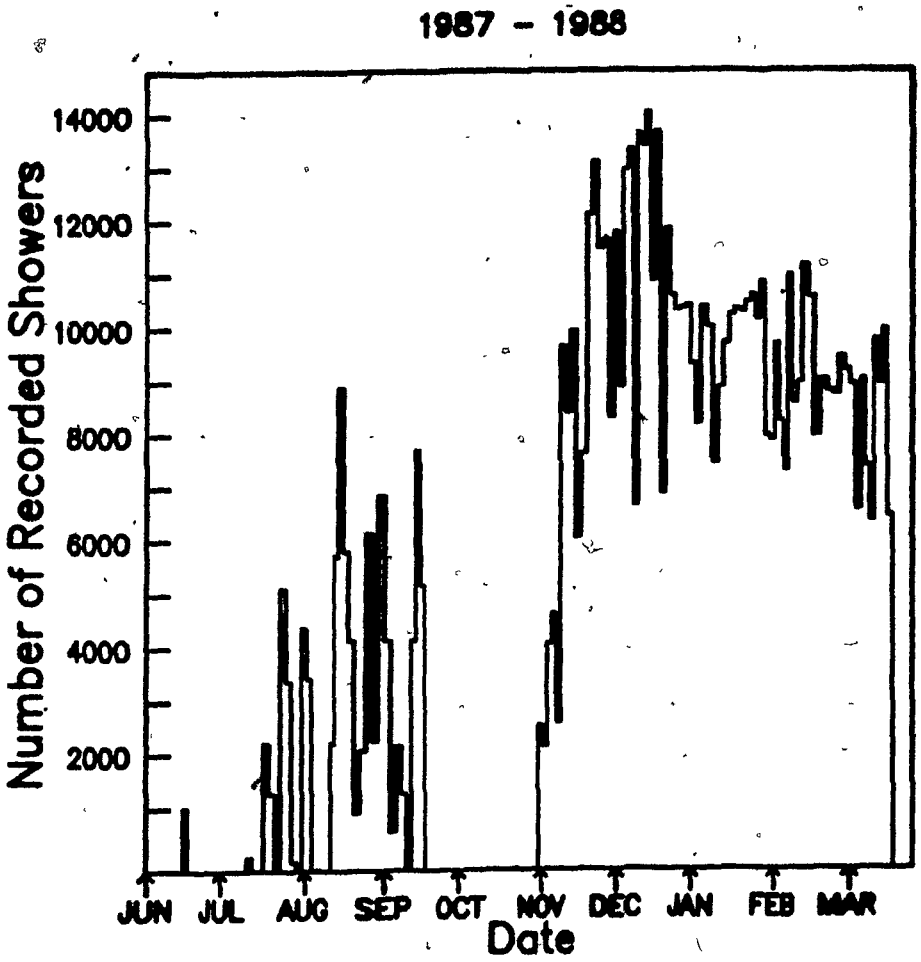

FIG 4.9: A histogram of the total number of showers recorded on disk for each two-day period.

were included to eliminate erroneous data from detectors with high pedestals. These cuts reduced the total number of showers recorded on disk, but not the actual amount of useful events.

4.6 Timing Calibrations

Calibration of the TDC

TABLE 4.4
Gain and Time Offsets for the TDC channels

counter#	cc/ns (±.02)
1	4.17
2	4.18
3	4.12
4	4.22
5	4.23
6	4.19
7	4.20
8	4.16
9	4.26
10	4.30
11	4.23
12	4.21
13	4.31
14	4.31
15	4.25
16	4.28
17	4.09
18	4.13
19	4.04

The conversion from clock-counts to nanoseconds was pre-set to $4\,cc/ns$ on the TDC module. To determine the accuracy of this, we used the pulse from one counter

to start the clock and then the same pulse, delayed by a succession of calibrated cables, was used to stop the clock. The individual measurements were then fitted to a straight line to determine the conversion factor for each channel. These conversion factors are listed in table 4.4 for each counter. They range from $4.09\,cc/ns$ to $4.23\,cc/ns$.

Pulse-Height Corrections

It was shown in chapter 2 that the 'absolute' time is dependent upon the pulse height of the incoming signal because of the time slewing effect. Time slewing is a function of the electronic devices as well as a function of the photo-tube. In the lab it was shown that the time slewing effects between photo-tubes was not consistent, and in the field, the electronic configuration is different than that in the lab. Instead of 1/2 the incoming pulse being used to stop the TDC clock, now 4/5 of the pulse from the outer 12 counters and 2/5 of the pulse from the inner 7 counters is used to stop the clock. Therefore it was necessary to measure the time-slewing effects for each counter under field conditions.

To measure the time slewing, a trigger counter, comprised of two plastic scintillators separated by lead with two fast photomultipliers, was placed underneath of the detector to provide the 'absolute' time. Because we wanted to know the time delay of each counter with respect to the same arbitrary point and not just the relationship between one counter and the triggering device, it was necessary to maintain the cable arrangement for the trigger counters between one experiment and the next. This would then give us the extra advantage of incorporating any extra delay time times

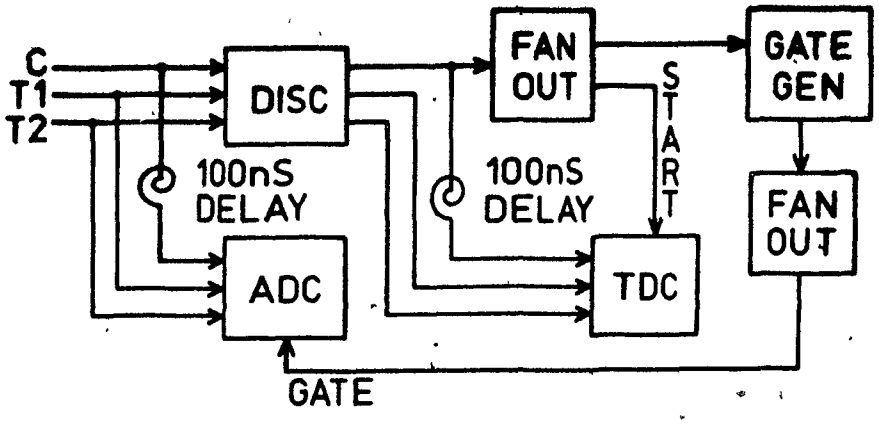

(a)

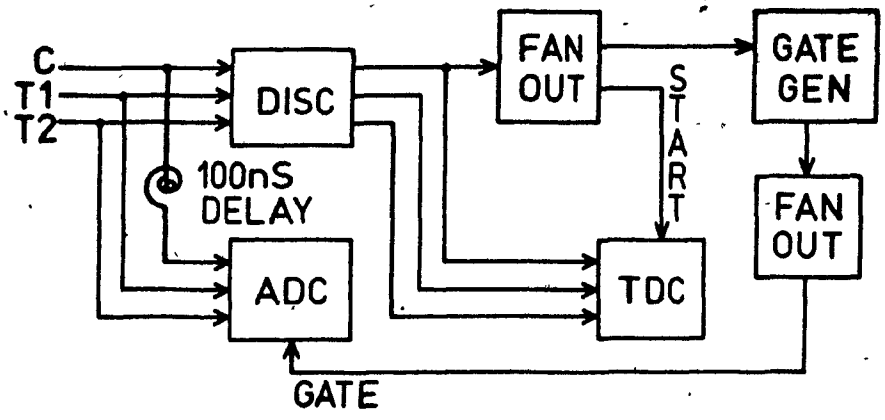

(b)

FIG 4.10: A block diagram of the electronics used in the time-slewing measurement for (a) the inner seven counters (1-7) and (b) the outer twelve counters (8-19). The signal from counters (1-7) were split with 2/5 going to the discriminator and 1/5 of the pulse going to the ADC. The other 2/5 were not used. The signal from counters (8-19) were split with 4/5 going to the discriminator and 1/5 going to the ADC. In both cases, the counter started the clock.

due to inaccurate measurements of the cable length into the calculation. The signal from the counter was used to trigger the electronics, and after the trigger was sent, the computer program only accepted an event if the trigger ADC levels were above noise levels and if the TDC times were not overflowed. The electronic configuration is shown in figure 4.10. The clock is started when the pulse from the counter passes over the threshold of the discriminator. The measurement of the electronic delays, and the delay cables for the inner seen counter, is measured by the stop pulse of the counter. Because the time-slewing effects occur within the discriminator the start and stop pulses are effected equally, therefore the measurement of the electronic delay is pulse-height independent. The trigger counter generates two stop pulses, and because the trigger counter uses fast PMTs, we assume that stop pulses are pulse-height independent.

Because the start time of the clock is pulse-height dependent, but the trigger stop pulses are not, the time slewing is actually recorded by the time variation of the trigger counter. This is demonstrated in figure 4.11. The data was analyzed using only the timing information from the scintillator located at the top of the trigger counter, with the electronic delays added as a constant. The interpretation of the equation

$$t = a/\sqrt{ph} + b \qquad 4.2$$

is that a is a measure of the time-slewing effect, and the intercept b is a direct measure of the of the timing delays due to cable lengths and electronic delays.

There was a total of five tests done for each counter with each test having a

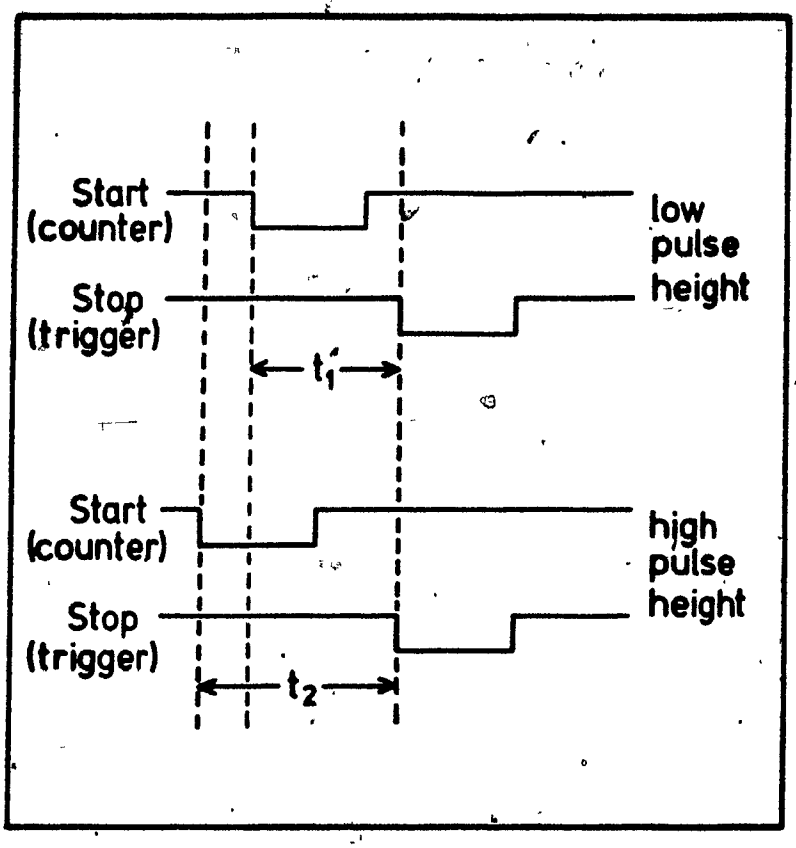

FIG 4.11: A timing diagram of the start and stop pulse of the TDC, with different pulse-heights coming from the counter. The start pulse is pulse-height dependent which causes the measured time t_1 and t_2 to be variable, even though the time of the stop pulse is constant.

TABLE 4.5
A summary of the parameters a,b for each detector, where a,b were defined by the equation $t = a/\sqrt{ph} + b$

counter#	a (ns)	b (ns)
1	112.1 ± 8.4	10.0
2	108.0 ± 8.1	6.8
3	123.2 ± 10.8	6.3
4	93.2 ± 7.4	5.6
5	106.7 ± 6.1	13.8
6	121.3 ± 10.4	14.6
7	106.4 ± 11.8	4.7
8	227.6 ± 5.7	145.0
9	141.1 ± 6.7	154.3
10	120.2 ± 5.4	154.7
11	137.6 ± 5.9	153.3
12	136.7 ± 11.9	152.8
13	182.8 ± 12.4	145.0
14	143.7 ± 8.7	152.7
15	145.3 ± 5.6	148.6
16	102.8 ± 10.0	151.1
17	116.2 ± 4.4	154.1
18	137.3 ± 3.6	151.3
19	106.6 ± 1.4	163.2

different voltage. The voltages were set at $V_0 - 20$, $V_0 - 10$, V_0, $V_0 + 10$, $V_0 + 20$, where V_0 is the operating voltage for that particular detector. The general shape of the curve was continuous between the varying voltages, so we combined the data of all of the voltages and fit the data to equation 4.2, which is shown in figure 4.12 for counter 19. A summary of the time-slewing corrective terms (a in equation 4.2) is shown in figure 4.13.

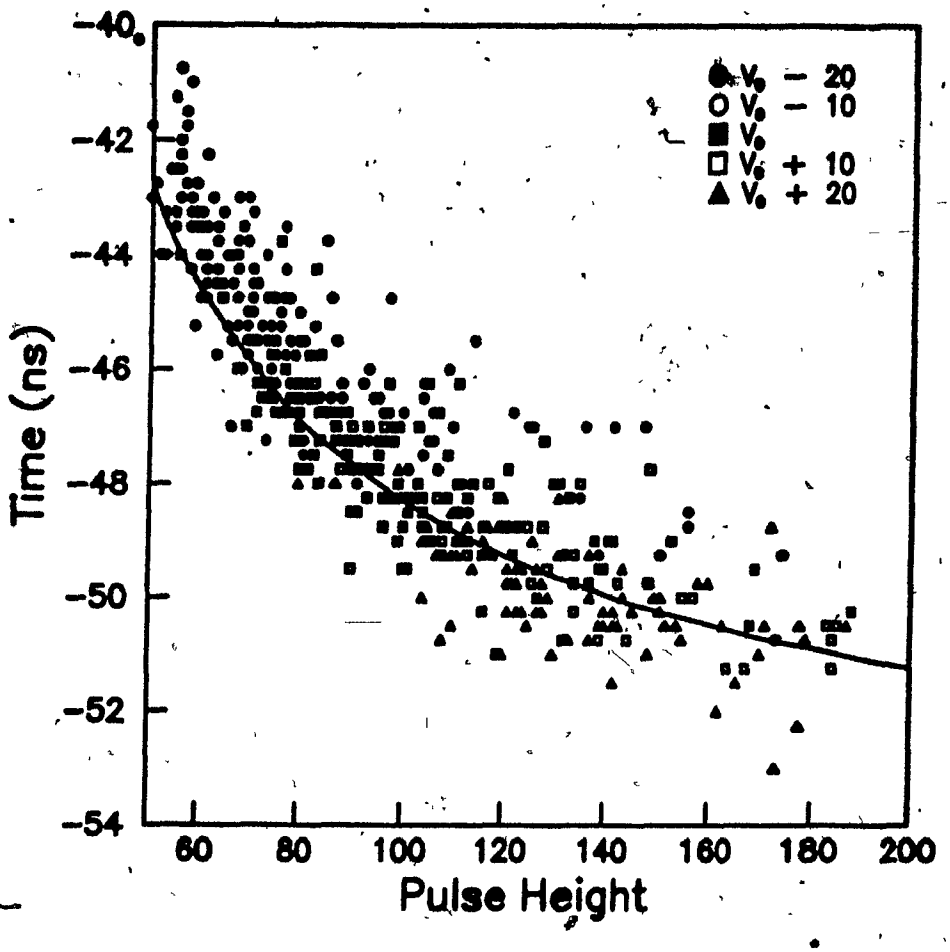

FIG 4.12: The results of the time-slewing data is shown here with the calculated function superimposed on the graph.

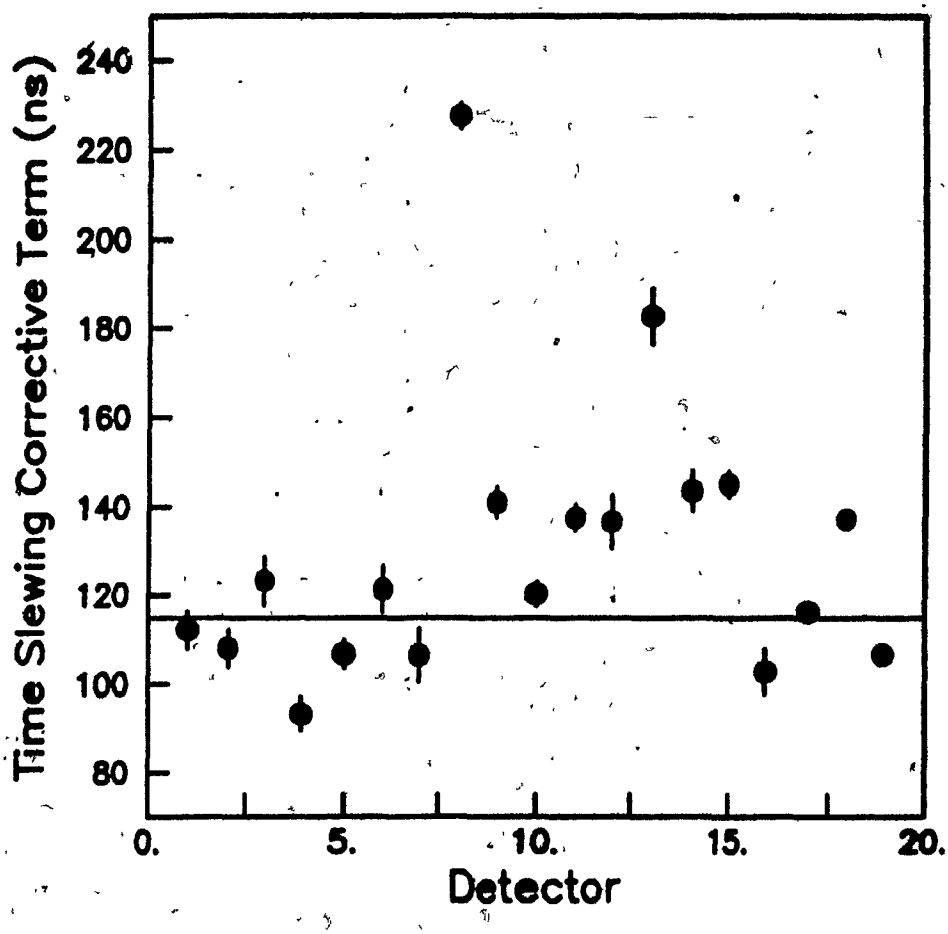

FIG 4.13: The time slewing-corrective term is shown for each detector, where the line is the mean value.

Timing Resolution

The parameters listed in table 4.5 were used to find a 'corrected' time for each one of the counters ie:

$$t = t_i - a/\sqrt{ph_i} + b \qquad 4.3$$

and the results were histogrammed. A Gaussian distribution was fitted for each histogram and the resultant σ was $1.3 ns$. The results for counter 2 are shown in figure 4.14. The σ was found to be larger than the results listed in chapter 2. This inconsistency can be understood in terms of the actual experimental configuration. In the laboratory, the trigger counter was placed directly underneath the counter with a maximum vertical separation distance of $3 cm$. However, when the timing tests were done in the field, the vertical distance between the trigger and the counter varied depending on how much snow was under the detector at the time of the test. The lower the trigger detector is from the bottom of the counter, the larger the area is on the counter bottom where a particle may pass and still be detected by the trigger. This is illustrated in figure 4.15. In figure 4.15a, the distance between the points of impact on the bottom of the counter is minimal as compared to part b. It was shown in chapter 3 (see figure 3.8) that the absolute time is a function of radial position at which the particle crosses the counter bottom. Hence it can be seen that if the trigger was not immediately adjacent to the counter bottom, the acceptance area is larger and the radial position of the incoming particle will have a larger effect on time distribution.

Using this data, the expected uncertainty in each detector is less than 1 ns. This value is small when compared to the uncertainty in time due to the finite thickness of the shower front.

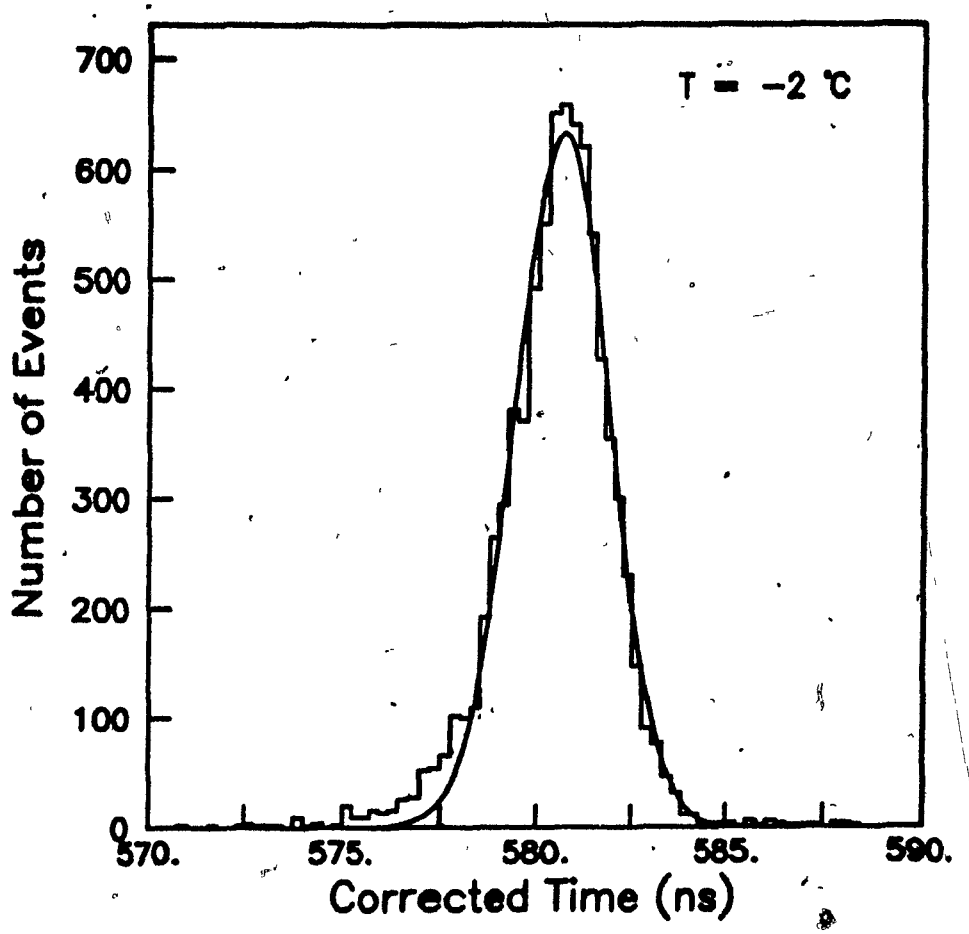

FIG 4.14: A histogram of the 'corrected' time (equation 4.3) for counter 2.

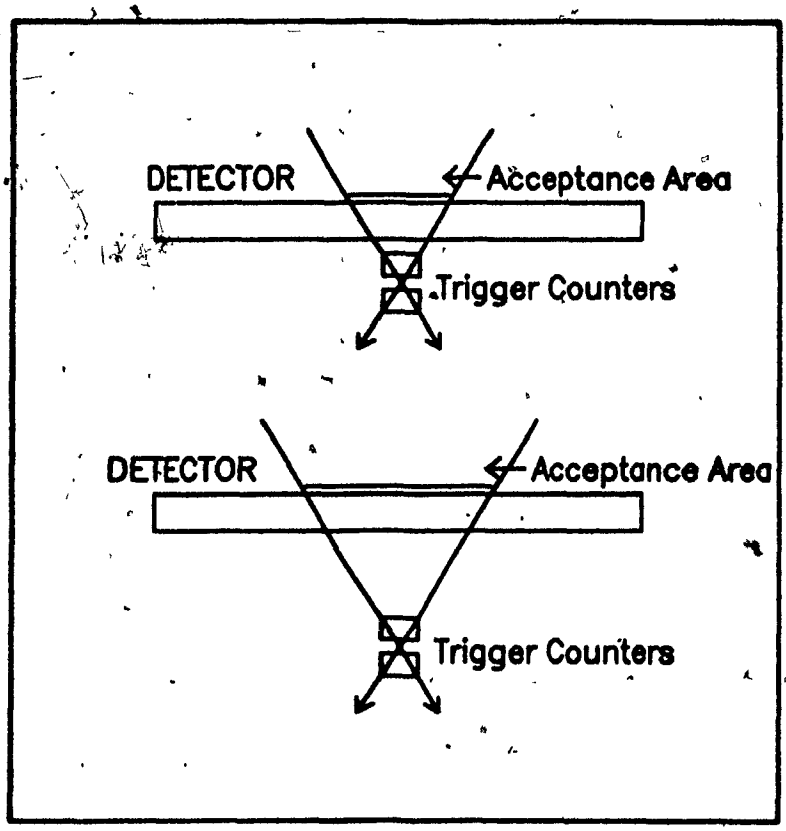

FIG 4.15: An illustration of how the position of the trigger counters will effect the acceptance area of the incoming particles.

5.0 DATA ANALYSIS

5.1 Fitting the Shower Front

As the extensive air shower develops through the atmosphere, the electrons form a thin ($1 \sim 2\,m$) spherical shape with a radius of curvature of $\sim 2600\,m$. Because of the large radius of curvature, and our small effective viewing area, the shower front can be approximated as a disk.

For each counter that participated in the event there is a direct measurement t_i. Because of the finite measurement precision, the measured times deviate from the 'true' values by a random amount which is measured by the standard deviation σ_i. The most useful method of fitting such data, if the function describing their relationship is linear, is the least squares method

$$\chi^2 = \sum_{i=1}^{n} \frac{r_i^2}{\sigma_i^2} = \min \qquad 5.1$$

where

r_i = residual, defined as the difference between the expected value and the value actually measured

n = number of data points

σ_i^2 = uncorrelated variance of each measurement t_i

In our case, we are fitting the time t_i to a plane by the following expression:

$$ct_i = a_1 x_i + a_2 y_i + a_3 \qquad 5.2$$

where

c = velocity of light $(.2998\, m/ns)$

x_i, y_i = position of the i^{th} detector in meters

t_i = measured time in ns given by the i^{th} detector.

Therefore, the χ^2 for this set of data is:

$$\chi^2 = \sum_{i=1}^{n} \frac{(a_1 x_i + a_2 y_i + a_3 - c t_i)^2}{\sigma_i^2} \qquad 5.3$$

To find the minimum of χ^2, the differentials $\partial\chi^2/\partial a_1$, $\partial\chi^2/\partial a_2$, and $\partial\chi^2/\partial a_3$ are set equal to zero. The resulting three equations can be summarized into a matrix form:

$$\mathbf{FA} = \mathbf{T} \qquad 5.4$$

where

$$\mathbf{F} = \begin{pmatrix} \sum x_i^2/\sigma_i^2 & \sum x_i y_i/\sigma_i^2 & \sum x_i/\sigma_i^2 \\ \sum x_i y_i/\sigma_i^2 & \sum y_i^2/\sigma_i^2 & \sum y_i/\sigma_i^2 \\ \sum x_i/\sigma_i^2 & \sum y_i/\sigma_i^2 & \sum 1/\sigma_i^2 \end{pmatrix}$$

and

$$\mathbf{A} = \begin{pmatrix} a_1 \\ a_2 \\ a_3 \end{pmatrix}, \qquad \mathbf{T} = c \begin{pmatrix} \sum t_i x_i/\sigma_i^2 \\ \sum t_i y_i/\sigma_i^2 \\ \sum t_i/\sigma_i^2 \end{pmatrix}$$

Solving for the matrix $\mathbf{A} = \mathbf{F}^{-1}\mathbf{T}$ then gives the 'best fit' parameters a_1, a_2, a_3.

To determine the error in **A** we use the matrix notation of the standard formula of error propagation. If we have a linear equation

$$\mathbf{Y} = \mathbf{BX}$$

and the covariance matrix of **X** [**V**(X)] is a diagonal matrix with the diagonal elements equal to σ_i^2, then the covariance matrix of **Y** is

$$\mathbf{V(Y)} = \mathbf{B}\ \mathbf{V(X)}\ \mathbf{B}^T$$

Using this method, and the proper choice of matrices, it can be shown[44] that the covariant matrix of A given in equation 5.4 is

$$\mathbf{V(A)} = \mathbf{F^{-1}} \qquad 5.5$$

Conversion to θ, ϕ

Once we have determined the best fit for the parameters a_1, a_2, a_3, we must convert this to the angles θ and ϕ. Figure 5.1a shows the plane front and one detector placed at XC,YC. Using simple trigonometric properties it can be seen that

$$\dot{z} = \frac{d}{\tan\theta}$$

$$d = (yc - xc\tan\phi)\cos\phi$$

where the value of d is found from figure 5.1b. However, it is not the angle of the plane which we wish to find, but the angle of the vector normal to the plane, ie: $\theta \rightarrow 90-\theta$, and $\phi \rightarrow \phi - 90$. Also, the time measured by the detectors do not come from vertical going particles, but from particles travelling perpendicular to the shower front, hence

$$ct = z\cos\theta$$

which gives, as our final formula

$$ct_i = -(x_i\cos\phi + y_i\sin\phi)\sin\theta \qquad 5.6$$

comparing this with equation 5.2, we then have

$$a_1 = -\cos\phi\sin\theta,$$

$$a_2 = -\sin\phi\sin\theta$$

or conversely

$$\sin\theta = \sqrt{a_1^2 + a_2^2},$$
$$\phi = \tan^{-1}\left(\frac{a_2}{a_1}\right) \qquad 5.7$$

The uncertainty in the angles can be found by using the covariance matrix and the general formula for the propagation of errors. If Δ is the variance (or covariance) of a set of parameters $a_1, a_2, \ldots, n$ and if y is a function of these parameters, then

$$\Delta y = \sum_i \sum_j \frac{\partial y}{\partial a_i}\frac{\partial y}{\partial a_j}\Delta_{ij}.$$

Taking the partial derivatives from equation 5.7 the variance of $\cos\theta$ and ϕ are given as

$$\Delta\cos\theta = (\Delta_{11}\, a_1^2 + \Delta_{22}\, a_2^2 + 2\Delta_{12}\, a_1 a_2)/\cos^2\theta$$
$$\Delta\phi = (\Delta_{22}\, a_1^2 + \Delta_{11}\, a_2^2 - 2\Delta_{12}\, a_1 a_2)/\sin^4\theta \qquad 5.8$$

The angular resolution of an array is defined as the angle between the 'real' shower direction and the calculated vector. To approximate this using the covariance matrix, we find the σ of the angle by using the equation for a solid angle

$$\delta\Omega = \delta\cos\theta\,\delta\phi$$

and the half angle α of a cone defined by $\delta\Omega$

$$\alpha^2 = \frac{\delta\Omega}{\pi}$$

to obtain

$$(\sigma_\alpha)^2 = \sqrt{\frac{\Delta\cos\theta\,\Delta\phi}{\pi}}. \qquad 5.9$$

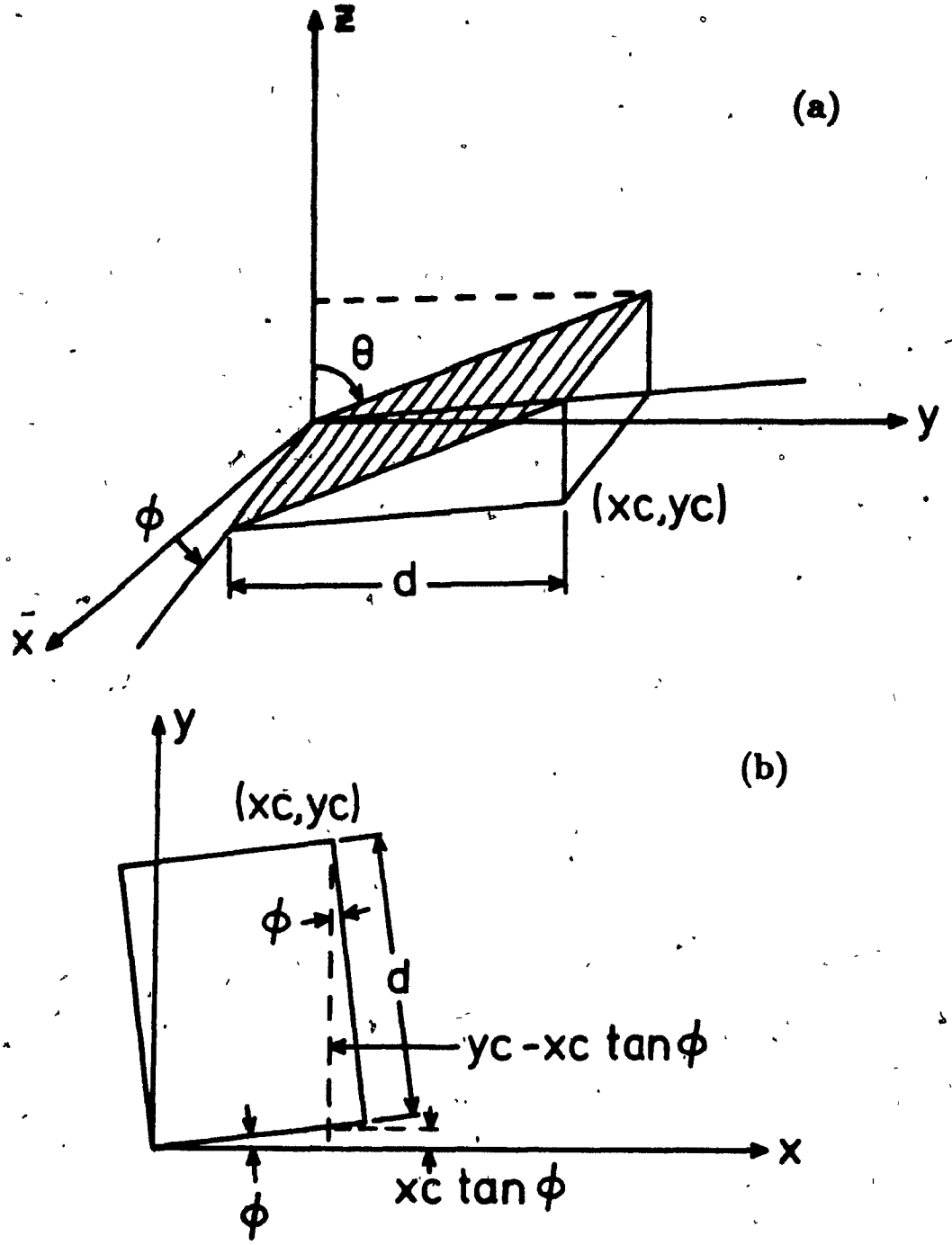

FIG 5.1: A diagram illustrating how the relative arrival times of the shower front in detectors with coordinates (xc,yc) are converted to the angles θ and ϕ which define the plane.

5.2 Monte Carlo Simulation

When the shower front is fitted using equation 5.6, it is assumed that it is infinitely thin with no curvature. However, we know[7] that each shower has a thickness between 1 and $2m$, and that the average shower curvature is $2600m$ (with a lower limit of $1300m$). If the shower front is curved, it is immediately obvious that the measured angle is dependent upon the portion of the shower front detected, which implies that the further the shower core is from the central detector, the larger the angular error.

The effect of the shower thickness on the angular resolution is a little less obvious, but nonetheless very important. At the center of the shower front, the number of particles is large, and hence the probability that there are particles at the leading edge of the shower is much larger than at the edge of the shower where the particles are less numerous. Since the detectors only measure the time of the first particle which arrives, a large shower with no curvature may still give the appearance of a curved front, and then we have a similar problem as described above.

Description of the Monte Carlo

To determine how these two phenomenon would effect the angular resolution, a Monte Carlo was written to simulate curved shower fronts with finite thicknesses.

Unless otherwise stated, the following conditions were imposed on the Monte Carlo program:

(1) The thickness *th* of the shower front was modelled by a Gaussian shape where 98% of all the particles are within *th*

(2) Each counter has a timing uncertainty with a sigma of .7ns (again the shape was Gaussian)

(3) The earliest particle striking a counter was the one that was considered to have stopped the clock. The NKG function was used to simulate the lateral spread of the shower particles.

(4) All the shower cores were generated within $100\,m$ of counter 1

(5) The event was considered accepted if 1 of the inner seven counters had 4 particles or more, and if at least 5 of the counters had 1 particle or more.

(6) The angular resolution is calculated by $\mathbf{v}_1 \cdot \mathbf{v}_2 = \cos\alpha$, where $\mathbf{v}_1$ was the normal vector generated by the shower front and $\mathbf{v}_2$ was the normal vector to the calculated shower front. The angle resolution is given by that angle inside which 63% of all the events would occur.

Mean Time Offsets

It is the standard practice of researchers using extensive air shower arrays to calibrate the time offsets in each detector by centering the the individual histograms of the arrival times about a common value.[45] The theory is that given the random nature of the shower directions, each detector is as likely to be triggered early as it is to be triggered late.

It can be seen in figure 5.2a that the means of the arrival times are indeed centered around a common value when the shower front is flat, but for curved shower fronts, the mean of the arrival time varies from detector to detector as a function of

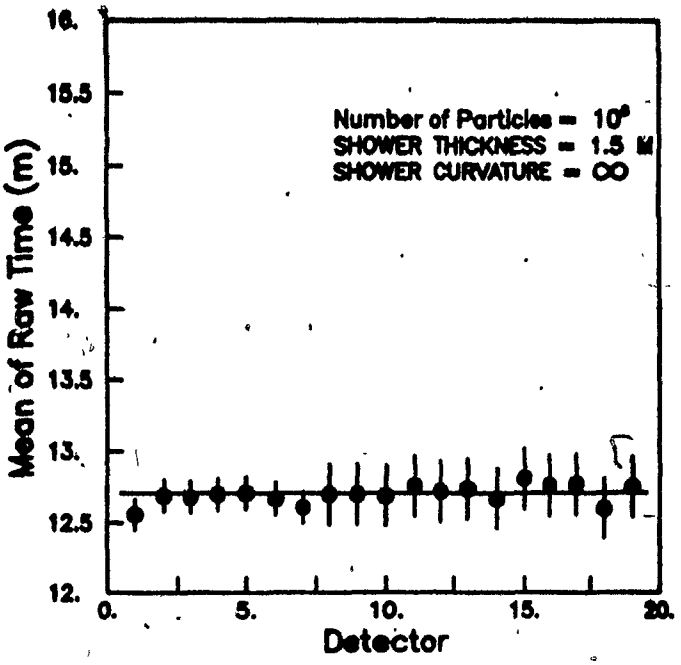

(a)

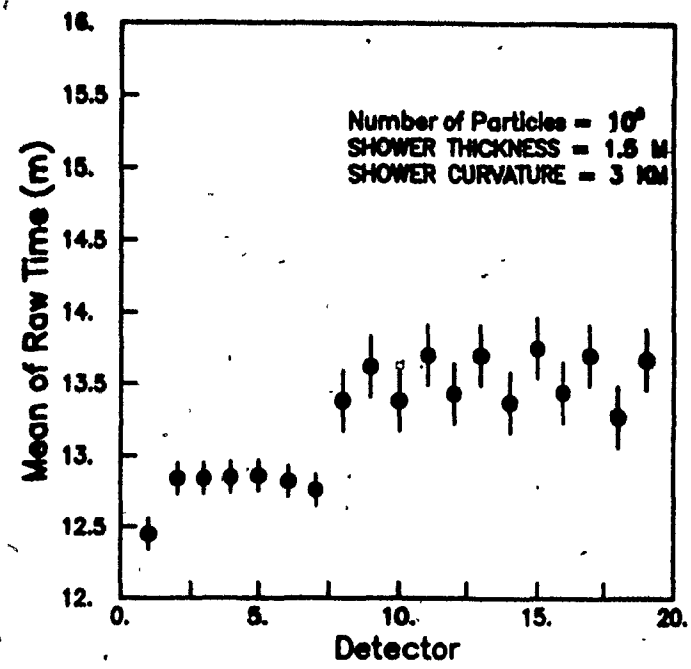

(b)

FIG 5.2: The simulated mean of the arrival time (ct) in each detector for (a) flat shower front, and (b) a curved shower front with the radius of curvature = 3000 m.

the distance from that detector to the center of the array (figure 5.2b). This unique pattern is not surprising if one considers the statistical nature of the detected showers. On average, the shower cores are located at the center of the array with $\theta = 0°$. If the curvature of the shower is R, then the measured time of each detector is offset by $d^2/2R$ where d is the distance from the center of the shower.

Angular Resolution

The angular resolution of the array is a function of the properties of the incident shower front, such as the curvature and thickness, as well as the location of the shower core with respect to the array. The results of the Monte Carlo are summarized in figure 5.3. It was mentioned before that for a curved shower front, one would expect the angular resolution to be more accurate if the shower core was located at the center of the array. Figure 5.3a shows this relationship for a shower of size 6 ($N_e = 10^6$), and three different shower curvatures. It should be noted that even for a flat shower front, the angular resolution is better near the center of the array. This is because the finite thickness of the shower front will simulate a curved structure due to the higher density of particles near the shower core.

The angular resolution as a function of shower thickness is shown in figure 5.3b. Again, the number of particles in the generated shower is 10^6. The relationship between the thickness and the angular resolution is linear regardless of the size of the shower curvature. The shower curvature seems to have the largest effect on the angular resolution, as shown in figure 5.3c. As the radius of curvature decreases, the

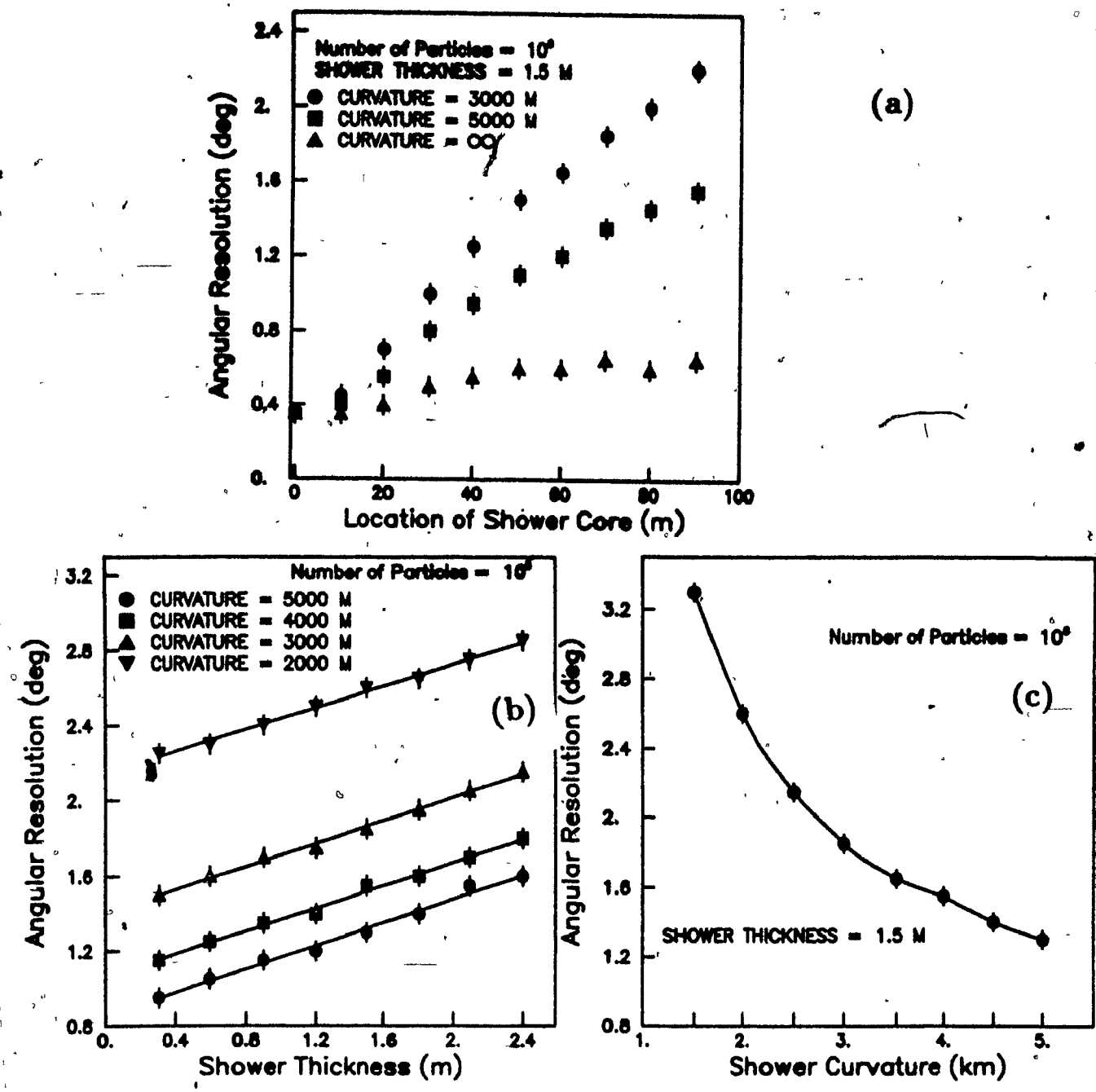

FIG 5.3: (a) Simulated angular resolution as a function of the radial distance of the shower core from the center of the array. (b) Simulated angular resolution as a function of the shower thickness, for 4 different radii of curvature, (c) Simulated angular resolution as a function of the shower curvature.

angular resolution decreases exponentially.

The summary of the relationships between angular resolution, shower curvature, shower thickness, and location of the core, do not give an estimate of the overall accuracy of our array. To do that, the above conditions were combined in the following way to simulate the operating conditions of our array. The shower sizes were randomized to obey the known flux rates, which are:

$$F(N) = 6.7N^{-2.32} \qquad 10^3 > N > 10^6$$

$$F(N) = 167N^{-2.58} \qquad 10^6 \geq N > 10^9;$$

the shower curvatures were randomized using a Gaussian function to give an average of 2600 m and a lower limit of 1300 m ($\sigma = 430\,m$); and all the generated showers had a thickness of 1.5 m. The total angular resolution calculated by the Monte Carlo was then 1.15°.

In air shower arrays, the time offsets for each detectors are not always known, so, as mentioned before, the mean of the arrival times are centered around a common value. This is equivalent to centering the residuals about zero. We simulated this in our Monte Carlo by adding a timing correction to each detector. The new angular resolution was estimated to be 1.25°.

5.3 Data Analysis

Additional Data Cuts

Because the angular resolution degrades as the distance of the shower core from the centre of the array increases, only those showers whose calculated cores† are within $75\,m$ of counter 1 are analysed. Once θ and ϕ are calculated, only the showers with $\theta < 30°$ are accepted because, at larger angles, the changes in the apparent depth of atmosphere are more significant and cause the showers to be poorly measured.

Before a shower is recorded on the disk, at least one of the inner seven counters must have an ADC channel reading of 550 or more. This value of 550 is a function of the number of particles recorded in the detector as well as a function of the amplification of the photo-tube. Because of this, there are some biases within the triggering system. For this reason, stricter acceptance conditions are required when analyzing the data. As was mentioned before, the ADC trigger acceptance corresponds to roughly to 4 particles. To un-bias the data, the software trigger conditions must be that 5 particles pass through at least 1 of the inner seven counters, and that at least 5 counters had 1 particle or more. The efficiency of shower detection of our array was modelled using Monte Carlo methods[13] and is shown in figure 5.4.

Timing Calibrations

The mean of the arrival times for all accepted showers was measured and il-

† A detailed description of this calculation is given by K. Murthy[13].

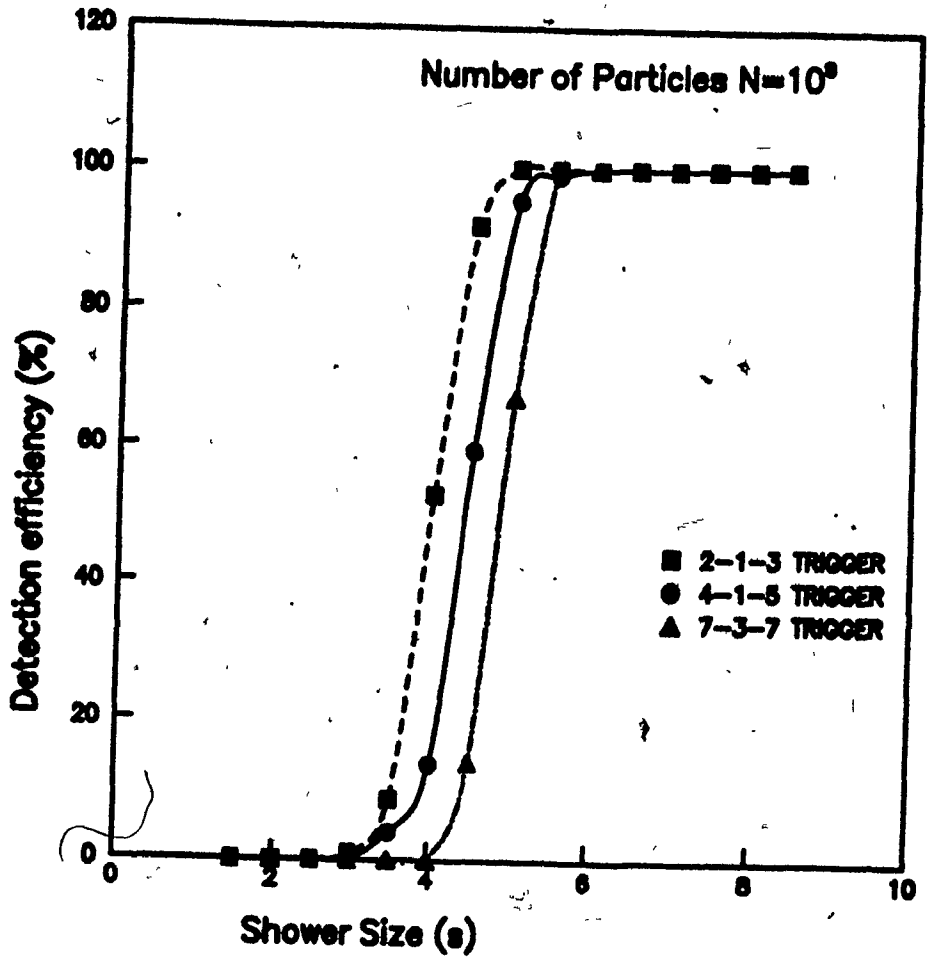

FIG 5.4: A plot of the LEDA detection efficiency for 3 separate triggering conditions. The three numbers correspond to a) the minimum number of particles required by at least one of the inner seven counters, b) the minimum number of particles required by any detector to be considered 'hit', and c) the minimum number of detectors hit before the shower is accepted.

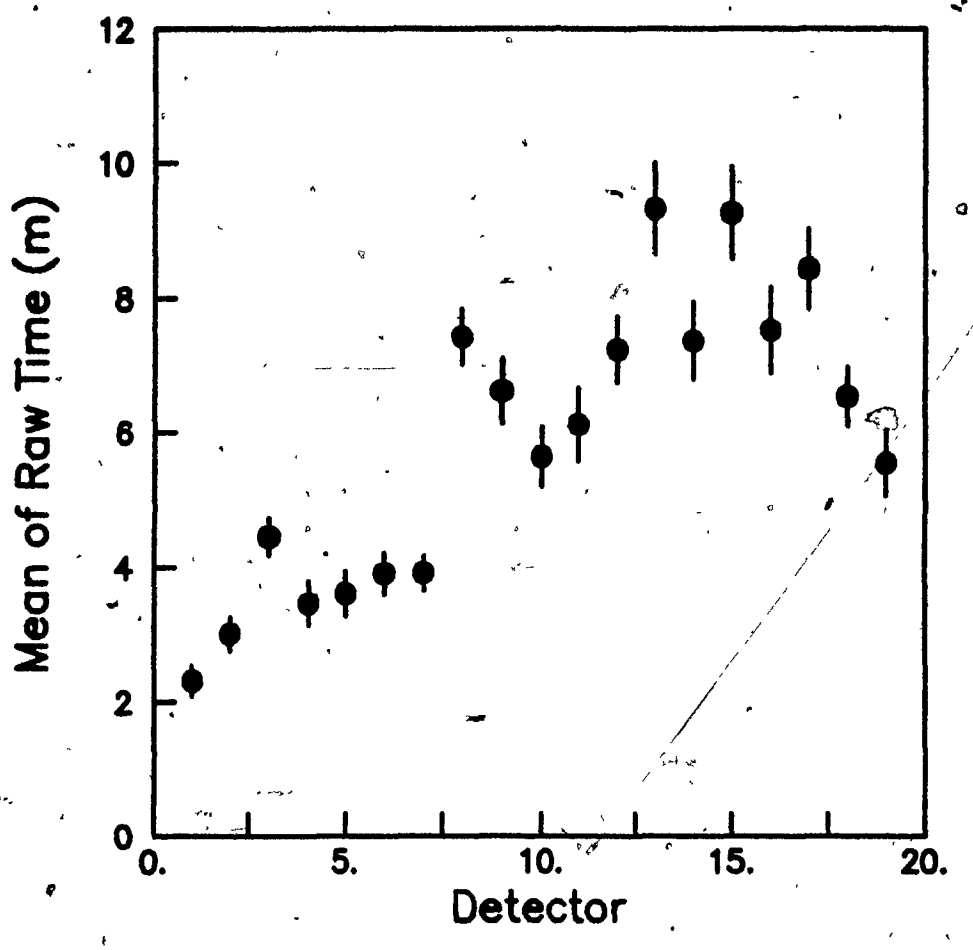

FIG 5.5: The mean of the arrival times ($\times .30\, m/ns$) is plotted for each detector.

lustrated in figure 5.5. The pattern that was originally shown in figure 5.3a is not reproduced, however the overall pattern of the real data is a mixture of timing delays due to shower curvature, as well as timing delays due to the vertical offsets of the detectors. If the detector has a coordinate of (x_i, y_i, z_i) then the time delay (ct) due to its z offset is simply $-z$. If the pattern of mean times follows the Monte Carlo, then counters 11, 10, 9, 18,and 19 have higher elevations than the rest of the array. Although there is no detailed contour map of the array location, a visual inspection of our array confirms this. To compensate for these vertical offsets, it was decided that a timing correction will be added to each detector so that the mean of the arrival times will be equal. This is justified by the Monte Carlo simulation (discussed in the previous section) which showed that doing this would decrease our angular resolution by only 0.1°.

Residuals

Before equation 5.4 can be properly utilized in obtaining the best fit for a plane, the uncertainty in the timing measurement must be known. Because of the timing uncertainties brought about by shower thicknesses and curvature, the best estimate of the timing uncertainties are obtained in the following manner. The data, once it has satisfied the above conditions, is fit using equation 5.4 with $\sigma_i = 1$. The residuals for each detector are stored in a histogram, and later fit to a Gaussian. The σ of the Gaussian is then used as the timing uncertainty for that detector. The data is then re-fit using the properly weighted time measurements.

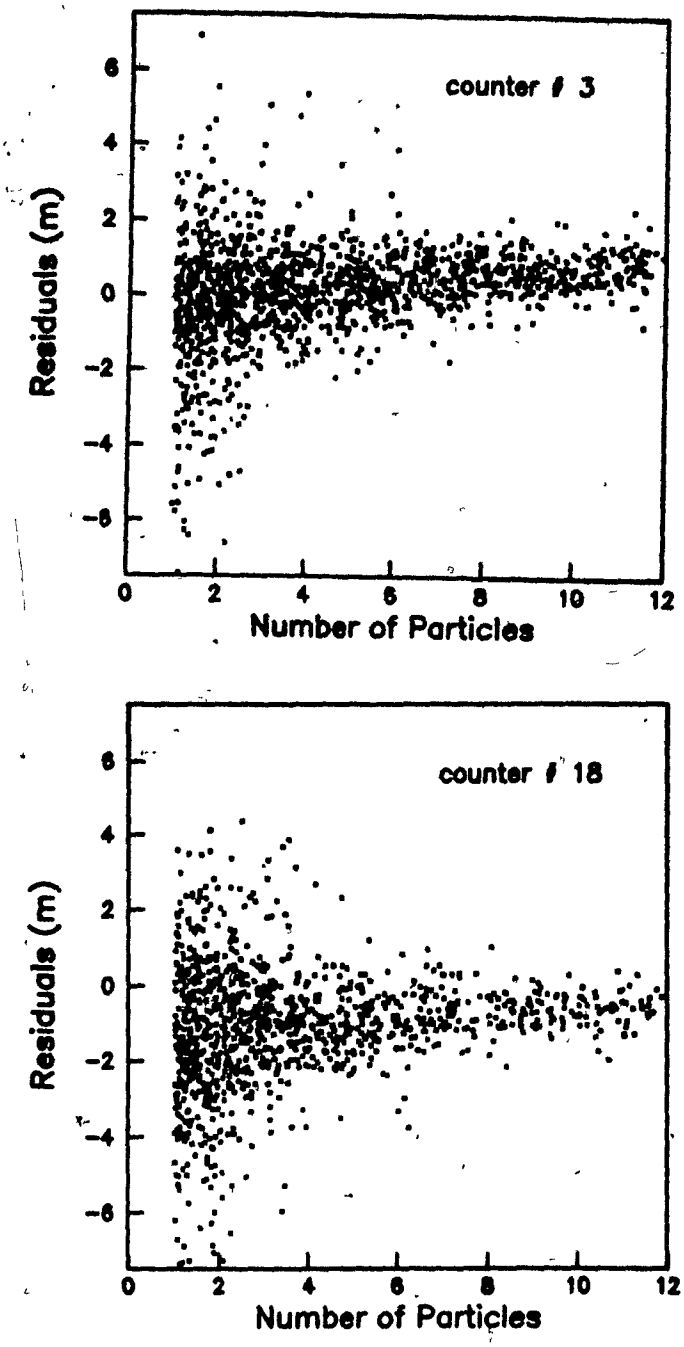

FIG 5.6: The residuals for detector (a) 3, and (b) 18 are shown as a function of the number of electrons in the detector at the time of the measurement.

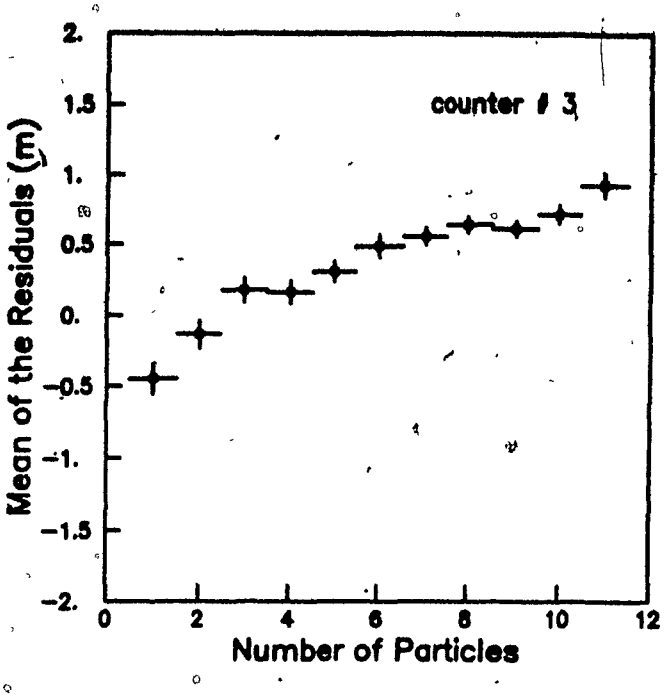

(a)

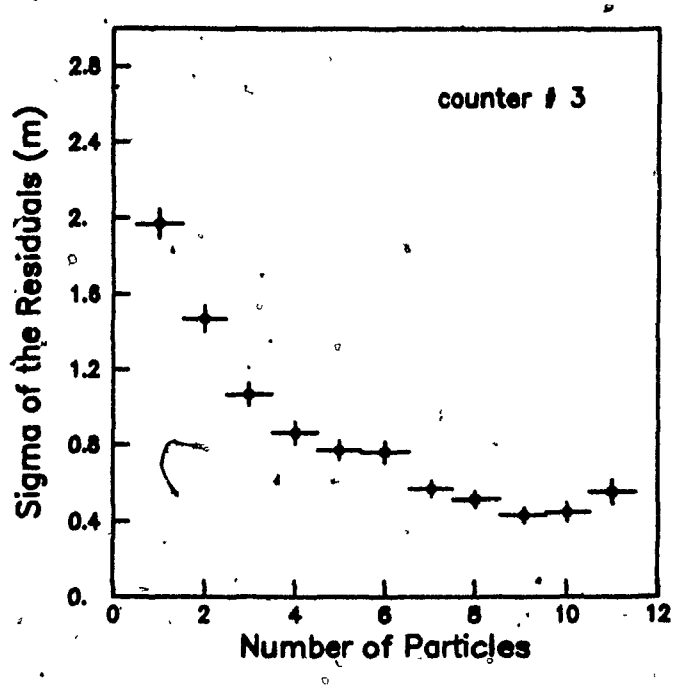

(b)

FIG 5.7: The mean and σ of the residuals for counter 3 is shown as a function of electrons

The residuals are again calculated, but this time they are plotted as a function of number of electrons detected. Figure 5.6 shows two examples of this. The more electrons there are detected in the counter, the higher the probability that one of the electrons was within the leading edge of the detector, which would explain why the residuals are larger when the number of particles is lower. Figure 5.7 shows a plot of the residual means and σ's as a function of the number of electrons for detector 3 and 19. These σ's are then tabulated and again the data is re-analyzed by weighting the data as a functions of the number of electrons (ie: $wt_i(N_e) = [1/\sigma_i(N_e)]^2$. Those detectors which measured the edge of the shower will not participate as strongly in the fit as the ones which detected the center of the shower.

If the residuals are calculated properly, the χ^2 per degree of freedom should peak at 1. The degree of freedom (dof) is the number of detectors participating in the event, minus the number of constraints (3). A histogram of the χ^2/dof is shown in figure 5.8. The peak centers around 1 so it can be assumed that the estimation of the timing uncertainties is correct.

Calculation of Angular Error

In the Monte Carlo program, the angular resolution was calculated by comparing the calculated normal vector with the original normal vector. However, for real data, the original vector is not known. One method of estimating the angular resolution is by using the covariant matrix, described in section 5.1 If all the estimated σ_α's are histogrammed, the total angular resolution is the limit within which 98% of the

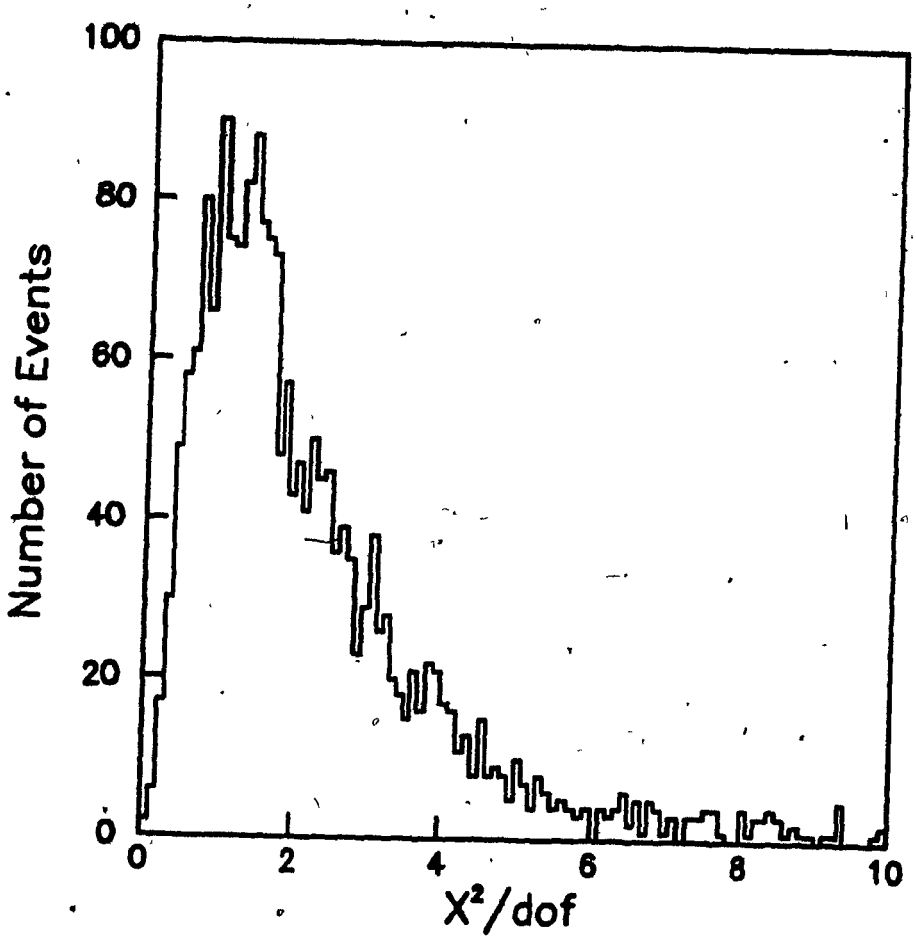

FIG 5.8: A histogram of the χ^2 per degree of freedom.

events occur.

Another method of estimating the angular resolution is done in the following manner. After the best fit for the shower is obtained, each detector time is modulated by a random amount, which is dependent upon the previously calculated residuals for that detector. The 'new' times are then re-fit and then the error in the angular measurement is found by taking the dot product between the old and the new normal vectors. This is repeated 5 times for each accepted shower. The angles are histogrammed, and the angular resolution is defined to be the limit within which 63% of the events occur.

When we impose an additional data cut that the χ^2/dof is less than 8, the angular resolution (illustrated in figure 5.9) was estimated to be 0.55° and 0.65° by the two methods described above.

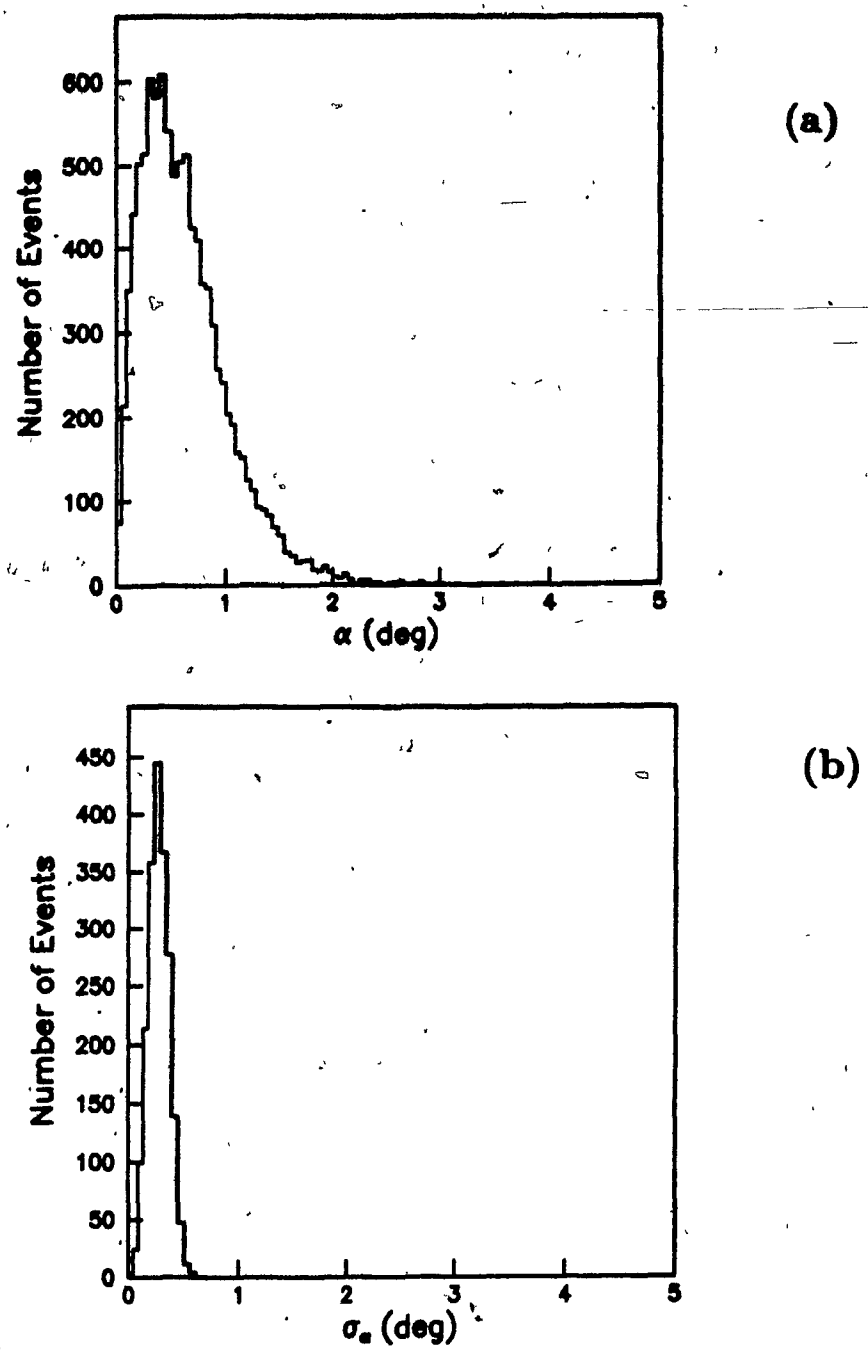

FIG 5.9: (a) The σ_α calculated from the covariant matrix, giving an angular resolution of 0.55°, and (b) the α calculated by varying the times of the real data and re-fitting the event (see text for more detailed description), giving an angular resolution of 0.65°.

5.4 Star Tracking

Coordinate Systems

Once the local coordinates θ and ϕ are calculated, we must then interpret them in terms of celestial objects. Before this can be done, we must first define what is commonly known as the celestial sphere. Imagine a sphere with earth at the center, rotating in the east to west direction about the earth. All celestial objects will then appear to be fixed points on this sphere. The following is a list of the important points or great circles on the celestial sphere, shown in figure 5.10 and figure 5.11.

local zenith point: A point defined by extending the line joining the center of the Earth and the observer's position on the Earth.

horizon: A great circle defined by the intersection of the celestial sphere with a plane which is perpendicular to the local zenith, and passes through the center of the Earth. Note that due to the finite size of the Earth, mountains etc., the visual horizon of the observer is not necessarily the 'horizon' defined here.

celestial poles: The intersection of the rotational axis of Earth with the celestial sphere defines the two points; the North and South celestial poles.

observer's meridian: A great circle perpendicular to the horizon and passing through the local zenith and the north celestial pole.

north point: A point defined by the intersection of the horizon and the great

circle passing through the North and South celestial poles.

celestial equator: A great circle defined by the intersection of the celestial sphere with a plane which also intersects with the Earth's geodetic equator.

ecliptic: A great circle defined by the apparent path of the sun during the course of one year.

equinox: Two points defined by the intersection of the ecliptic with the celestial equator. The vernal equinox occurs in spring and the autumnal equinox occurs in the autumn, the two days in the year when the day and night are both 12 hours long.

sidereal day: Equal to the time between crossing of the observer's meridian by a point fixed on the celestial sphere. This is not equal to one solar day.

$$1 \text{ sidereal day} = 1.002738 \text{ solar day}$$

In the Local Horizon Coordinates, a celestial object is defined by the altitude θ', and the azimuth ϕ' where

θ' is the angle between the horizon and the celestial object and

ϕ' is the angle *east* of the north point.

As the earth spins, the local zenith point moves along the celestial sphere, thereby making θ' and ϕ' function of the time of day and the time of the year. To account for

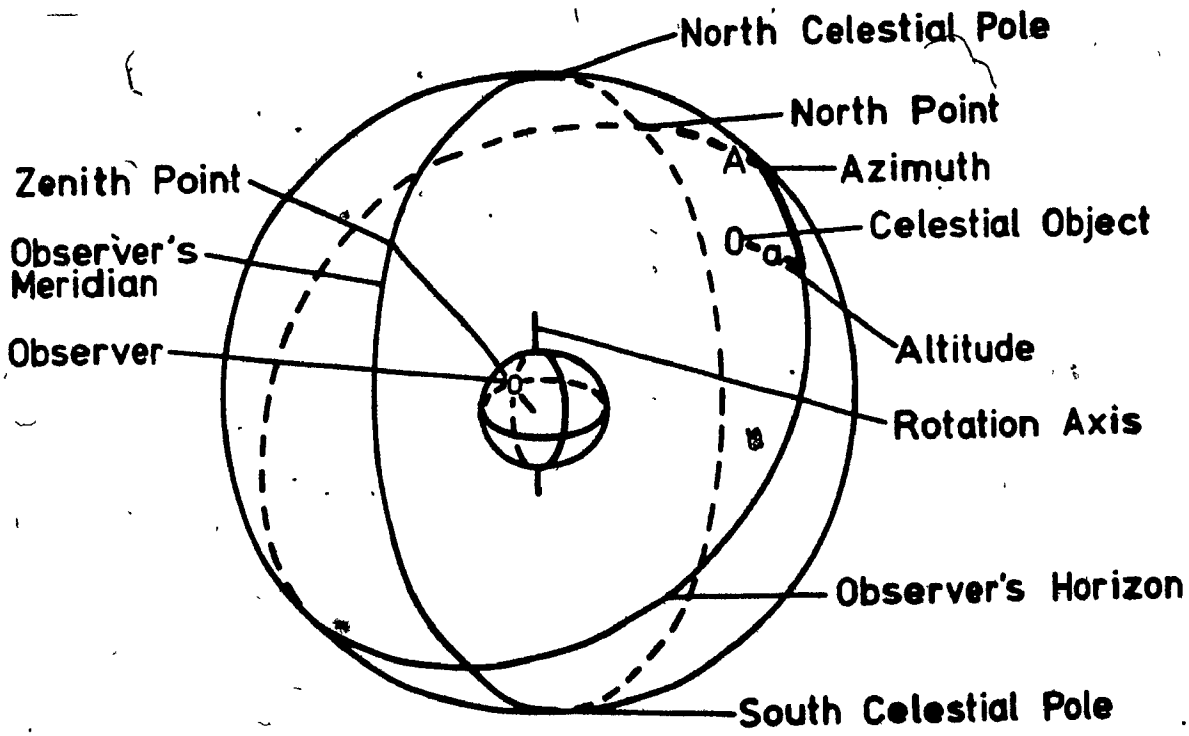

FIG 5.10: Local Horizon Coordinate system. The position of a stellar object is defined by the altitude θ' which is the angle ($\perp$ to the horizon) from the horizon to the object, and the azimuth ϕ' which is the angle east (along the horizon) from the north point.

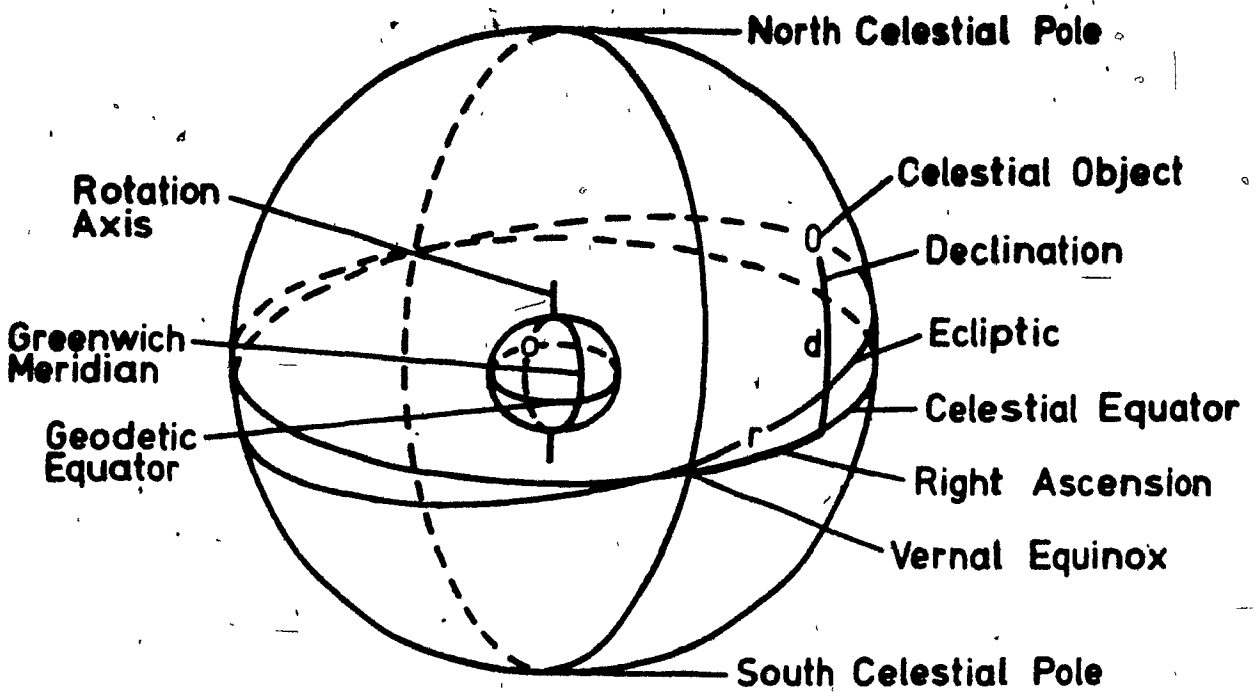

FIG 5.11: Equatorial Celestial Coordinate system of defining the position of a stellar object. The right ascension α is the angle east (along the celestial equator) from the vernal equinox. The declination δ is the angle ($\perp$ to the equator) from the equator to the object.

this difficulty, astronomers have developed coordinate systems which are independent of the motion of the Earth. One such system, called the Equatorial Celestial Coordinates, is shown in figure 5.11. In this coordinate system a celestial object is located by two coordinates, declination δ and the right ascension α where

δ is the angle between the celestial equator and the object and

α is the angle east of the vernal equinox.

It should be noted that α is often given in units of hour-angles (hr), where 1 hour-angle = 15 degrees/hour.

Transformation from Local to Celestial Coordinates

Before the transformation from local to celestial coordinated can be accomplished, the local mean sidereal time (LMST) must first be calculated, from the local (standard, not daylight savings!) time (LT) and the universal time (UT).[46]

$$\begin{aligned} \mathrm{UT} &= \mathrm{LT} + \lambda/15 \\ \mathrm{GMST} &= \mathrm{GMST}(0^h\mathrm{UT}) + 0^h.065710d + 1^h.002738t \\ \mathrm{LMST} &= \mathrm{GMST} - \lambda/15 \end{aligned} \qquad 5.10$$

where

λ = west longitude

GMST(0^hUT) = GMST on day 0 at 0^hUT of each month given in empheris tables. Table 5.1 lists the GMST(0^hUT) for 1986

GMST = greenwich mean sidereal time which is equal to the right ascension α (in hour-angles) of the celestial objects crossing the *Greenwich* meridian at this absolute time

LMST = local mean sidereal time which is equal to the right ascension α (in angle-hours) of celestial objects crossing the *observer's* meridian at this time.

d = day of the month

t = time in decimal hours UT

TABLE 5.1
Important Constants for Star Tracking

GMST on day 0 at 0^hUT of each month 1986			
Jan 06.6245^h	Apr 12.5384^h	Jul 18.5180^h	Oct 00.5633^h
Feb 08.6615^h	May 14.5097^h	Aug 20.5550^h	Nov 02.6003^h
Mar 10.5014^h	June 16.5467^h	Sep 22.5920^h	Dec 04.5716^h
Coordinates of the LEDA array			
$\beta = 45°25'26''$ N		$\lambda = 73°56'17''$ E	

From the local sidereal time and the right ascension of a celestial object, we can define the hour-angle h (angle west along the celestial equator from the observer's meridian to α);

$$h = (15 \times \text{LMST} - \alpha) \text{ deg.}$$

Given the latitude β and the LMST, spherical geometry relates the altitude θ' and

the azimuthal ϕ' to α and δ according to:[47]

$$
\begin{aligned}
a) \quad & \cos\theta' \sin\phi' = -\cos\delta \sin h \\
b) \quad & \cos\theta' \cos\phi' = \sin\delta \cos\beta - \cos\delta \cos h \sin\beta \\
c) \quad & \sin\theta' = \sin\delta \sin\beta + \cos\delta \cos h \cos\beta \\
d) \quad & \cos\delta \cos h = sin\theta' \cos\beta - \cos\theta' \cos\phi' \sin\beta \\
e) \quad & \sin\delta = \sin\theta' \sin\beta + \cos\theta' \cos\phi' \cos\beta
\end{aligned}
\qquad 5.11
$$

Since δ by definition is less than 90°, it is determined uniquely by equation 5.11e. However, h can vary over 360°, so $\sin h$ and $\cos h$ must be determined separately by equations 5.11a and 5.11d to give the correct quadrant.

The accuracy of the above equations are dependent on the accuracy of θ',ϕ' and the time measurement of the shower. As each shower is recorded on the LSI-11, the current time (in seconds past midnight) is also recorded. The time on the computer is set in conjunction with the time signal given by CBC at 1:00 Eastern Standard Time. The computer time is then checked daily against a quartz digital watch (accurate to within 6 seconds/month). In the worst case of an error in our time of six seconds, the corresponding error in the hour-angle will be 0°1′30″. This is negligible compared to the angular resolution given by the previous section.

The viewing area of the sky is illustrated in figure 5.12, where each dot is proportional to the number of showers recorded, which came from that location in the sky, during the month of January 1988. It can easily be seen that at our latitude, Cygnus X-3 ($\delta = 40.^{\circ}9 \quad \alpha = 307.^{\circ}8$) is well within our visible range of the sky.

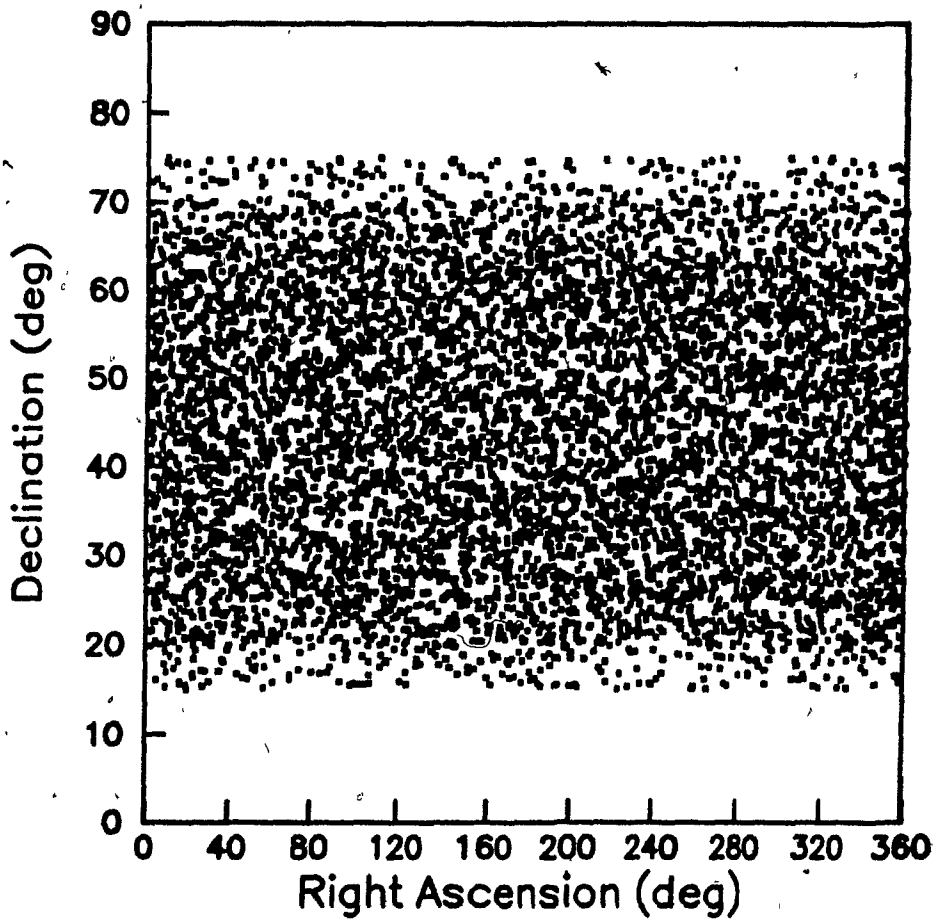

FIG 5.12: The map of the sky is shown where the number of recorded showers (during January 1988) is proportional to the number of dots. Cygnus X-3 has the coordinates $\delta = 40.^{\circ}9$ and $\alpha = 307.^{\circ}8$.

6.0 CONCLUSION

The angular resolution for our array, calculated by the Monte Carlo is 1.25°. However, since the model was a highly simplistic view of the real shower front (Gaussian distributions of curvature, etc.) this resolution is considered to be pessimistic. The angular resolution calculated from the data (0.65°) is much smaller than that predicted by the Monte Carlo. However, since the data analysis does not consider the effects of measuring only a portion of the shower front, the angular resolution is estimated to be between 0.65° and 1.25°. This resolution is of the same order as that of the Kiel group,[23] and so we conclude that we will be able to observe any strong γ-ray sources within our visible range ($20° < \delta < 70° N$ and $0° < \alpha < 360°$), given sufficient viewing time.

In the future, we hope to improve the timing resolution by adding a thin layer of lead. This will reduce the shower thickness and curvature problems because γ-rays will be converted into electrons, and this yields an additional signal which is earlier in time.[51] A more accurate estimation of the angular resolution can be found if the relation of shower curvature to shower size is understood, either by measuring the curvature directly, or by simulating the shower front by modelling the entire shower process starting from the original cosmic ray.

APPENDIX A

A.1 A Simulation of the Light Cone of the LEDA Detector

Assumptions and Restrictions

To simulate the timing resolution of the light cone in the LEDA detector, the following conditions were imposed upon the Monte Carlo program:

(1) Because we wished to model the light cone only, the quantum efficiency of the PMT was not included in the calculations. We assume that if the reduction of photons detected is constant over the entire gate width, the pulse shape (although not the pulse-height) will remain unchanged

(2) The rise-time of the PMT was given in the manual as $6.5\,ns$, so for simplicity sake we assumed that each photon generates a Gaussian pulse with a $6.5\,ns$ rise-time (defined as the time it takes to go from 10% to 90% of the maximum peak. This corresponds to a σ of $3.85\,ns$

(3) The PMT was considered to be a flat plane instead of hemispherical, and we assumed it has a uniform response across the photo-cathode.

(4) The pulse spectrum is integrated over $150\,ns$ since this is the gate width used in our experimental analysis.

(5) The mylar on the light cone was assumed to be 99% efficient, the reflectivity of the scintillator dish was given as 90%. The top of the scintillator dish was assumed to be 100% transparent.

(6) The index of refraction of the scintillator was approximated to be 1.5, and it was

also assumed to be independent of the wavelength of the photon.

(7) The light generated by the scintillator was assumed to be uniformly distributed over the path of the cosmic ray.

(8) Our detector was designed to give a uniform pulse-height with no radial dependence. Hence the pulse-height, defined as the number of photons hitting the PMT, was normalized and given no radial dependence.

(9) The shape of the scintillator dish was simplified by assuming a flat bottom.

(10) The number of photons generated by the scintillator was completely arbitrary, and was chosen to be sufficiently large so that statistical fluctuations would be minimized.

(11) We also ignored all photons that would be internally reflected in the scintillator since, by our simplified version, they would remain trapped until they are absorbed by the walls of the tray.

Modelling of the Detector

Our detector was modelled by using the intersection of 19 planes. Eight planes were used to describe the light cone, one plane for the PMT, one plane for the scintillator–air boundary, and another nine planes were defined for the scintillator tray.

To calculate the path of the photon in the light cone, we used the following vector analysis (see figure A.1).

Let

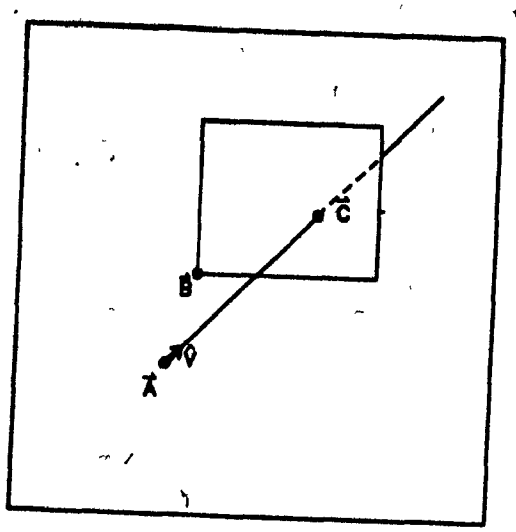

FIG A.1: A vector $\vec{A}$ with direction $\hat{V}$ intersects with a plane, defined by the vector $\vec{B}$ and the normal $\hat{n}$, intersects at a point defined by the vector $\vec{C}$.

$\vec{A}$ = the initial position of the photon

$\hat{V}$ = directional vector of the photon trajectory

$\hat{n}$ = outward unit normal of the detector plane

$\vec{B}$ = any point in the plane which, when combined with $\hat{n}$, uniquely defines it

$\vec{C}$ = the interception point of the photon with the plane

α = length of the path from $\vec{A}$ to $\vec{C}$

then

$$\vec{C} = \vec{A} + \alpha\hat{V} \qquad A.1$$

For two points on the same plane we know that

$$(\vec{C} - \vec{B}) \cdot \hat{n} = 0$$

$$\text{or } \vec{C}\cdot\hat{n} = \vec{B}\cdot\hat{n} \qquad A.2$$

Rewriting equation A.1 and then taking the projection onto $\hat{n}$ gives

$$\alpha\hat{V}\cdot\hat{n} = (\vec{C}-\vec{A})\cdot\hat{n}$$

$$\Rightarrow \alpha\hat{V}\cdot\hat{n} = (\vec{B}-\vec{A})\cdot\hat{n} \quad \text{from eq'n A.2}$$

$$\Longrightarrow \alpha = \frac{(\vec{B}-\vec{A})\cdot\hat{n}}{\hat{V}\cdot\hat{n}} \qquad A.3$$

and

$$\vec{C} = \vec{A} + \left(\frac{(\vec{B}-\vec{A})\cdot\hat{n}}{\hat{V}\cdot\hat{n}}\right)\hat{V} \qquad A.4$$

To determine which plane the photon struck, we calculated α for each plane using equation A.3 and then used the following argument; the plane which has the shortest positive distance between the origin of the photon and the intersection point must be the one which the photon hit. Once the intersection point was discovered, the position of the photon was then calculated using equation A.4. The travelling time of the photon is α/c (c = speed of light in air).

The new direction vector $\hat{V}$ of the photon had to be calculated differently for reflected and refracted photons (shown in figure A.2). The direction of a reflected photon obeys the law of reflection which states *the component parallel to $\hat{n}$ changes sign.* Therefore, if $\hat{V}_i$ is the incident direction, and $\hat{V}_r$ is the reflected direction,

$$\hat{V}_r = \hat{V}_i - 2(\hat{V}_i\cdot\hat{n})\hat{n}. \qquad A.5$$

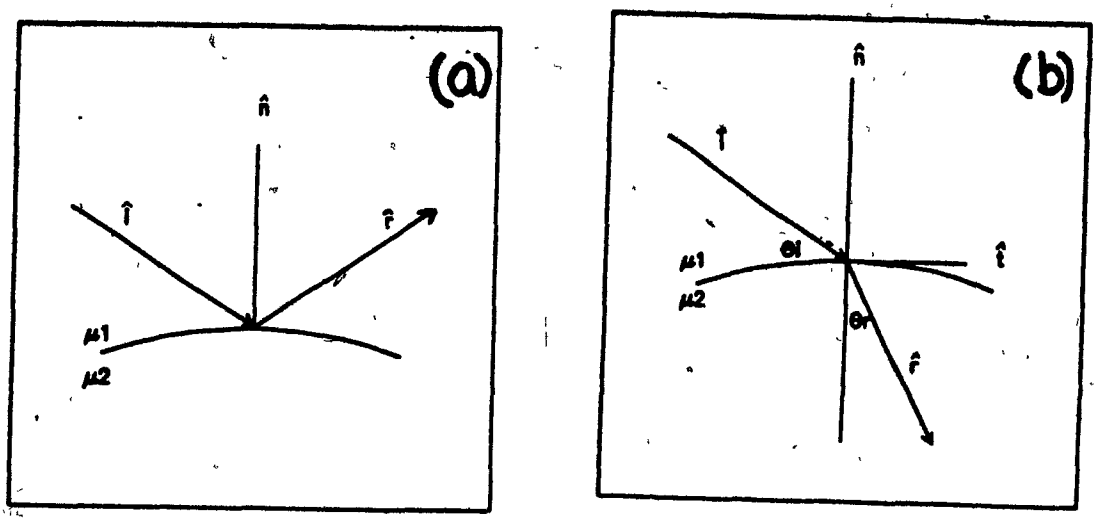

FIG A.2: (a) The reflection of light from a boundary between $\mu 1$ and $\mu 2$. (b) The refraction of light through a boundary between $\mu 1$ and $\mu 2$.

The direction of a refracted ray is is described by

$$\hat{V}_r = \hat{t}\sin\theta_r + \hat{u}\cos\theta_r \qquad A.6$$

$$\hat{u} = \hat{n}\,[\text{sign}(\hat{V}_i \cdot \hat{n})]$$

$$\sin\theta_r = n\,\sin\theta_i$$

where

$\hat{t}$ = unit tangent in the plane of incidence

$\hat{u}$ = unit normal with which $\hat{V}_r$ subtends an acute angle.

With the new position and directional vectors calculated for the photon, the process is repeated until the photon either is absorbed, or hits the PMT.

The program was used to simulate our experimental data. 10 cosmic ray events were generated at each fixed radial position, where the position is defined as the x-y coordinates of the cosmic ray as it crosses the bottom of the tray. Photons were continually generated until the total number striking the PMT in $150\,ns$ was 5000, which means that, the total number of photons generated varied with radial position to compensate for the collection efficiency. Thus, the pulse-height effects on timing resolution will not be modelled. As each photon strikes the PMT, it forms a Gaussian curve with a rise time of $6.5\,ns$, and a time offset corresponding to the travel time of the photon. The pulse shape is generated by adding each individual Gaussian curve. The measured time is then given as the point when the pulse shape passed a given trigger level.

REFERENCES

[1] Hayakawa, S., Cosmic Ray Physics John Wiley & Sons, N.Y., 1969 pg 9.

[2] Cocconi, G., *Hand-buch der Physik*, **XLVI,1**, 215 (1967)

[3] Greisen, K., *Ann. Rev. of Nuclear Science*, **10**, 63 (1960)

[4] Schein,M., Jeese,W.P., and Wollan,E.O., *Phys. Rev.*, **59**, 615 (1941)

[5] Greisen, K., *Progress in Cosmic Ray Physics*, **3**, 3 (1956)

[6] Rossi, B., and Williams, R.W., *Phys. Rev.*, **72**, 172 (1947)

[7] Bassi, P., Clark, G., and Rossi, B., *Phys. Rev.*, **92**, 441 (1953)

[8] Nikolsky, S.I., *Nucl. Inst. Meth.*, **A248**, 214 (1986)

[9] MacKeown P., and Weekes, T.C., *Scientific Amer.*, **253**, 60 (Nov 1985)

[10] Weekes, T.C., *Nucl. Inst. Meth.*, **A264**, 55 (1988)

[11] Neshpor, Yu.I., Stephanian, A.A., Fomin, V.P., Gerasimov, S.A., Vladimrsky, B.M., and Sixkin, Yu.L., *Astrophys. Space Sci.*, **61**, 349 (1979)

[12] Cassiday, G.L., Bergeson, H.E., Loh, E.C., Elbert, J.W., and Steck, D., *AIP conf. proc.*, **49**, 417 (1978)

[13] Murthy, K., *Energy Measurement Capabilities of the LEDA Array*, Master's Thesis, McGill University, Montreal, (1987)

[14] Smith, A.C., and Thompson, M.G., *Nucl. Inst. Meth.*, **145**, 289 (1977)

[15] *Nature phys. Sci*, **239**, 113 (1972)

[16] Galper, A.M., Kirillov-Ugrimov, V.G., Kurochkin, A.F., Leikov, P.G., Luchkov, B.I., and Yourkin, Y.T., *Soviet Astr. AJ Letters*, **2**, 206 (1976)

[17] Lamb, R.C., Fichtel, C.E., Hartman, R.C., Kniffen, D.A., and Thompson D.J., *Astrophys. J.*, **212**, L63 (1977)

[18] Parsignault, D.R., Schreierr, E., Grindlay, J., and Gursky, H., *Astrophys. J.*, **L73**, 209 (1976)

[19] Bennett, K.M.V., Maraschi, L., Bignami, G., Helmklen, H., Margon, B., Hjellming, R., Bradt, H.V., and Dower, R.G., *Nature*, **273**, 450 (1978)

[20] Helmken, H.F., and Weekes, T.C., *Astrophys. J.*, **228**, 531 (1979)

[21] Danaher, S., Fegan, D.J., and Porter, N.A., *Nature*, **289**, 568 (1981)

[22] Lamb, R.C., Godfrey, C.P., Wheaton, W.A., and Tümer, T., *Nature*, **296**, 543 (1982)

[23] Samorski, M., and Stamm, W., *Astrophys. J.*, **268**, L17 (1983)

[24] Lloyd-Evans, J., Coy, R.N., Lambert A., Lapikens, J., Patel, M., Reid, R.J.O., and Watson, A.A., *Nature*, **305**, 784 (1983)

[25] Kifune, T., Nishijima, H., Hara, T., Hatano, Y., Hayashida, N., Honda, M., Kamata, K., Matsubara, Y., Mori, M., Nagano, N., Tanahaski, G., and Teshima, M., *Astrophys. J.*, **301**, 230 (1986)

[26] R.M. Baltrusaitis et al., *Sporadic and Periodic* $10 - 1000 TeV$ *γ-rays from Cygnus X-3* preprint

[27] Alexeenko et al., *Cygnus X-3 Observation in Gamma Ray energy Range* $> 10^{14} eV$ preprint

[28] Crouch, P.C., Gerhardy, P.R., Patterson, J.R., Clay, R.W., and Gregory, A.G., *Nucl. Inst. Meth.*, **179**, 467 (1981)

[29] Protheroe, R.J., Clay, R.W., and Gerhardy, P.R., *Astrophys. J.*, **280**, L47 (1984)

[30] Baltrusaitus, R.M., Cassiday, G.L., Cooper, R., Elbert, J.W., Gerhardy, P.R., Loh, E.C., Mizumoto, Y., Sokolsky, P., Sommers, P., and Steck, D., *Astrophys. J.*, **293**, L69 (1985)

[31] Poirier,J.,Canough,G.,Funk,E.,Kinney,P.,LoSecco,J.,Mikocki,S.,&Rettig,T., *Nucl. Instr. Meth.*, **A264**, 81 (1988)

[32] Gibbs,K.G. et al, *Nucl. Instr. Meth.*, **A264**, 67 (1988)

[33] Eichler, D., Vestrand, W.T., *Nature*, **307**, 613 (1984)

[34] Vestrand, W., Eichler, D., *Astrophys. J.*, **261**, 251 (1982)

[35] Chanmugan, G., Brecher, K., *Nature*, **313**, 767 (1985)

[36] Kazanas, D., and Ellison, D.D., *Nature*, **319**, 380 (1986)

[37] Milgom, M., and Pines, D., *Astrophys. J.*, **220**, 272 (1978)

[38] Bultena, S., Hanna, D.S., Murthy, K., *Nuclear Instr. Meth.*, **A260**, 247 (1987)

[39] Clay, R.W., and Gregory, A.G., *Nucl. Inst. Meth.*, **153**, 467 (1978)

[40] **Hamamatsu**, Technical Data Sheet, *5 inch hemispherical photomultiplier tube R2218*

[41] THORN EMI Gencom Inc., *Photomultipliers* THORN EMI Electron Tubes Ltd.New Jersey1986

[42] Hearing, H., and Wright, A.G., *IEEE Trans. Nucl. Sci.*, **RS-26 no 1**, 368 (1979)

[43] Clark, W., Earl, J., Kraushaar, W.L., Linsley, J., Rossi, B.B., Scherb, F., and Scott., D.W., *Phys. Rev.*, **122**, 637 (1961)

[44] European Physical Society, **FORMULAE AND METHODS IN EXPERIMENTAL DATA EVALUATION with emphasis on High Energy Physics**, Jan 1984

[45] Smith, A.C., Thompson, M.G., *Nucl. Instr. Meth.*, **145**, 289 (1977)

[46] Bishop, R.L., The Royal Astronomy Society of Canada, Observer's Handbook 1986, Toronto, 1986

[47] Worstel, A.W., *An Experimental Search for a Time-Modulated Muon Flux from the Direction of Cygnus X-3*, PhD. Thesis, Harvard University, Cambridge,

[48] Morello, C., Navarra, G. & Vernetto, S., *Conference papers of 18th international Cosmic Ray Conference, Bangalore*, **1**, 127 (1983)

[49] Stepanian, A.A., Fomin, V.P., Neshpor, Yu.I., Vladimirsky, B.M. & Zyskin, YU.L., *Proceedings of the International Workshop on Very High Energy Gamma Ray Astronomy*, **Ootacamund, India**, 43 (1982)

[50] Mukanov, D.B., Nesterova, N.M., Stepanian, A.A. & Fomin, V.P., *Isv. Krymskoi. Astrofiz. Obs.*, **62**, 98 (1980)

[51] Pojrier, J. and Mikocki, S., *Nuclear Instr. Meth.*, **A257**, 473 (1987)